

SCUOLA DI SCIENZE

Dipartimento di Chimica Industriale "Toso Montanari"

Corso di Laurea Magistrale in

Chimica Industriale

Classe LM-71- Scienze e Tecnologie della Chimica Industriale

**Synergistic Catalysis: Michael
addition of acyl-pyridines**

Tesi di laurea sperimentale

CANDIDATO

Cecilia Poderi

RELATORE

Prof. Andrea Mazzanti

CORRELATORE

Dr. Ramon Rios Torres

Anno Accademico 2016-2017

Abstract

A new diastereo- and enantioselective strategy for the functionalization of 2-acetylpyridine with α,β -unsaturated aldehydes has been investigated through synergistic catalysis. In particular, the aim of the work was to use cinnamaldehydes bearing different substituents on the phenyl group and to study its effect on the yield, conversion and stereoselectivity of the reaction. The reaction mechanism involves combined iminium ion and transition metal catalysis in a synergistic fashion and proceeds with two consecutive Michael additions, followed by final intramolecular aldol condensation to yield the formation of three new stereogenic carbons, with high to excellent stereoselectivities. The structures of the molecules obtained were fully characterized by NMR spectroscopy. After having assigned the relative configuration by NOE-NMR and 2D-COSY experiments, conformational analysis was performed by DFT calculations to find the most stable molecular conformations. The absolute configuration of each diastereoisomer was then eventually assigned by quantum mechanical simulations of the Electronic and Vibrational Circular Dichroism spectra.

Abstract

In questo progetto è stata sviluppata una strategia di funzionalizzazione diastereo- ed enantioselettiva di 2-acetil-piridina con aldeidi cinnamiche α,β -insature attraverso catalisi sinergica. In particolare, lo scopo del lavoro è stato quello di utilizzare aldeidi cinnamiche con diversi gruppi sostituenti sul fenile e studiarne l'effetto sulla resa, sulla conversione e sulla stereoselettività della reazione. Il meccanismo di reazione prevede due cicli catalitici separati che combinano immينو-catalisi e organometallo-catalisi, e la reazione procede tramite due addizioni di Michael consecutive seguite da una condensazione aldolica intramolecolare, portando alla formazione di tre centri stereogenici con elevati eccessi enantiomerici. La struttura delle molecole ottenute è stata determinata tramite spettroscopia NMR assegnando la configurazione relativa attraverso esperimenti NOE-NMR e 2D-COSY; in seguito è stata svolta l'analisi conformazionale tramite calcoli DFT, ottenendo la conformazione molecolare più stabile. La configurazione assoluta di ogni diastereoisomero è stata successivamente attribuita tramite simulazioni quanto meccaniche degli spettri di Dicroismo Circolare Elettronico e Vibrazionale.

Index

1	Introduction.....	1
1.1	Asymmetric organic synthesis	2
1.2	Enantioselective organocatalysis	3
1.3	Multicatalysis	6
1.3.1	Synergistic catalysis.....	7
1.3.2	Transition-metal and iminium catalysis.....	8
1.4	Domino reactions	12
2	Aim of the thesis	14
3	Results and Discussion	16
3.1	Scope of reaction with enals	16
3.2	Reaction with 2-propionyl-pyridine.....	20
3.3	Identification and characterization.....	22
3.3.1	HPLC purification	22
3.3.2	Characterization of compound 3i-major	23
3.3.3	Characterization of compound 3i-minor	34
3.3.4	Characterization of compound 3f-major	45
3.3.5	Characterization of compound 3f-minor	49
4	Conclusions.....	52
5	Experimental Part	53
5.1	General	53
5.2	Procedures and spectroscopic data of synthesized compounds.	54
6	Appendix.....	70
6.1	Density Functional Theory (DFT)	70
6.2	Electronic Circular Dichroism (ECD).....	72
6.3	Vibrational Circular Dichroism (VCD)	75
7	Bibliography	77

1 Introduction

This thesis is focused on the development of a new enantioselective synthetic strategy for the synthesis of pyridine derivatives, containing three stereogenic centres.

The first part of this project has been carried out at the University of Southampton under the supervision of Dr. Ramon Rios Torres. During this period, we performed the synthesis of the desired products and the characterizations by means of $^1\text{H-NMR}$, $^{13}\text{C-NMR}$, HRMS, OR, HPLC and IR, with the support of Gabriela Sitinova. Afterwards, we investigated relative and absolute configurations of the products at the University of Bologna by means of 2D-COSY and NOE-NMR experiments, ECD and VCD spectroscopies supported by quantum mechanical calculations.

1.1 Asymmetric organic synthesis

Natural compounds often present very complex scaffolds with a well-defined three-dimensional structure. This complexity is generally correlated with a defined stereochemistry of the products. Thus, the synthesis of chiral compounds has become an important issue in organic chemistry. Furthermore, chirality plays an important role in determining the characteristics of a substance. In fact, although the structures of two enantiomers are similar, each one individually could show different biological activity and different properties, such as pharmacokinetics, toxicology etc.⁽¹⁾ An evident example is drug Thalidomide (**Figure 1**), prescribed in the 1950's as sleeping drug and sedative for pregnant women. Unfortunately, it was not known that, while the (*R*)-thalidomide presents sedative properties, the (*S*)-thalidomide shows teratogen effects, involving the initiation of functional and structural disabilities.⁽²⁾

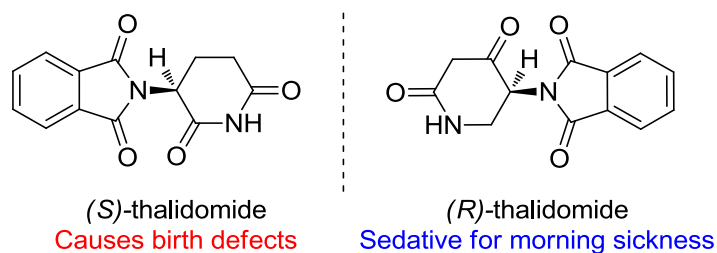


Figure 1. Thalidomide enantiomers structures.

For this reason, the opportunity to achieve enantiopure products through asymmetric synthesis has become a mandatory target in organic chemistry. Asymmetric synthesis is defined as a method for the preparation of chemical compounds, which aims to bias the synthesis in favor of producing one enantiomer over another one.

In order to improve asymmetric synthesis a catalytic strategy has to be used in many cases. Catalysis consists in a powerful method that improve the efficiency, sustainability and economicity of a chemical process and could be also used to discover new chemical reactions.

In particular, this thesis was focused on enantioselective catalysis, consisting in a kind of catalysis that allows the obtainment enantiopure products using a substoichiometric amount of catalyst.

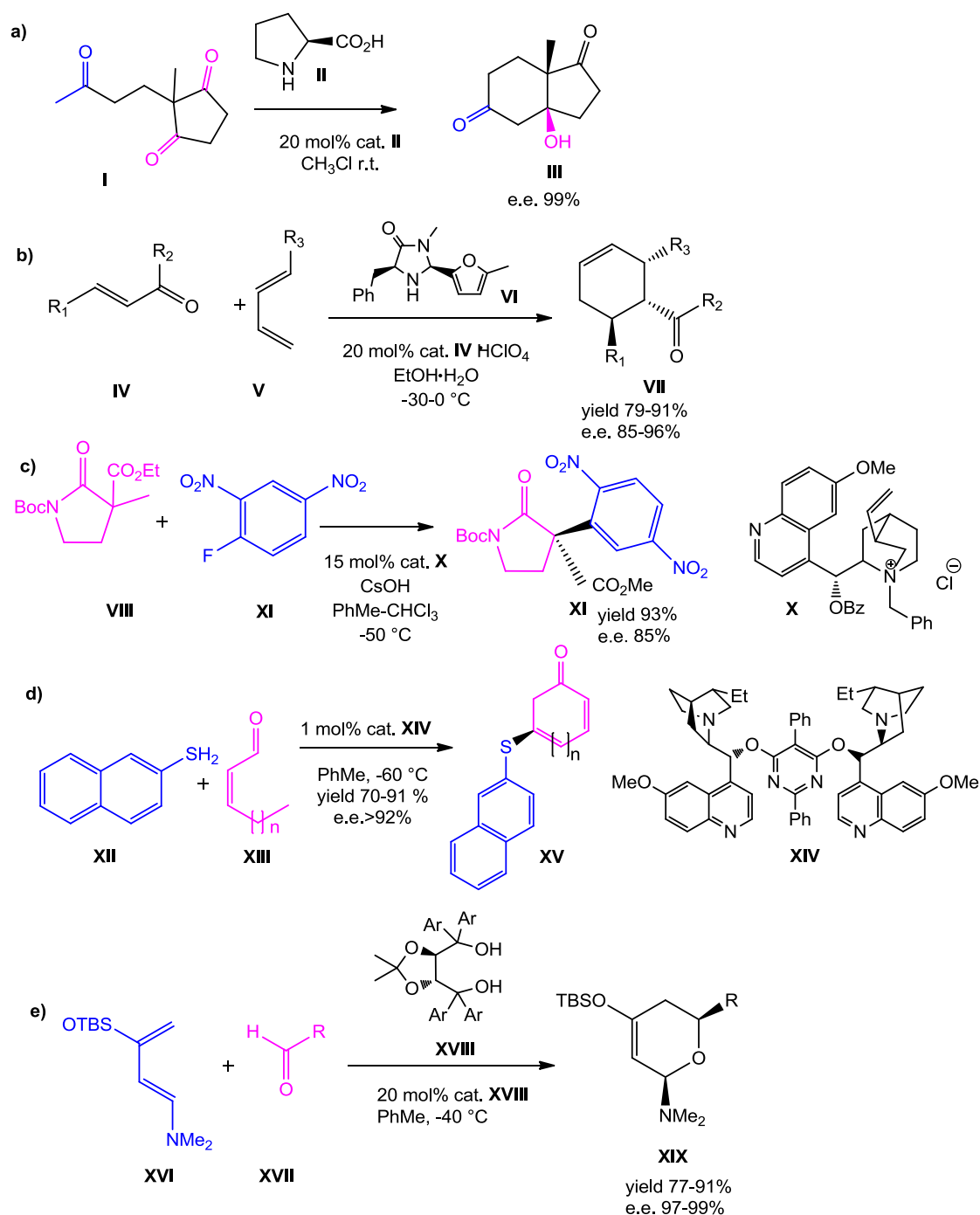
1.2 Enantioselective organocatalysis

The purpose of enantioselective catalysis is to control the stereochemistry of a reaction and obtain enantiopure products by means of an organic catalyst, instead of obtaining a racemic mixture.

The increasing number of diseases leads to the necessity of synthesizing new chiral and non-racemic compounds as pharmaceuticals. However, synthesis of drug candidates with one or more non-racemic asymmetric centres is difficult to achieve with classical asymmetric methods. Thus, new enantioselective strategies are required to achieve this target.⁽³⁾ The conventional synthetic methodologies employed to obtain chiral molecules involve the use of asymmetric metal complexes as catalysts.⁽⁴⁾ However, such transformations are not applicable on the industrial scale. In fact, the efficiency, simplicity and economicity of these methods have to be improved when it needs to be used in pharmaceutical synthesis. For this reason, over the past ten years, the field of enantioselective organocatalysis has gained a significant impact in chemical synthesis.⁽⁵⁾ Even if these strategies are still in progress, their reproducibility to a large amount of reactions makes it complementary to the conventional ones.

Organocatalysis has several advantages comparing with metal catalysis, such as a fewer toxicity, economicity and sustainability. In addition, most of the organocatalytic reactions are often easier to perform.⁽⁵⁾

Five different types of organocatalysis can be distinguished: a) secondary amine catalysis via enamines; b) secondary amine catalysis via iminium ions; c) phase transfer catalysis; d) nucleophilic catalysis and Brønsted base catalysis; and e) H-bonding catalysis (**Scheme 1**).



Scheme 1. Examples of: a) secondary amine catalysis via enamines;⁽⁶⁾ b) secondary amine catalysis via iminium ions;⁽⁷⁾ c) phase transfer catalysis;⁽⁸⁾ d) nucleophilic catalysis and Brønsted base catalysis⁽⁹⁾ and e) H-bonding catalysis.⁽¹⁰⁾

Aminocatalysis consists in a type of organo-catalyzed synthesis that employs primary or secondary amines, involving the formation of an iminium ion or an enamine intermediates. While the enamine intermediate increase the electron density on the α -carbon encouraging the electrophile attack (**Figure 2b**), the iminium ion decrease the electron density at the carbonyl atom activating the β -carbon at the nucleophile attack

(Figure 2a).⁽¹¹⁾ The formation of the enamine intermediate occurs when a secondary amine reacts with a carbonyl compound through dehydration, while iminium catalysis occurs when a secondary amine reacts in presence of an α,β -unsaturated compound.

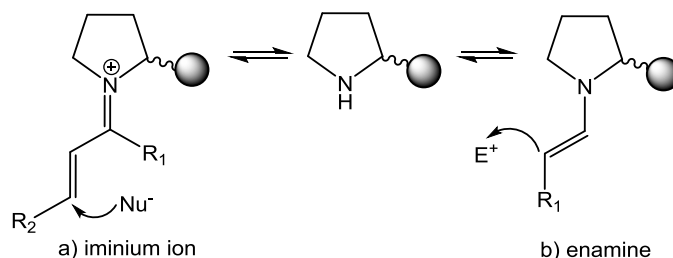


Figure 2. a) Iminium ion and b) enamine intermediates.

If a stereogenic centre is introduced on the secondary amine, this can induce an enantioselective iminium-catalysed addition. There are different kinds of chiral catalysts used for aminocatalysis, such as Jørgensen-Hayashi catalyst,⁽¹²⁾ MacMillan catalysts⁽¹³⁾ and proline.⁽¹⁴⁾

Enantioselective aminocatalysis combined with transition-metal catalysis in a synergistic fashion is known as a powerful strategy for the synthesis of potential targets, improving the efficiency of the synthesis.⁽¹⁵⁾ For this reason, a new multicyclic methodology combining aminocatalysis and metal Lewis catalysis has been explored in this project. In the next section the principal types of multicyclic catalysis will be discussed, with a particular focus on transition metal and iminium catalysis methodologies, which were employed in this work.

1.3 Multicatalysis

Enantioselective multicatalysis is a key towards sustainable synthetic strategies, which are becoming more and more used in organic chemistry. It consists in the combination of two catalytic cycles that conclude into one final product. Multicatalysis can be classified into four types, as shown in **Figure 3**.⁽⁹⁾ Bifunctional catalysis **a)** consists in both electrophile and nucleophile that are activated by the same catalyst but from two different sites. Cascade catalysis **b)** occurs when the starting reagent is activated sequentially from two different catalysts and then attached by a nucleophile. Double activation catalysis **c)** involves the activation of a single starting material by two different catalysts and successively attached by a nucleophile and for this reason is very similar to the previous one. Finally, synergistic catalysis **d)** consists in two different catalysts that activate two different starting materials by two catalytic cycles, concluding into one product.⁽¹⁶⁾

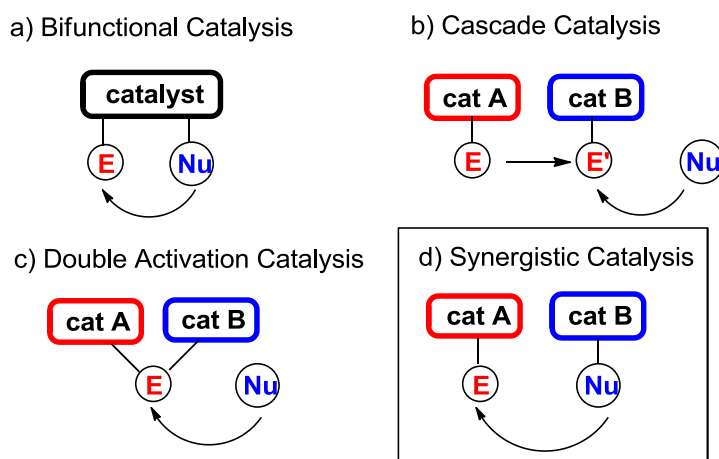


Figure 3. Types of multicatalysis discovered.

1.3.1 Synergistic catalysis

This project was based on synergistic catalysis as methodology for the synthesis of enantioselective compounds. This synthetic strategy presents many benefits, such as the opportunity to perform previously unachievable chemical transformations, the improvement of the efficiency of existing reactions and an higher enantioselectivity. Thus, synergistic catalysis became rapidly a powerful method used by different research groups.^(16a) The aim of this kind of catalysis is to create two reactive species, one with higher HOMO (nucleophile) and the other one with lower LUMO (electrophile) comparing with the starting reagents (**Figure 4**).⁽¹⁵⁾

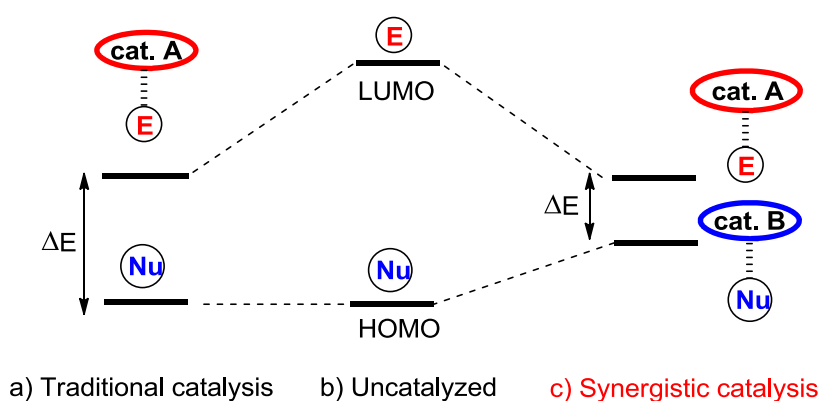


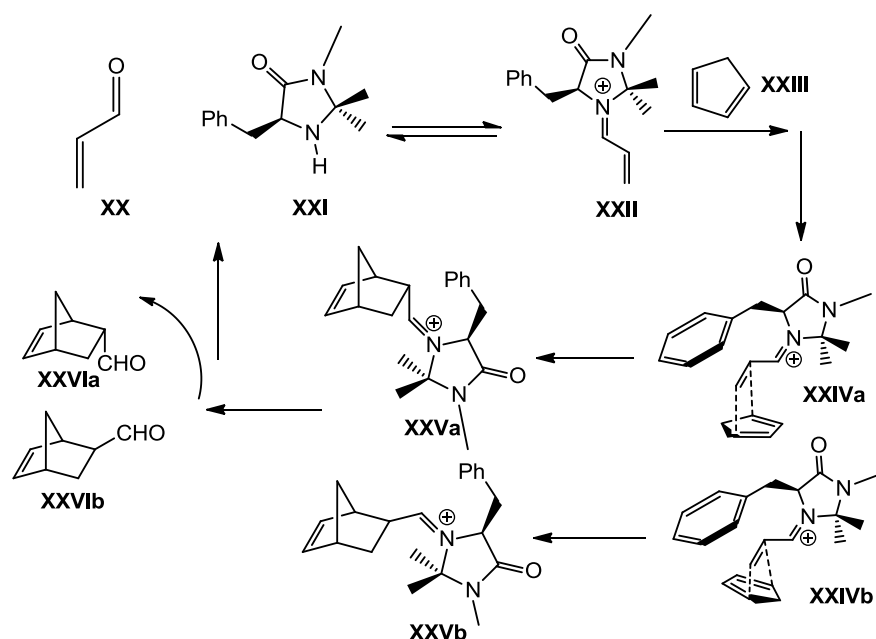
Figure 4. HOMO-LUMO energy levels in synergistic catalysis.

Another advantage is that the catalytic cycles can be optimized separately, since the modification of one catalyst does not affect the other. Despite the many benefits of synergistic catalysis, it has some disadvantages as well, such as auto-quenching, concentrations of the catalytic species and mostly in terms of economy, when using two catalysts to create one single bond is less efficient than mono-catalytic reactions. Usually in nature, the large structure of the proteins allows separating the catalytic sites and overcoming the problem, but this does not happen in laboratory experiments. Organic chemistry overcame this problem by a careful selection of the catalysis; as example, in recent years a new method using transition metal catalyst and organic catalysis has been studied, showing a high compatibility.^(15b) In the next paragraphs the mechanisms and the most important synergistic catalysis studies using the combination of transition metal and iminium catalysis is reported.

1.3.2 Transition-metal and iminium catalysis

MacMillan and co-workers in 2000 reported the first example of enantioselective iminium catalysis, performing a Diels Alder cycloaddition via enal activation, using a secondary amine as catalyst.⁽¹³⁾

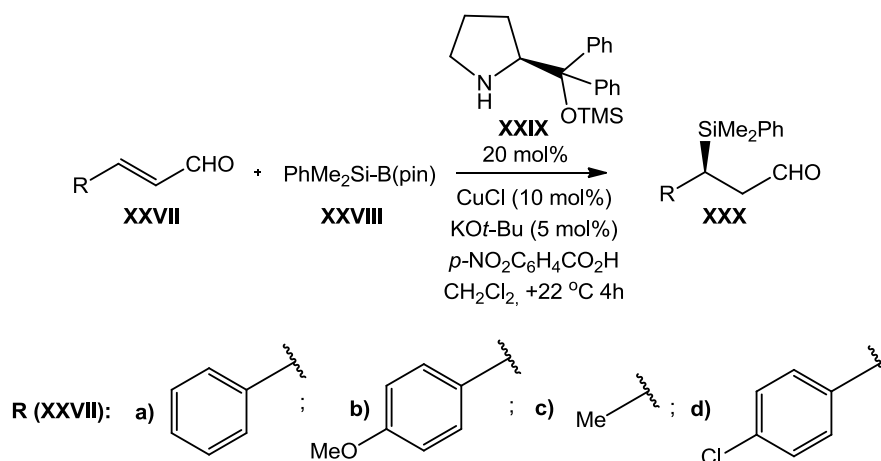
The mechanism involved the formation of the E-iminium ion (**XXII**) to avoid interactions between the double bond of the carbonyl-compound and the methyl substituents of the catalyst. Furthermore, the benzyl group blocks the Re-face forcing the Si-face attack (**Scheme 2**).



Scheme 2. Mechanism of Diels Alder cycloaddition via enal activation by MacMillan.

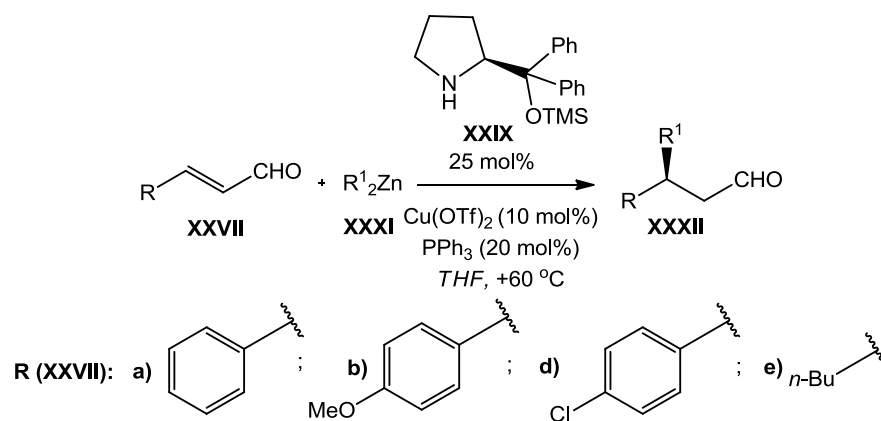
Synergistic catalysis combining amino-catalysis and transition metal catalysis has been known only using enamine and transition metal catalysis since Cordova's report from 2006.^(15b) However, while enamine catalysis only allows electrophilic reactions, iminium catalysis expands amino-catalytic reactions, introducing nucleophilic additions.

Cordova in 2011 reported the first example of combined iminium catalysis and transition-metal catalysis for an enantioselective silyl addition to enals, based on MacMillan's work (described above). The reaction was afforded with high yield and good enantioselectivity (**Scheme 3**).⁽¹⁷⁾



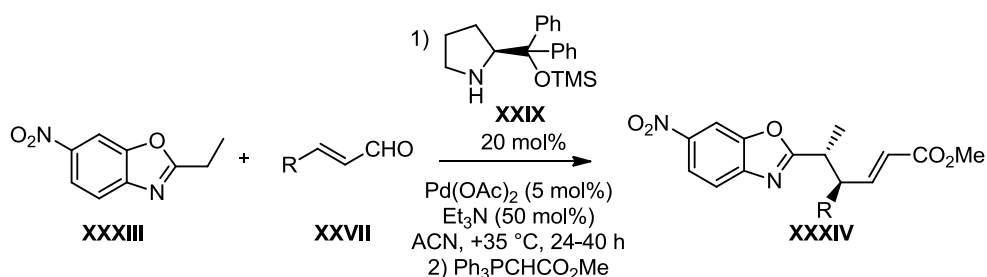
Scheme 3. Enantioselective silyl addition to enals by Cordova et al.

Later, Cordova and co-workers used the same method to perform a β -alkylation of enals using dialkyl-zinc reagent and Jørgensen catalyst (**XXIX**) as shown in **Scheme 4**.⁽¹⁸⁾ The mechanism involved a transmetalation between the dialkyl-zinc reagent and the copper (I) salt, which generated an organocuprate compound. The organocuprate compound reacted with the activated iminium form of the enal. In order to improve the enantio- and regioselectivity Cordova and team used different copper ligands, finding out that triphenylphosphine led to the best results.



Scheme 4. β -alkylation of enals by Cordova.

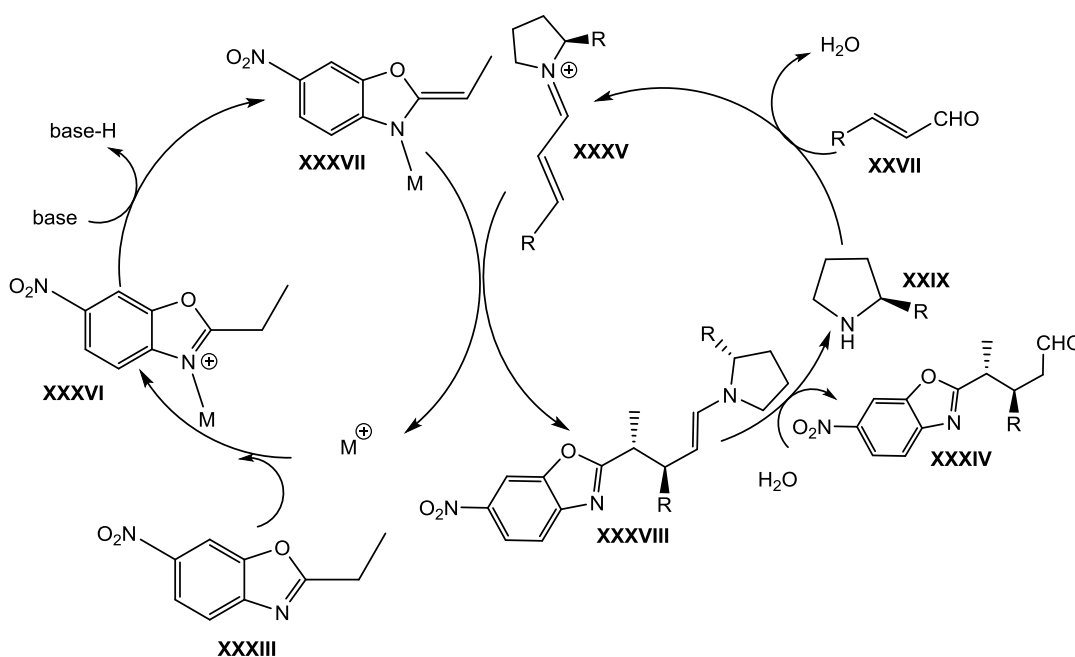
One of the most important examples reported in the literature was developed by Rios group, involving the activation of azaarenes by combined metal Lewis acid and iminium catalysis (**Scheme 5**).^(15c)



Scheme 5. Benzoxazole β -addition to enals by Rios.

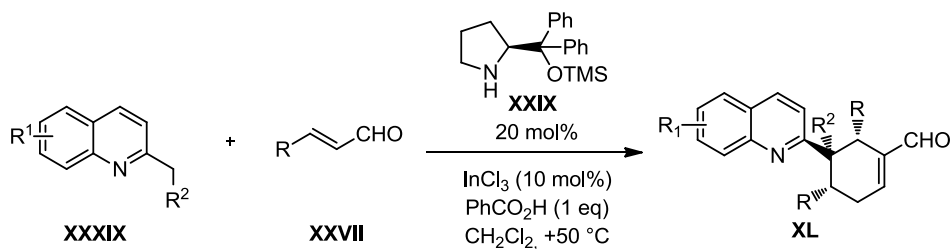
This method relied on the alkylazaarene activation through coordination of metal to the aromatic nitrogen. Then, activated azaarene (**XXXVII**) would attack the enal (**XXVII**), which was previously activated via iminium catalysis. An accurate screening of metal Lewis acid was made in order to select the metal with higher efficiency. palladium(II)acetate showed good results, achieving low diastereoselectivity, good enantioselectivity and satisfying yields, when an electron-withdrawing group is installed on the benzoxazole ring.

The proposed mechanism of this reaction is reported in **Scheme 6**.



Scheme 6. Mechanism of Benzoxazole β -addition to enals by Rios: catalytic cycle.

Recently, a cascade synergistic diastereo- and enantioselective functionalization of alkyl quinolines using α,β -unsaturated aldehydes has been explored by Jørgensen and co-workers (**Scheme 7**).⁽¹⁹⁾ This new activation method allowed obtaining products with good yields and good enantioselectivity (**XL**).



Scheme 7. Synergistic diastereo- and enantioselective functionalization of unactivated alkyl-quinolines with α,β -unsaturated aldehydes by Jørgensen group.

1.4 Domino reactions

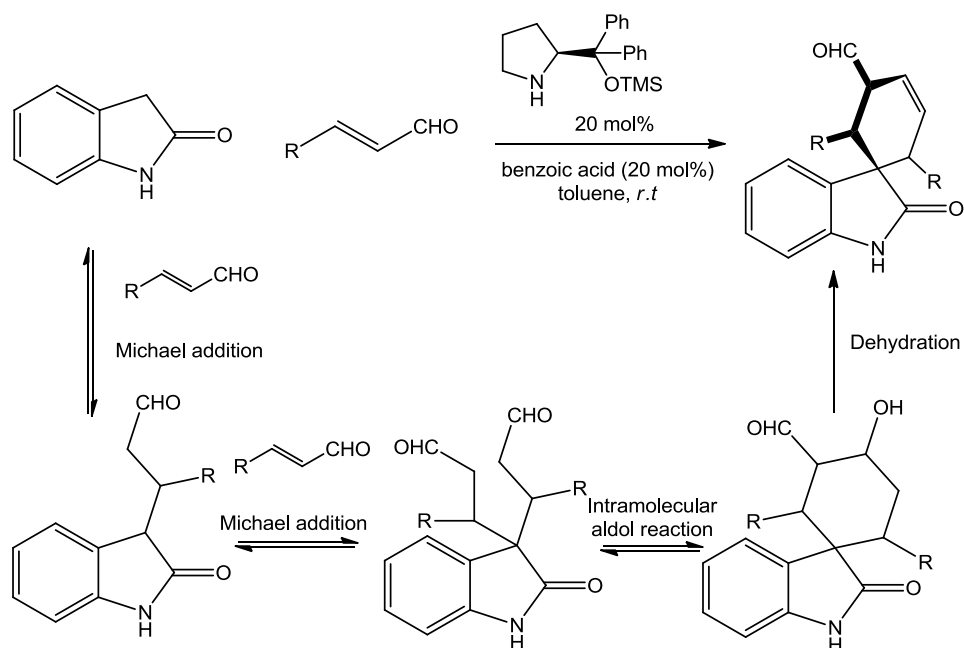
Enantioselective construction and preparation of natural compounds could result a big challenge for organic chemistry. In fact, building a very complex three-dimensional structure requires the development of new powerful synthetic strategies, involving catalytic cycles. Organocatalytic domino reactions⁽²⁰⁾ are one of the common economic and effective approaches that follow the rules of green and sustainable chemistry.⁽²¹⁾

According to Tietze, a domino reaction is defined as a reaction in which two or more bond-forming transformations occur on the base of the functionalities formed in the previous steps. It is not allowed to make any change in the reaction, such as an addition of reagents or other additives or conditions modification.⁽²²⁾

The efficiency of such reaction can be determined by the number of bonds generated, which leads to a complexity increase. The reactions can be performed as single, two, or multicomponent transformations, depending on how many reagents are used in the process.⁽²³⁾ The use of two-component and multicomponent domino reactions in organic synthesis is increasing constantly. Most of the examples of known domino reactions involve the use of chiral amines as catalyst,⁽²⁴⁾ which are ideal for the design of new asymmetric organocatalytic reactions and for the development of new catalytic cascade processes. Usually, domino reactions are distinguished by the type of reaction step and also by the type of activation mode.

In particular, Michael-Aldol domino reactions found a great amount of applications in organic synthesis. The first report of domino asymmetric process appeared in early 2000s from Barbas research group and involved combining iminium ion and enamine activation.⁽²⁵⁾ In 2007, Jørgensen and co-workers reported a powerful domino reaction between malononitrile and unsaturated aldehydes, consisting in an enantioselective Michael–Michael-Aldol reaction that built cyclohexenes in excellent yields and enantioselectivities, but in moderate to good diastereoselectivities.⁽²⁶⁾

Considered the state of art, in 2010, Rios et al. developed a Michael-Michael-Aldol domino enantioselective synthesis of spiro-compounds. High diastereo- and enantioselectivity were obtained, using Jørgensen-Hayashi catalyst (**XXIX**), in the presence of benzoic acid (**Scheme 8**).⁽²⁷⁾



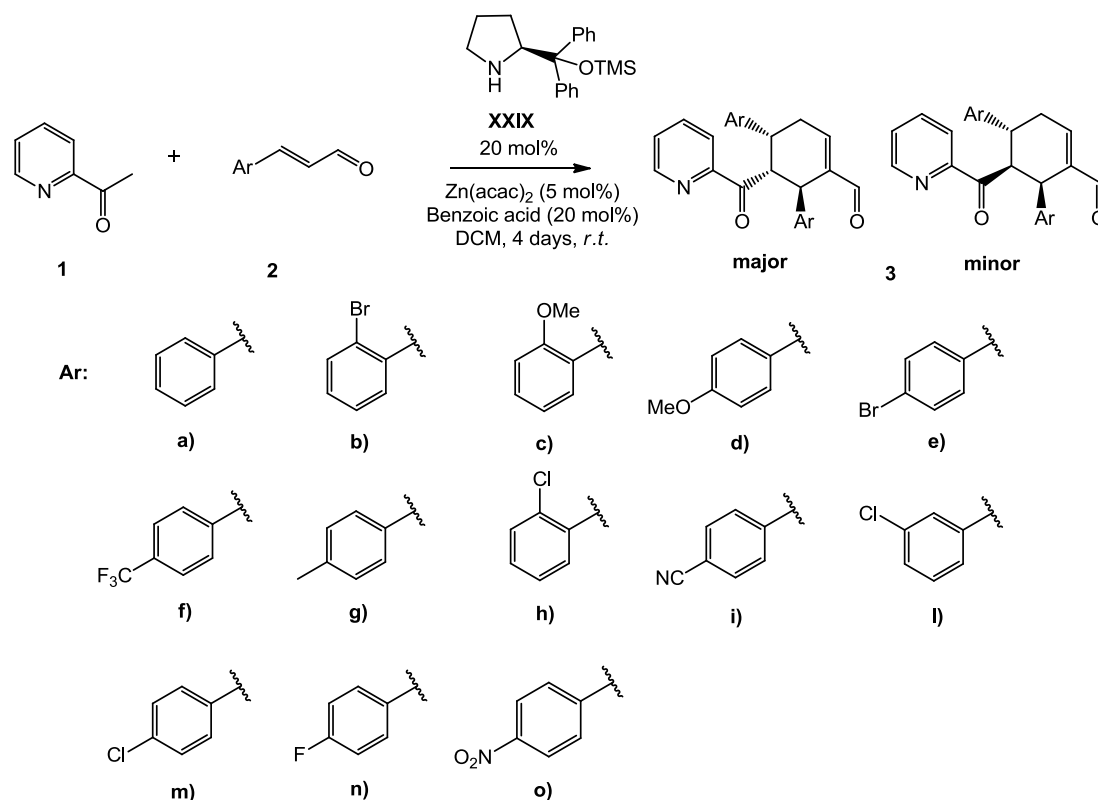
Scheme 8. Mechanism of spiro-cyclisation by Rios.

The mechanism consisted of two consecutive Michael additions catalysed by iminium ion intermediates. After the second Michael addition an intramolecular aldol condensation occurred, and thanks to the final dehydration it led to the desired product (**XLV**). In this project a similar kind of reaction mechanism was investigated, which will be described in the next section.

2 Aim of the thesis

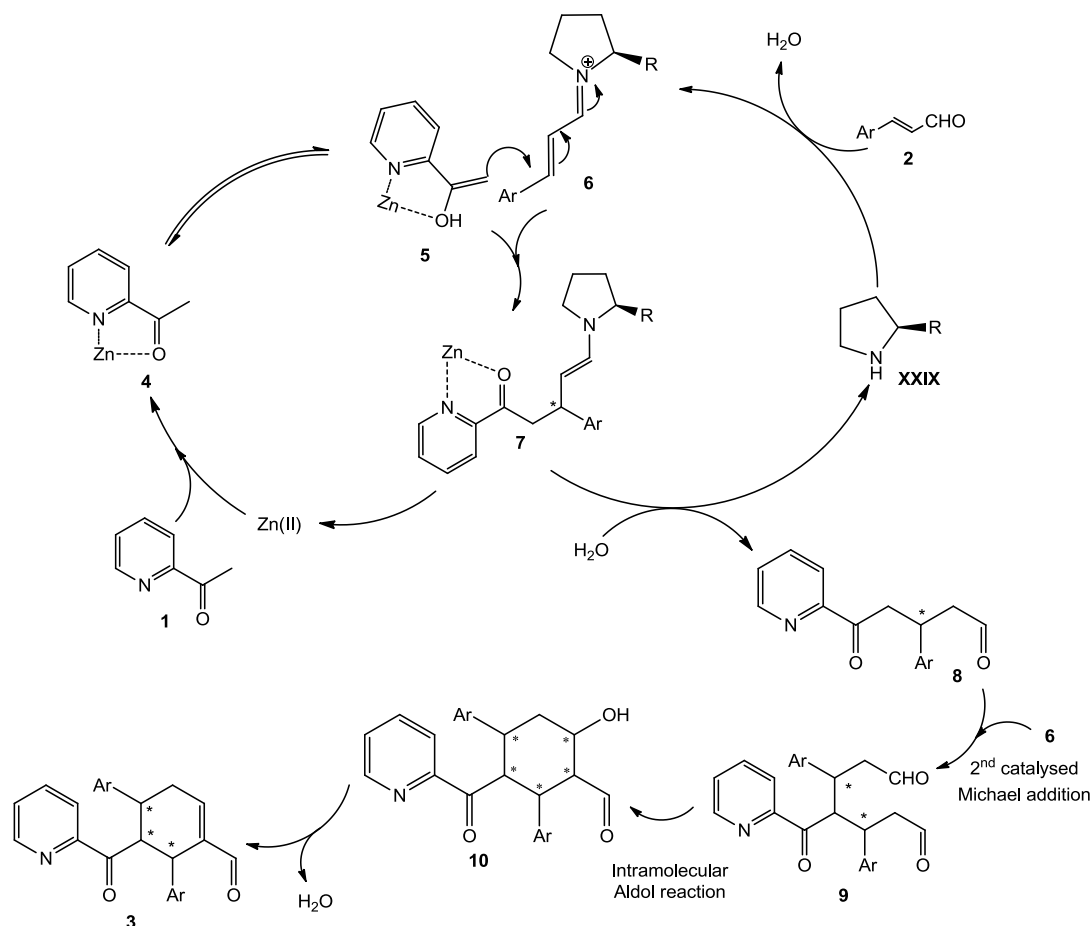
Based on the state of art regarding synergistic catalysis and domino reactions,^(19,27) this work was focused on the development of a new enantioselective strategy for the synthesis of pyridine derivatives, via domino Michael-Michael-Aldol reaction.

An asymmetric functionalization of 2-acetyl-pyridine (**1**) with α,β -unsaturated carbonyl compounds (**2**) by means of iminium ion and transition metal synergistic catalysis was reported. In order to verify the reproducibility and applicability of this reaction the synthesis using cinnamaldehydes bearing different substituents on the phenyl groups was studied (**Scheme 9**).



Scheme 9. Functionalization of 2-acetyl-pyridine with different cinnamaldehydes.

A mechanism involving synergistic catalysis was proposed, consisting in two catalytic cycles where the organic catalyst is the Jørgensen-Hayashi pyrrolidine (2-diphenyl-trimethylsilyloxy-methyl-pyrrolidine), and the other catalyst is a metal Lewis acid $\text{Zn}(\text{acac})_2$ (**Scheme 10**). Both configuration of Jørgensen catalyst (*R*) and (*S*) (**XXIX**) were used, in order to clarify the stereochemistry of the process.



Scheme 10. Proposed catalytic cycle of β -functionalization of 2-acetyl-pyridine with cinnamaldehyde.

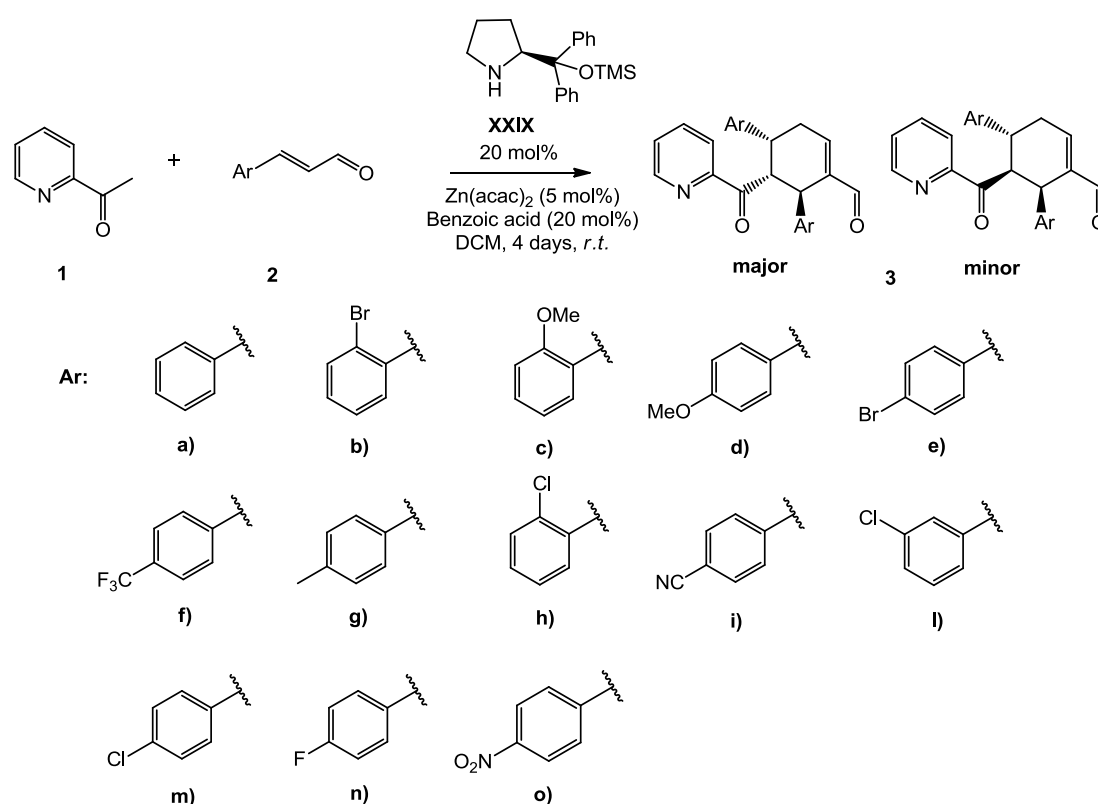
As evident from **Scheme 10**, the process occurs by Michael-Michael-Aldol reaction, yielding to the creation of three stereogenic centres.

A complete characterization of the final compounds (**3**) was performed, including the determination of the relative and absolute configurations, which were assigned by 2D-COSY and NOE-NMR experiments, and using Electronic and Vibrational Circular Dichroism (ECD and VCD) and comparing experimental results with that obtained by quantum mechanical calculations (TD-DFT and DFT).

3 Results and Discussion

3.1 Scope of reaction with enals

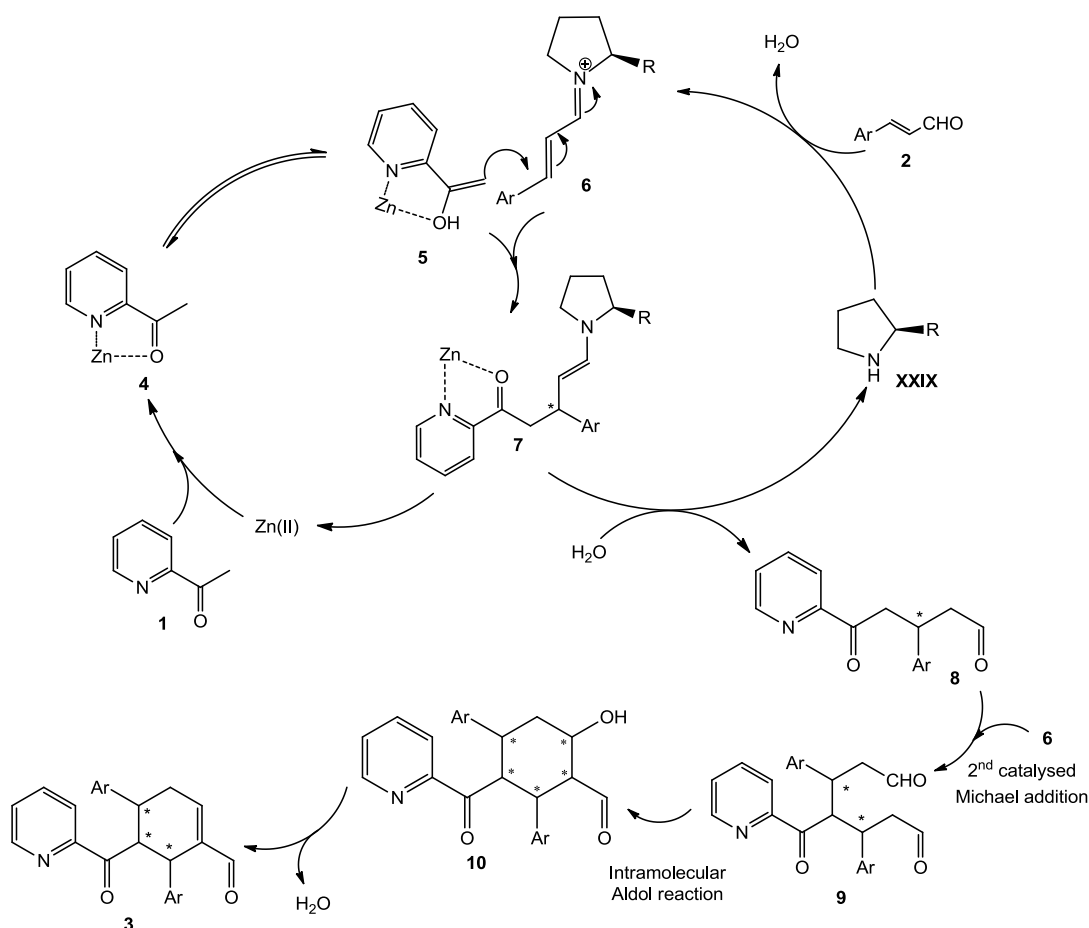
Using conditions determined from a previous reaction screening ($\text{Zn}(\text{acac})_2$ and benzoic acid dissolved in dichloromethane, at room temperature up to four days) a reaction scope employing cinnamaldehydes bearing different substituted phenyl groups (**2**) was studied (**Scheme 11**). The reactions were conducted using the enantiopure organo-catalysts **XXIX**, obtaining the two diastereoisomeric products (**3**).



Scheme 11. Functionalization of 2-acetyl-pyridine (**1**) with different cinnamaldehydes (**2**).

The reaction occurred through the synergistic catalytic mechanism shown in **Scheme 12**, using a metal Lewis catalyst and an organo-catalyst to activate the starting materials. The 2-acetyl-pyridine (**1**) interacts with the Lewis acid $\text{Zn}(\text{acac})_2$, which coordinates the oxygen and the nitrogen increasing the nucleophilicity of the α -carbon (**5**). Simultaneously, the Jørgensen catalyst reacts with the cinnamaldehyde yielding the iminium ion where the double bond is on the opposite side of the bulky substituent of the

secondary amine (**6**). Thanks to the iminium ion formation, the β -carbon is activated to the nucleophile attack, and the creation of the first chiral centre occurs (**7**). After the first Michael addition, the addition of a second cinnamaldehyde molecule occurs by the same catalysis of the first one and the second chiral centre is created (**9**). Finally, the intramolecular aldol condensation, followed by dehydration, leads to the desired product and creates the third chiral centre (**3**).



Scheme 12. Catalytic cycle of β -functionalization of 2-acetyl-pyridine (**1**) with cinnamaldehydes (**2**).

As shown in **Scheme 12** the product (**3**) contains three stereogenic centres: two of them were determined by the catalyst (the ones bound to the aryl groups) while configuration of the third one depended on the last intramolecular aldol reaction. For this reason, only two diastereoisomers (**major** and **minor**) were obtained, which are epimers at the central stereogenic centre. Using 2-acetyl-pyridine almost all the starting materials led to the double addition products (**3**). The obtainment of the mono-addition product (**8**) was expected using 2-propionyl-pyridine instead (**Paragraph 3.2**). The effect on conversion,

yield, diastereoisomeric ratio and enantiomeric excess of using different enals is summarized in **Table 1**.

Table 1. Scope of reaction with different cinnamaldehydes.

Entry	R	J.c. ^(a)	Conv. ^(b)	d.r. ^(c) (major : minor)	e.e. major ^(d) (%)	Yield ^(e) (major)
3a	H	<i>R</i>	57%	6:1	> 99	40%
3b	2-Br	<i>R</i>	87%	> 99%	> 99	28%
3c	2-OMe	<i>R</i>	68%	> 99%	_(f)	37%
3d	4-OMe	<i>R</i>	31%	4:1	97	30%
3e	4-Br	<i>R</i>	56%	5:1	_(f)	43%
3f	4-CF ₃	<i>R</i>	80%	5:1	>99	55%
3g	4-Me	<i>R</i>	31%	7:1	>99	10%
3h	2-Cl	<i>R</i>	> 99%	8:1	>99	57%
3i	4-CN	<i>R</i>	> 99%	4:1	>99	40%
3l	3-Cl	<i>R</i>	52%	5:1	>99	42%
3m	4-Cl	<i>R</i>	80%	5:1	>99	56%
3n	4-F	<i>R</i>	65%	5:1	>99	53%
3o	4-NO ₂	<i>R</i>	65%	6:1	>99	85%

(a) J.c. = Jørgensen-Hayashi catalyst configuration. (b) Diastereoisomeric ratios were calculated from the crude NMR comparing the aldehyde signals of the diastereoisomers. (c) Conversions were calculated from the crude NMR comparing the aldehyde signal of the starting cinnamaldehyde and the one of the product. (d) Enantiomeric excess was determined by chiral HPLC analysis as shown below in the text. (e) Yields were calculated from the isolated diastereoisomers after column chromatography. (f) products that are in course of analysis.

The data of **Table 1** show that the products were obtained with good to high diastereoisomeric ratios and excellent enantioselectivities. Hence, good results were obtained mostly with an electron-withdrawing group in the *para* position on the phenyl, for example **3f**, **3i** or **3o**. On the other hand, worse results appeared when an electron-

donating group was contained in the phenyl (**3d** and **3g**), increasing the yield of mono-addition by-product (as determined by $^1\text{H-NMR}$ spectroscopy). Furthermore, the presence of an electron-withdrawing substituent in the *ortho* position seemed to favour an higher diastereoselectivity (**3b** and **3h**), because the bulky group promoted only one diastereoisomer over the other when the formation of the second chiral centre occurred. Finally, moderate results were acquired with an electron-withdrawing group in the *meta* position (**3i** and **3c**).

Enantioselectivity and enantiomeric excesses were determined using chiral stationary phase (CSP) HPLC. In particular, the major diastereoisomers resulting from reactions with (*R*) and (*S*)-Jørgensen-Hayashi catalyst were analysed by CSP-HPLC using cellulose-based Chiralcel OD-H or OZ-H column. An example of HPLC results for the mixture of **3i** major enantiomers was reported in **Figure 5**.

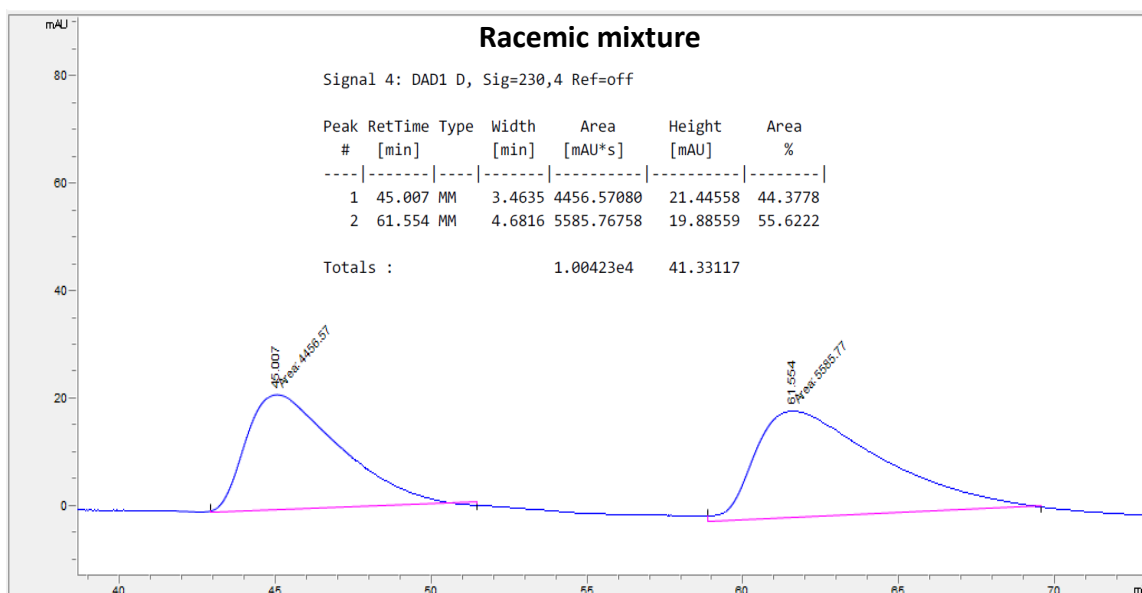
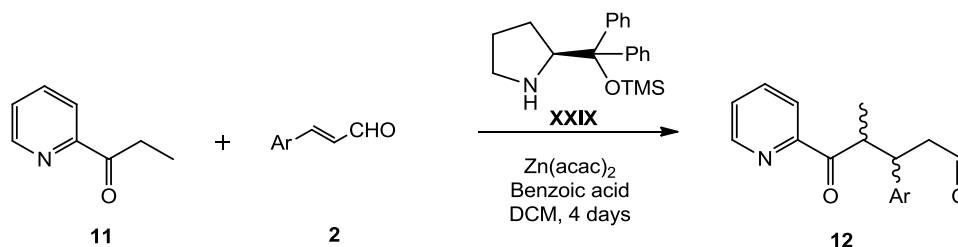


Figure 5. HPLC results for product **3i**-major. OD-H column, eluent mixture = *n*-hexane:*i*-PrOH 80:20, flow rate = 1 mL/min.

Comparing the product obtained with (*R*)-catalyst and the product obtained with (*S*)-catalyst, which exhibited the same $^1\text{H-NMR}$ spectrum, two single peaks at two different retention times could be observed, which means that two different enantiomers were obtained using Jørgensen-Hayashi catalyst with a different configuration. Furthermore, the enantiomeric excess was more than 99%, in almost all cases. HPLC analysis results for all the major products are reported in the experimental section (**Paragraph 6.2**).

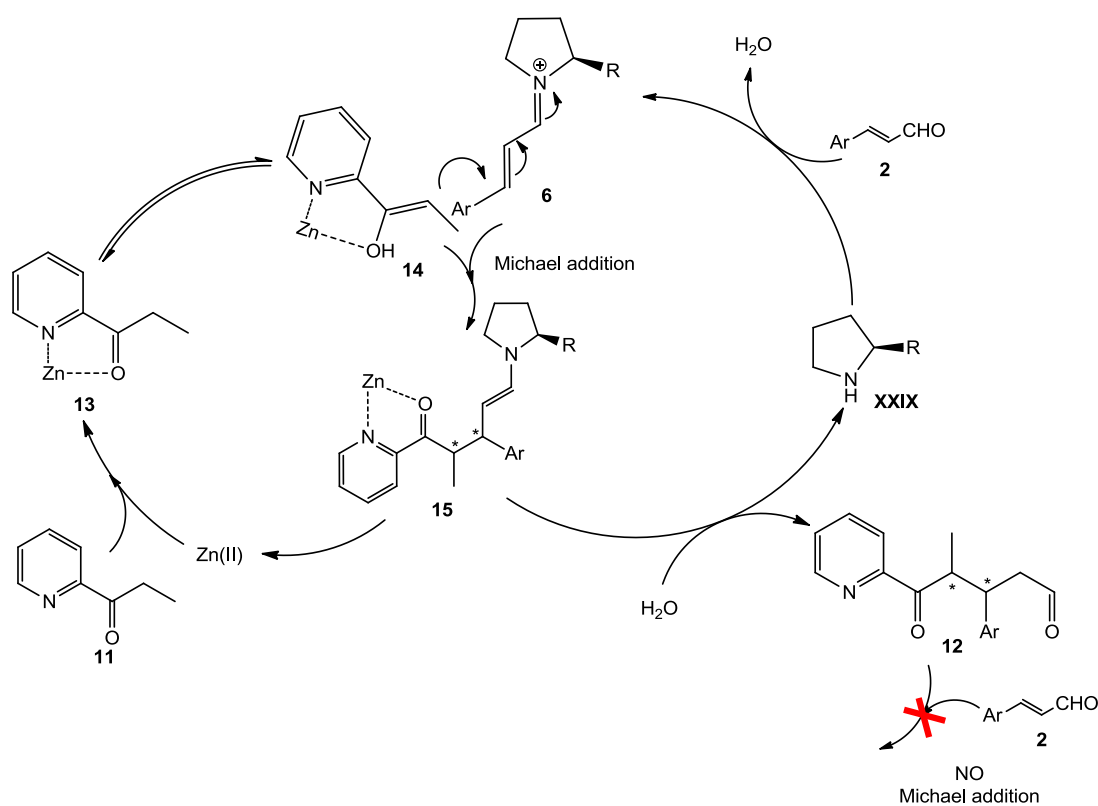
3.2 Reaction with 2-propionyl-pyridine

The reaction mechanism was verified by performing the reaction employing other acetylpyridines. As anticipated in the paragraph before, employing 2-propionyl-pyridine (**11**) no double addition product was obtained (**Scheme 13**). The products were analysed by NMR spectroscopy.



Scheme 13. Functionalization of 2-propionyl-pyridine (**16**) with cinnamaldehyde (**2**).

Only the mono-addition compound was observed (**12**), because the methyl group in α -position hinders the steric hindrance preventing the addition of a second molecule of cinnamaldehyde (**Scheme 14**).



Scheme 14. Catalytic cycle of β -functionalization of 2-propionyl-pyridine (**11**) with cinnamaldehyde (**2**).

Two reaction conditions using different metal catalysts were investigated as shown in **Table 2**. The conditions that gave the best conversion were found as the first combination with the $\text{Zn}(\text{acac})_2$ as Lewis acid.

Table 2. Screening of reaction with propionyl-pyridine using different catalysts.

Solvent	Lewis acid	J.c.	1 day		4 days	
			Conv.	d.r. (maj.:min.)	Conv.	d.r. (maj.:min.)
Toluene	$\text{Zn}(\text{acac})_2$	R	74%	3.4:1	74%	2:1
Toluene	$\text{Ni}(\text{OAc})_2 \cdot 4\text{H}_2\text{O}$	R	67%	4:1	62%	1.36:1

3.3 Identification and characterization

In order to study the stereochemistry and the mechanism of the reaction it was important to identify the relative and the absolute configuration of the two diastereoisomers obtained from the reaction. The analysis were carried out for the diastereoisomers of compounds **3i** and **3f**, and successively extended to the other products. The relative configuration of the products was determined by means of 2D-COSY and NOE-NMR experiments.

Moreover, the standard method used to assign the absolute configuration is X-ray anomalous scattering, but in the last years other methods that do not require the preparation of enantiopure single crystals showed to be reliable and feasible. They are based on chiro-optical techniques such as optical rotation, Electronic Circular Dichroism (ECD) and Vibrational Circular Dichroism (VCD), supported by quantum mechanical TD-DFT and DFT calculations (see **Appendix**). In this case, the absolute configuration of **3i** diastereoisomers was assigned by ECD spectroscopy, while the absolute configuration of **3f** diastereoisomers was determined by VCD spectroscopy.

3.3.1 HPLC purification

Before assigning the configuration, the major and minor diastereoisomers of compound **3i** must be purified by means of semi-preparative HPLC. The HPLC purification of the major diastereoisomer of **3i** was performed on CSP-HPLC, using a cellulose-based HPLC column (Phenomenex *Cellulose2*, **Figure 6**).

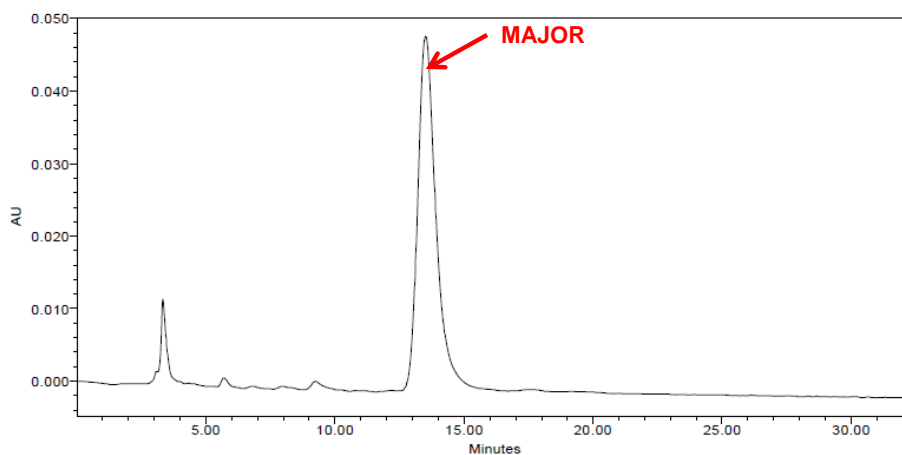


Figure 6. Semi-preparative HPLC of **3i-major** fraction with Phenomenex *Cellulose2* Column. Injection Volume = 10 μ L, Run Time = 32 min, eluent mixture = *n*-hexane/*i*-PrOH 30:70, λ = 254 nm, flow rate = 5 mL/min, $t_{r(\text{major})}$ = 14 min.

The minor diastereoisomer was obtained starting from a mixture of the two diastereoisomers containing about 60% of the minor (**Figure 7**). Reverse phase HPLC was used with a *LunaC18* column and acetonitrile/H₂O as eluent.

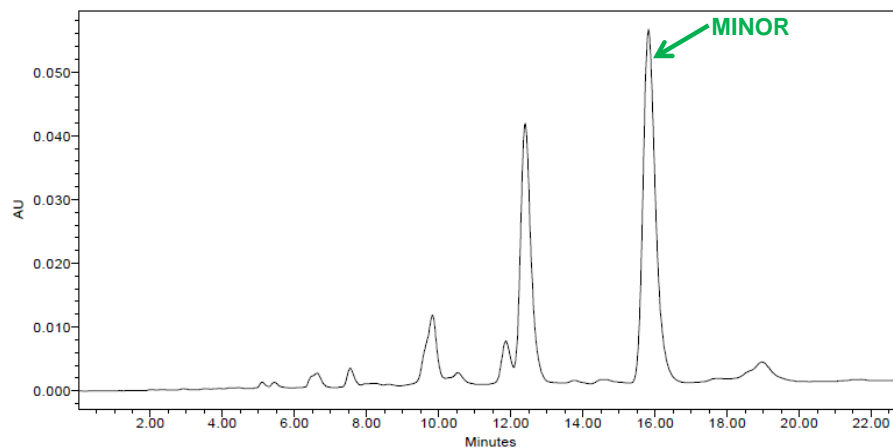


Figure 7. Semi-preparative HPLC of **3i-minor** fraction with *LunaC18* Column. Injection Volume = 10 μ L, Run Time = 23 min, eluent mixture = azeotropic ACN/H₂O mixture:H₂O 40:60, λ = 254 nm, flow rate = 5 mL/min, $t_{r(\text{minor})}$ = 16 min.

After purifying the two diastereoisomers of **3i** by HPLC, the interest was focused on the determination of the relative and the absolute configuration of each diastereoisomer.

3.3.2 Characterization of compound **3i-major**

The ¹H-NMR spectrum of compound **3i-major** is reported in **Figure 8**.

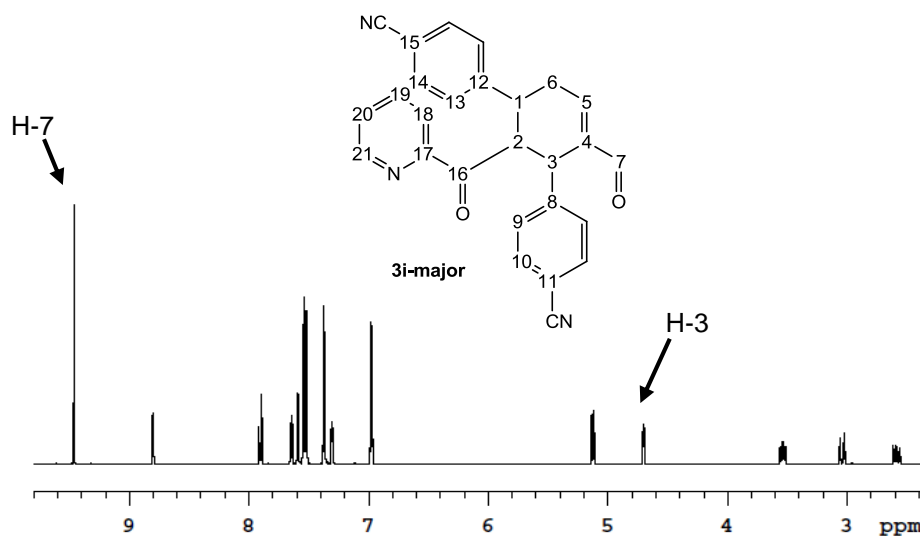


Figure 8. ¹H-NMR of compound **3i-major** (600 MHz in CD₃CN).

The chemical shift of **H-3** was assigned at 4.70 ppm, because it was the only doublet in the aliphatic region for the coupling with **H-2**. Starting from this, it was possible to

assign the signals of all the protons in the aliphatic area by means of 2D-COSY experiment (**Figure 9**).

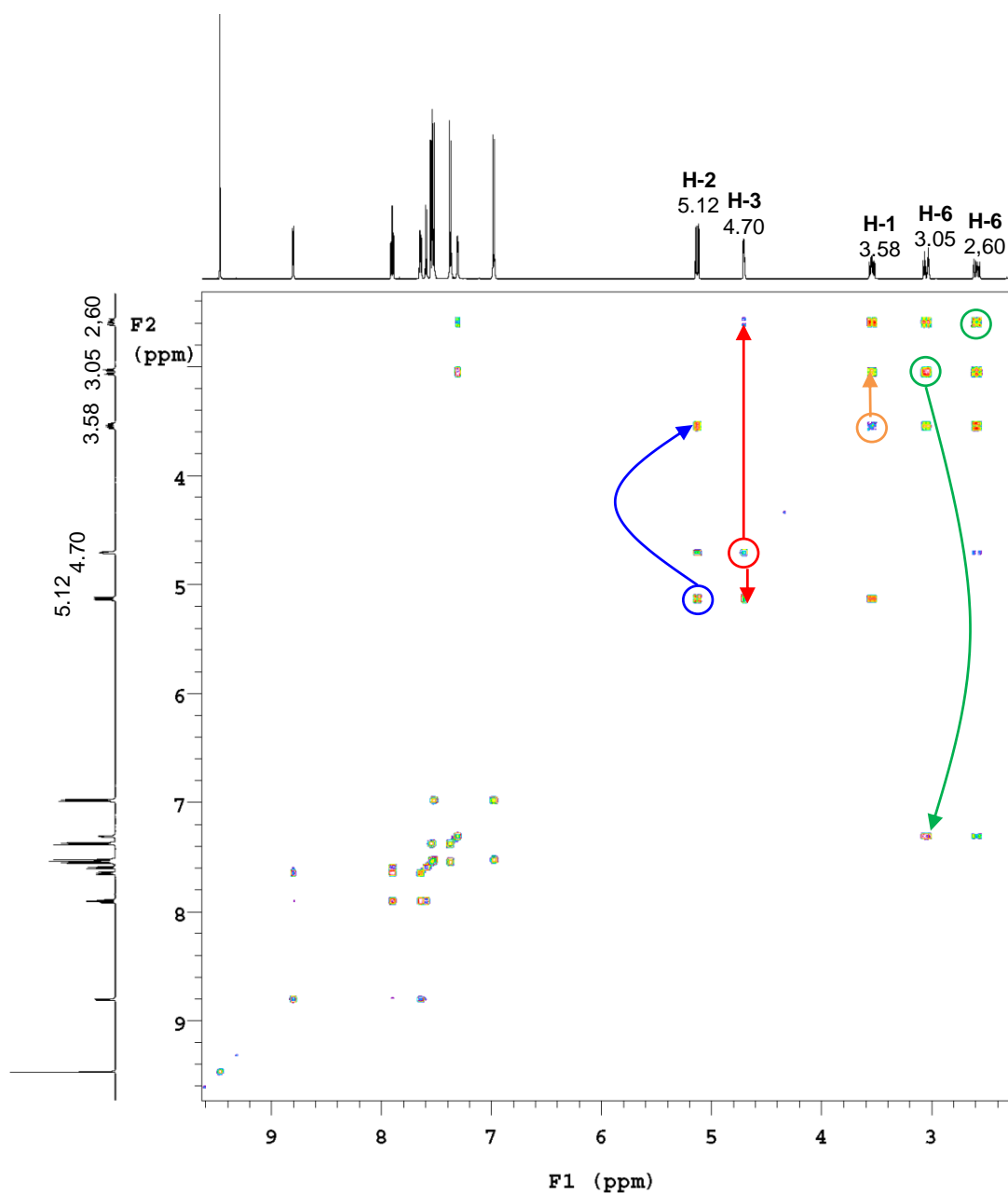


Figure 9. 2D-COSY experiment of compound **3i-major** (600 MHz in CD₃CN), showing correlation between **H-3** and **H-2** (red), **H-2** and **H-1** (blue), **H-1** and **H-6** (orange) and **H-6** and **H-5** (green).

H-2 was identified at 5.12 ppm from the correlation with **H-3**. In the same way, **H-1** signal was determined at 3.58 ppm by the correlation with **H-2** and also diastereotopic protons **H-6a** and **H-6b** at 3.05 ppm and 2.58 ppm were identified by the correlation with **H-1**. The discrimination of the chemical shifts of **H-6a** and **H-6b** was made in a second moment by means of NOE-NMR experiments (See below in the text).

Relative configuration

The relative configuration was then assigned on the base of NOE-NMR experiments. A first experiment was run by saturation of **H-3** signal (**Figure 10**).

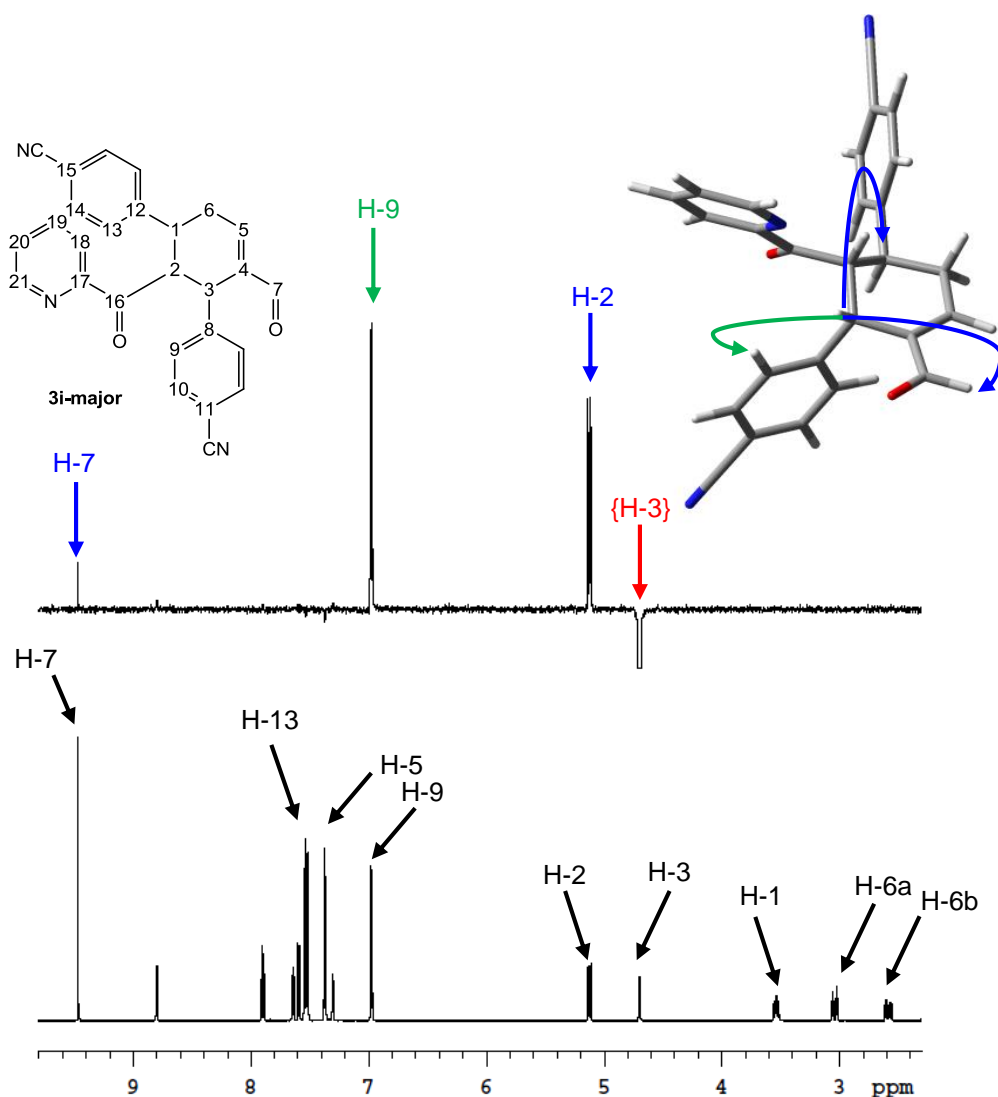


Figure 10. Top: NOE-NMR spectrum obtained from the irradiation of **H-3** (600 MHz in CD₃CN). Red: irradiated signal, green: control signals, blue: signals of interest. Bottom: ¹H-NMR spectrum.

The experiment showed that **H-3** presented a large NOE effect with **H-2** signal at 5.12 ppm. This led to the conclusion that **H-3** and **H-2** are positioned on the same side of the molecule (*syn* position). Furthermore, the spectrum showed that **H-3** was close also to the aromatic signal at 6.98 ppm, which represented the *ortho*-positioned protons of the 3-aryl group (**H-9**). Finally, a weak NOE effect between **H-3** and aldehydic proton **H-7**, at 9.45 ppm, was observed. This first experiment fixed the relative stereochemistry of the two stereogenic carbons **C-2** and **C-3**.

A second experiment was obtained by saturating **H-2** signal at 5.12 ppm (**Figure 11**). As expected NOE effect between **H-2** and **H-3** at 4.70 ppm (control signal) was observed.

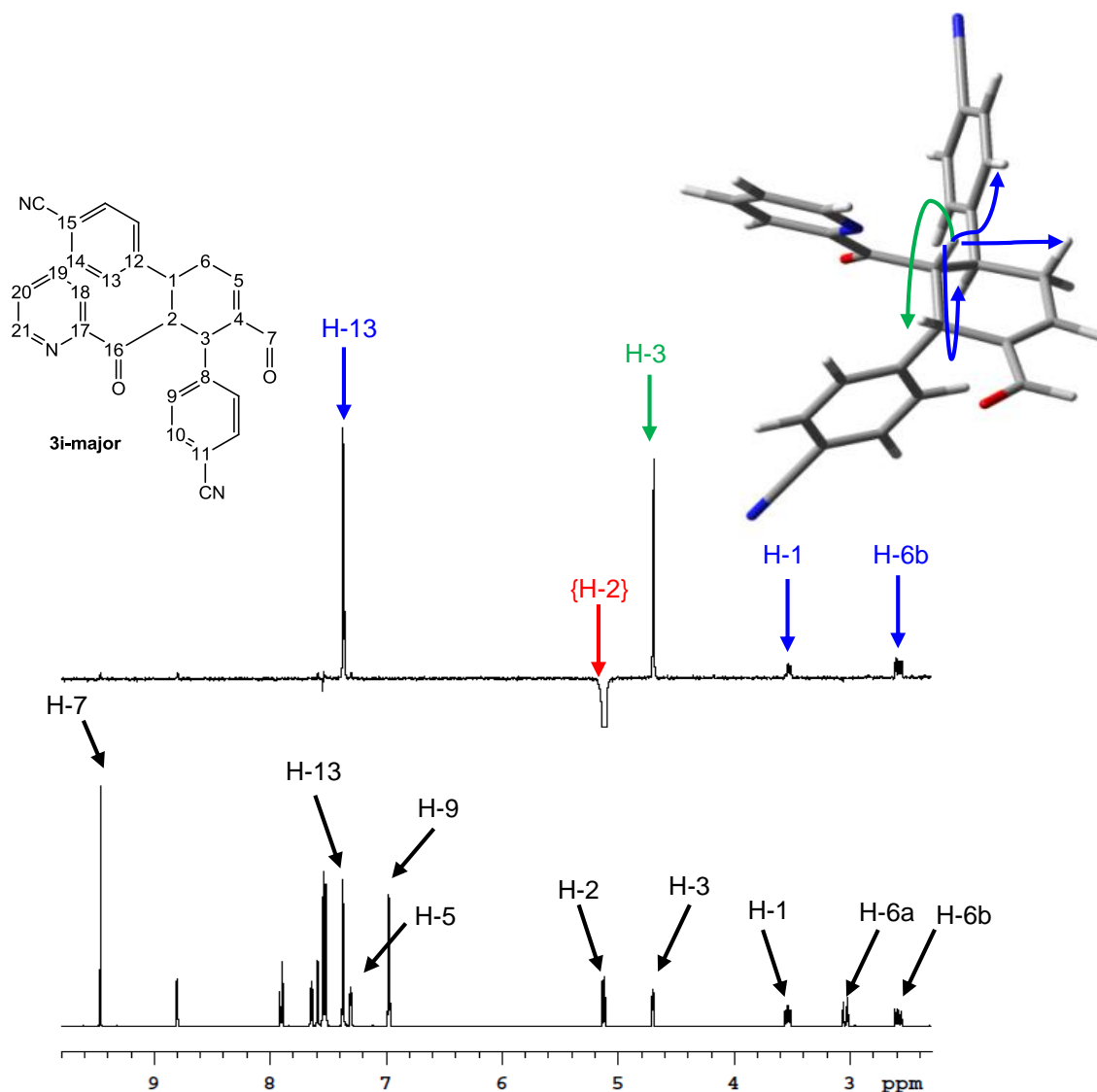


Figure 11. Top: Aliphatic region of NOE-NMR spectrum obtained from the irradiation of **H-2** (600 MHz in CD₃CN). Red: irradiated signal, green: control signals, blue: signals of interest. Bottom: ¹H-NMR spectrum.

The spatial proximity between **H-2** and *ortho* protons of the 1-aryl group **H-13** (7.36 ppm) was observed. This suggested that 1-aryl group and **H-2** were in the *syn* position. The spectrum showed also a weak NOE correlation with the signal at 2.60 ppm, which was assigned to the diastereotopic proton **H-6b** on the same side of **H-2**. The very small NOE effect between **H-2** and **H-1** (3.60 ppm) confirmed that these two aliphatic protons were in the *anti* relationship. This disposition is further confirmed by the very large coupling constant connecting **H-2** with **H-1** (12.5 Hz), suggesting a dihedral angle close

to 180°. Thus, this spectrum determined the stereochemistry of **C-1** and allowed distinguishing the two diastereotopic protons **H-6a** and **H-6b**.

In the third NOE-NMR experiment (**Figure 12**), the **H-1** signal at 3.60 ppm was saturated. The NOE effects observed confirmed the previous suggestions; **H-1** showed spatial proximity with 3.05 ppm signal (**H-6a**), with 6.98 ppm signal (**H-9**), with 7.30 ppm signal (**H-13**) and a weak NOE effect with **H-2**.

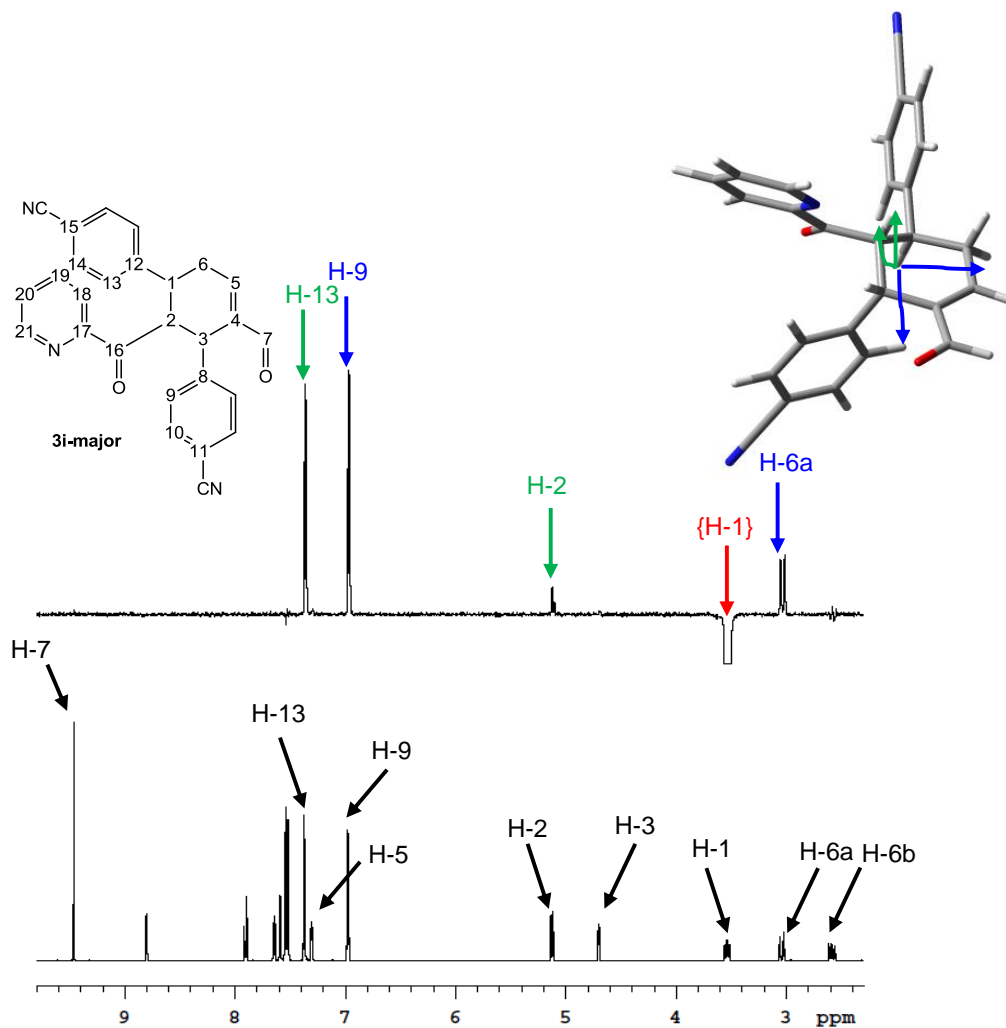


Figure 12. Top. Aliphatic region of NOE-NMR spectrum obtained from the irradiation of **H-1** (600 MHz in CD₃CN). Red: irradiated signal, green: control signals, blue: signals of interest. Bottom: ¹H-NMR spectrum.

Finally, saturation of aldehydic signal at 9.45 ppm (**H-7**) was performed, in order to obtain preliminary information about the conformation of aldehydic moiety (**Figure 13**).

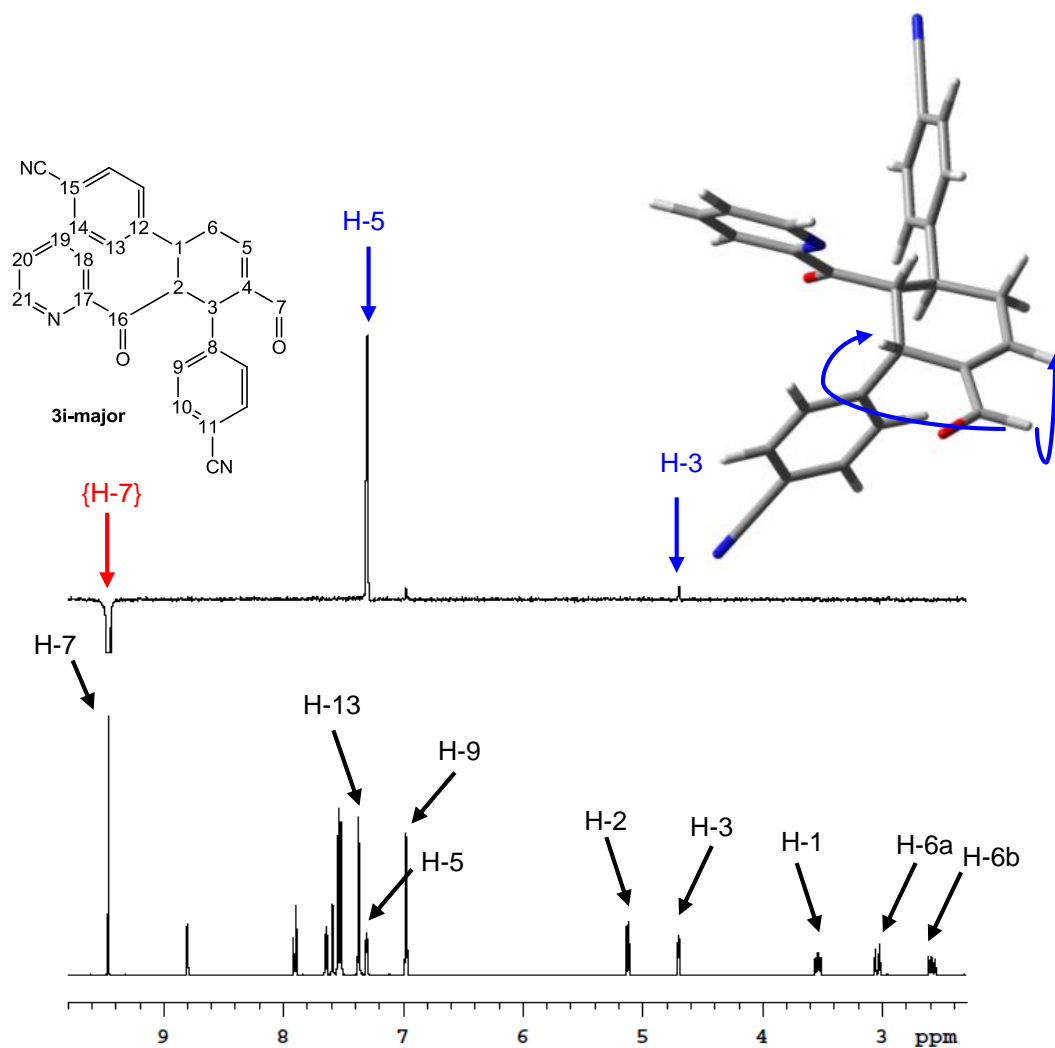


Figure 13. Top: NOE-NMR spectrum obtained from the irradiation of **H-7** (600 MHz in CD_3CN). Red: irradiated signal, blue: signals of interest. Bottom: ^1H -NMR spectrum.

Given the large NOE observed on **H-5** and the weak NOE on **H-3**, the aldehydic proton is mainly localized close to **H-5** (7.30 ppm).

With the information collected from the NOE-NMR experiments, it was possible to assign the $1S^*,2R^*,3S^*$ relative configuration of the compound **3i-major** (**Figure 14**).

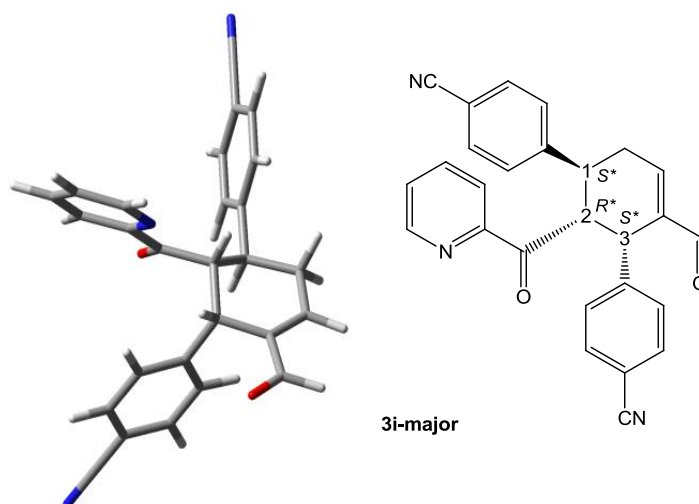


Figure 14. 3D structure (left) and relative configuration (right) of compound **3i-major**.

Conformational analysis

Having assigned the $1S^*,2R^*,3S^*$ relative configuration of **3i-major** diastereoisomer, the project was focused on conformational analysis. In this case the molecule was rather rigid but some degrees of freedom could be identified, such as the rotation of the aldehydic group, the rotation of the pyridine group and rotation of carbonyl group. A conformational search was preliminarily performed by means of molecular mechanics force field (MMFF 94). The conformations with lower energy found were then optimized by DFT computations, which were carried out at the B3LYP/6-31G(d) level of theory. The $1S,2R,3S$ absolute configuration was assumed for the **3i-major** diastereoisomer and eight conformations were identified (**Figure 15**). For all the optimized geometries, frequency analysis was performed to confirm they were true energy minima (no imaginary frequencies were found).

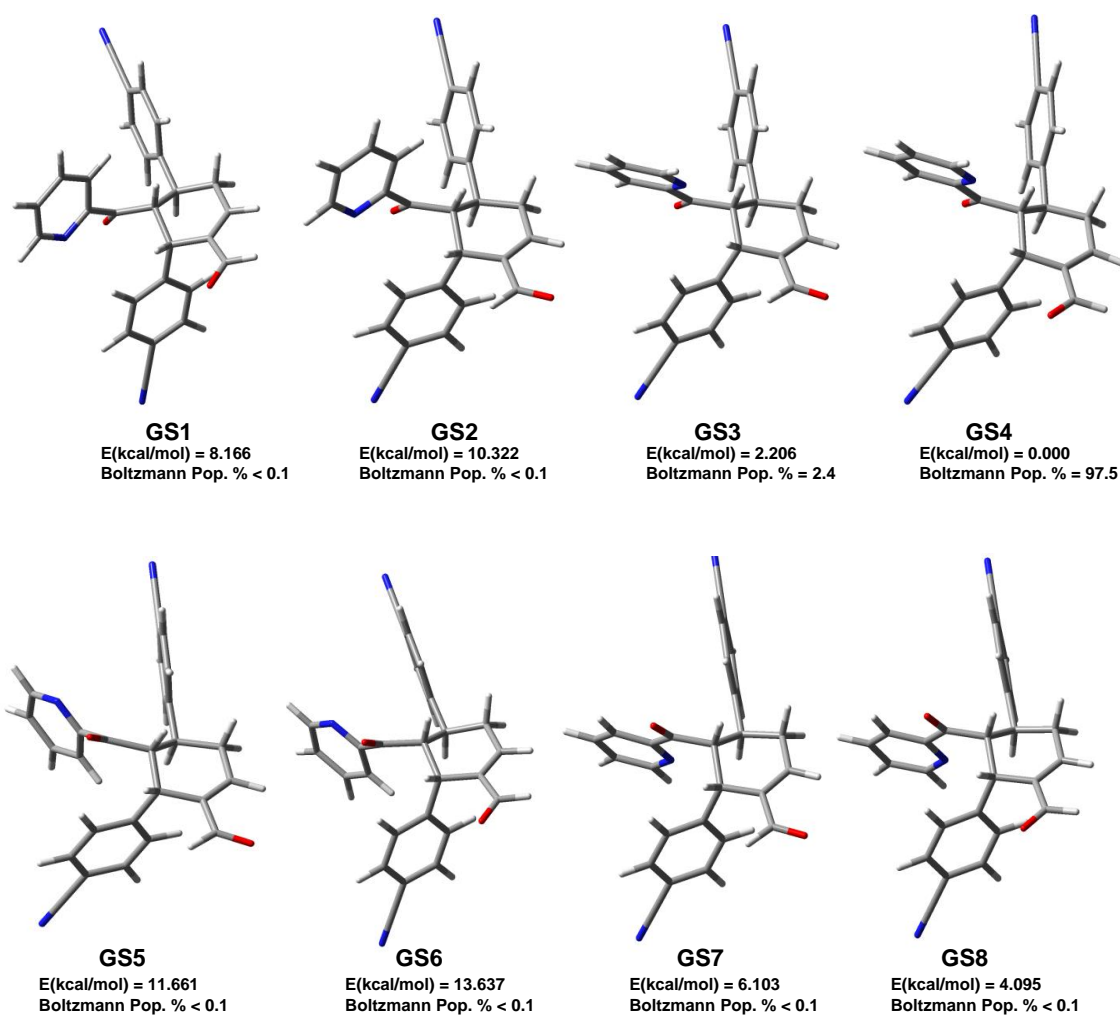


Figure 15. Conformations found by DFT calculations, optimized at the B3LYP/6-31G(d) level and relative energies of compound **3i-major**.

The results asserted that only conformations **GS4** and **GS3** should be appreciably populated (Boltzmann population is higher than 0.5%). These two conformations correspond to the 180° rotation of the CHO moiety.

Absolute configuration

Once the 1*S**,2*R**,3*S** relative configuration of compound **3i-major** was found, the absolute configuration had to be assigned by means of ECD technique.

The ECD spectrum of **3i-major** was recorded in the UV region between 180 nm and 400 nm (**Figure 16**). The spectrum showed a positive broad band at 275 nm, two positive signals centred at 245 nm and 210 nm and two negative bands at 225 nm and 200 nm. The most intense region of the spectrum was the positive branch at 245 nm.

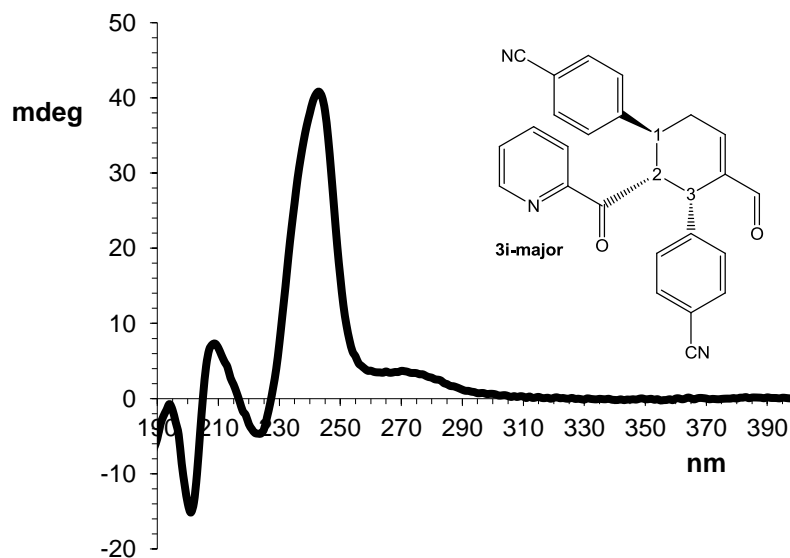


Figure 16. Experimental ECD spectrum of **3i-major** in acetonitrile. See the details in the **Section 6**.

The simulations of the ECD spectra were carried out using the TD-DFT method and using the populated geometries **GS3** and **GS4** previously optimized at the B3LYP/6-31G(d) level of theory. In order to have redundancy of data and to get more reliability, calculations were performed using four different functionals: the hybrid functionals CAM-B3LYP, BH&HLYP, M06-2X and ω B97XD that includes empirical dispersion (**Figure 17**). The basis set employed was 6-311++G(2d,p) for all the functionals.

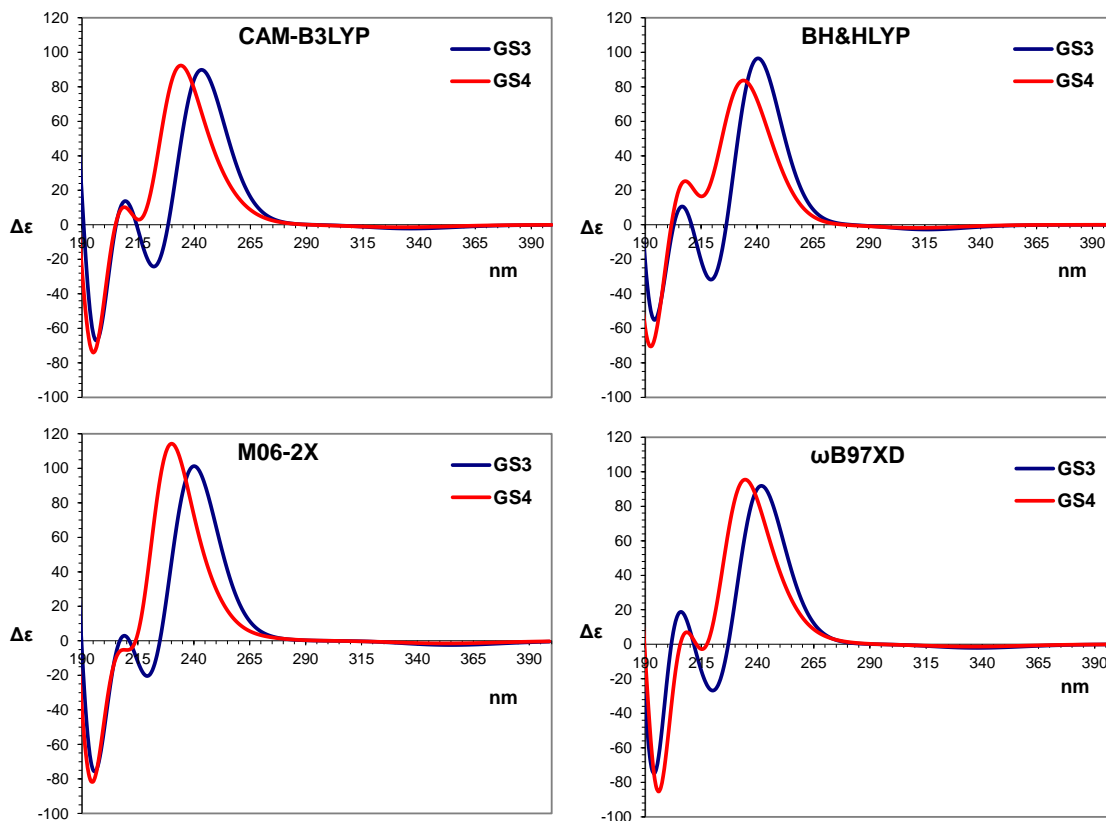


Figure 17. TD-DFT simulated spectra of the two conformations **GS3** and **GS4** of **3i-major** performed using functionals CAM-B3LYP, BH&HLYP, M06-2X, ω B97XD and the 6-311++G(2d,p) basis set. The spectrum was obtained using a 0.25 eV line width at half height.

All the simulation showed a positive band at 235-245 nm, a positive signal at about 210 nm and a negative one around 200 nm, in agreement with the experimental results (shown in **Figure 16**). In all calculations, **GS3** presented a more intense Cotton effect between 215 and 225 nm, while **GS4** did not exhibit a negative band in that region. In order to obtain the calculated spectrum to be compared with the experimental ECD, TD-DFT spectra of both conformations were weighted according with the populations determined by Boltzmann distribution. In this case, the simulations obtained for the two conformation were not very different, so errors in the conformational ratio did not change the final spectrum at a great extent. **Figure 18** shows the comparison between the averaged simulated spectra obtained for each functional (coloured lines), compared with the experimental spectrum (black line).

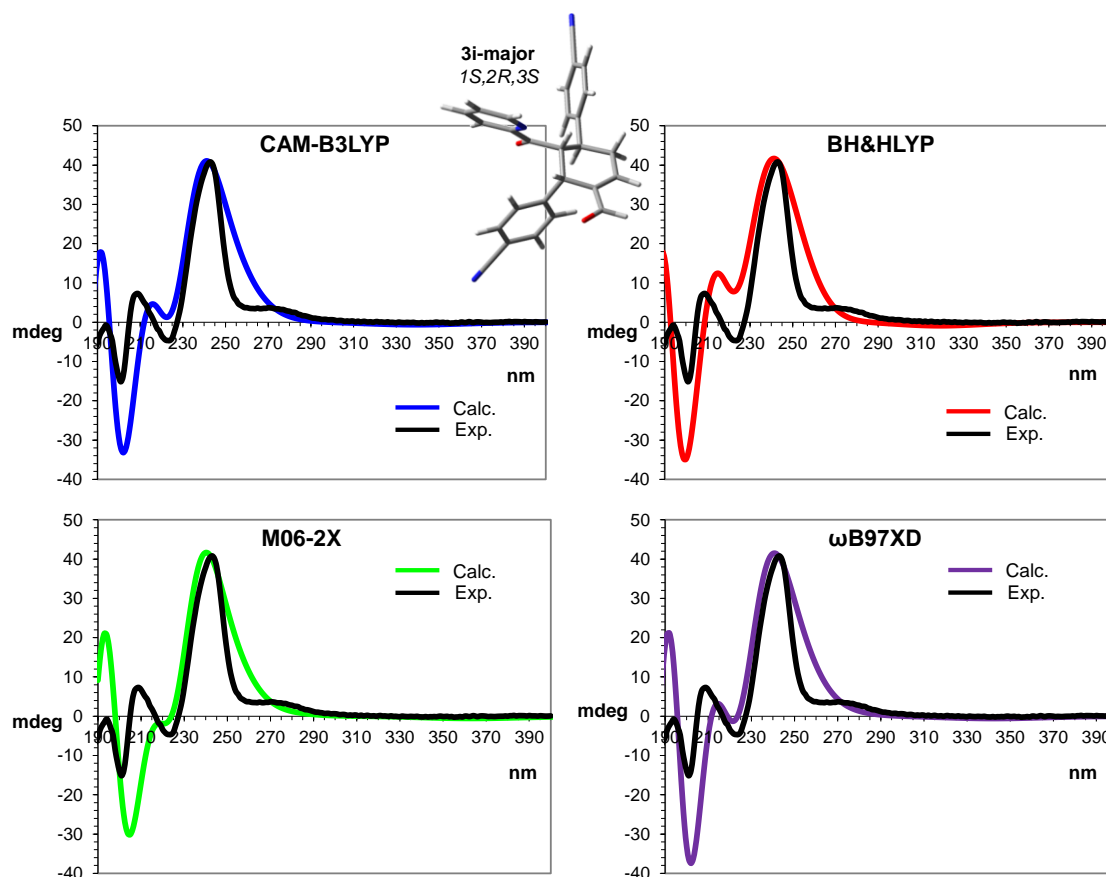


Figure 18. TD-DFT simulations compared with the experimental ECD spectrum of **3i-major**. Black line: experimental spectrum. Coloured lines: simulated spectra. All the simulations were carried out for the *1S,2R,3S* absolute configuration.

The simulated spectra were scaled and shifted in order to obtain the best overlap with the experimental one (y axes scaling factors: 0.45, 0.5, 0.44, 0.37, x axes shift factors: 7, 7, 8, 10 nm for CAM-B3LYP, BH&HLYP, ω B97XD, M06-2X, respectively). The comparison between all the simulated averaged spectra with experimental one was very good and the *1S,2R,3S* absolute configuration can be reliably assigned to **3i-major** (Figure 19).

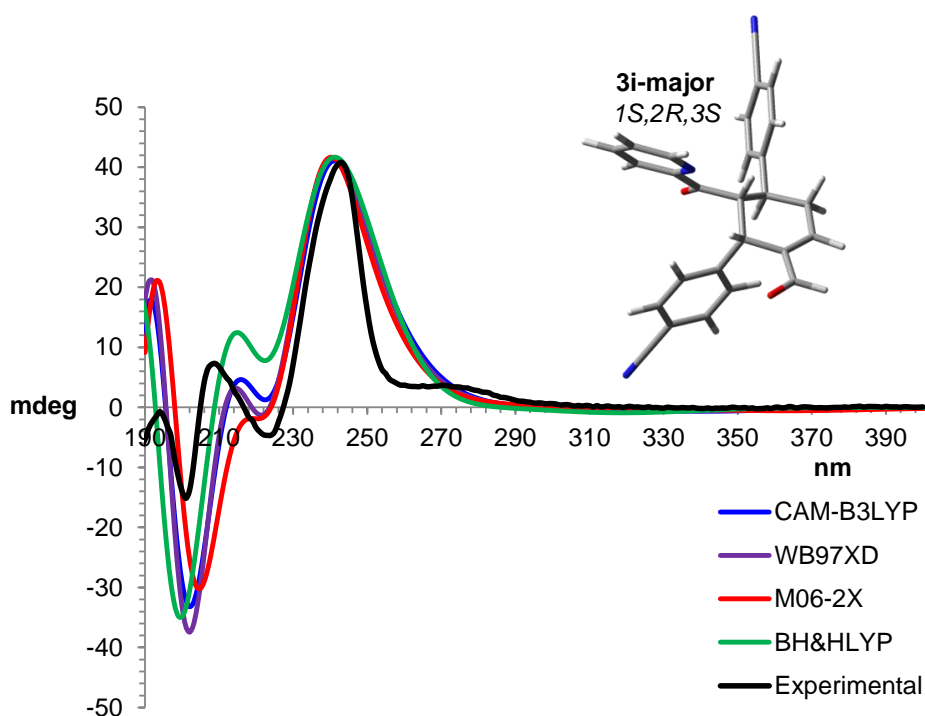


Figure 19. Comparison between the sum of all weighted simulated spectra and experimental spectrum of compound **3i-major**.

3.3.3 Characterization of compound **3i-minor**

In order to assign the relative configuration of compound **3i-minor** the same procedure used for **3i-major** was actuated. The chemical shift of **H-3** was assigned to the broad signal at 4.40 ppm that is the only aliphatic signal that shows HMBC correlation with the aldehydic carbon **C-7** (**Figure 20**).

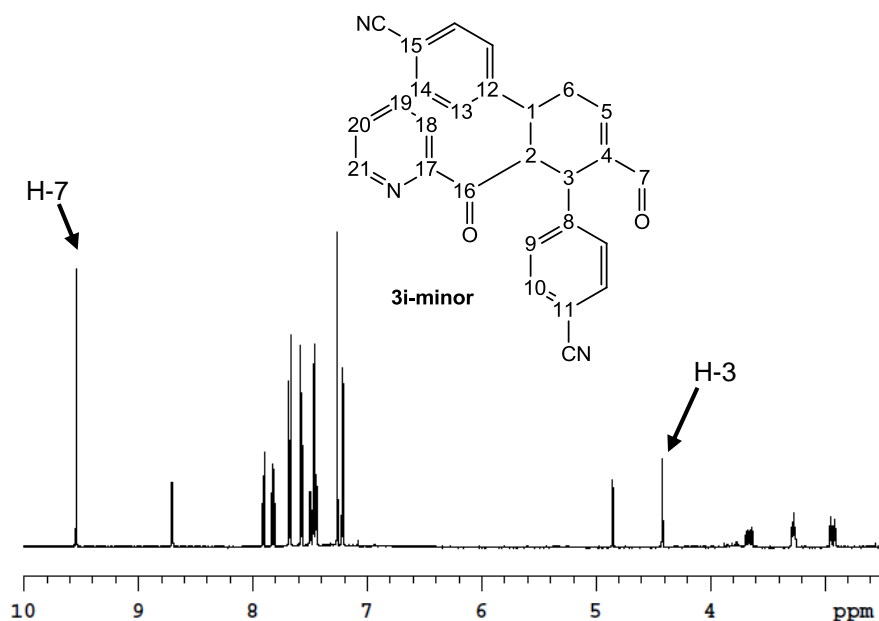


Figure 20. $^1\text{H-NMR}$ spectrum of compound **3i-minor** (600 MHz in CDCl_3).

Starting from **H-3** signal, it was possible to assign the peaks of all the protons in the aliphatic region by means of 2D-COSY experiment (**Figure 21**). **H-2** was identified from the correlation with **H-3** in the signal at 4.83 ppm. In the same way, **H-1** signal was determined at 3.20 ppm by the correlation with **H-2** and also the diastereotopic protons **H-6a** and **H-6b** at 3.60 ppm and 2.98 ppm were identified thanks to the correlation with **H-5**. The discrimination of chemical shifts of **H-6a** (equatorial position) and **H-6b** (axial position) was made by means of NOE-NMR experiments (see below in the text).

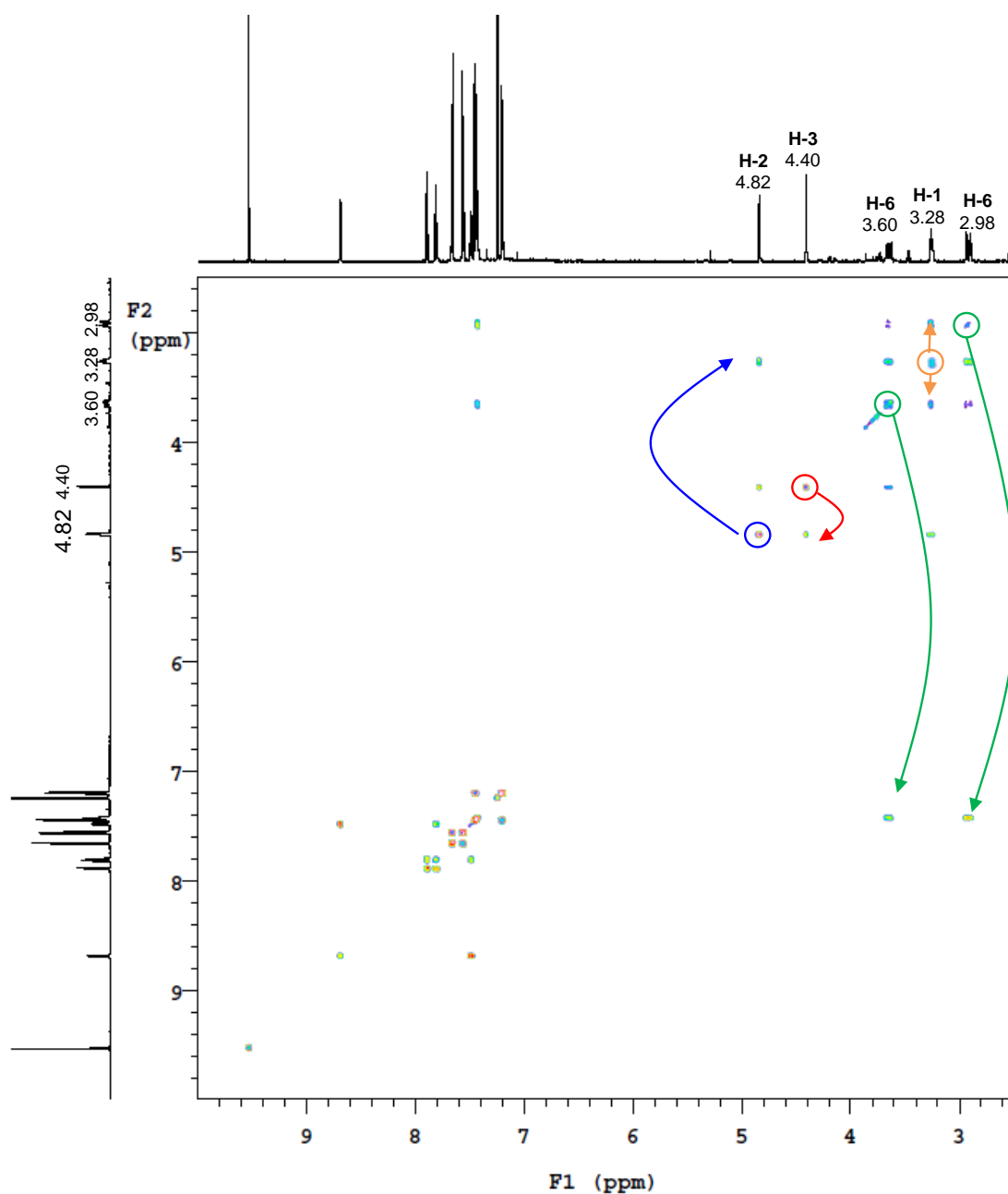


Figure 21. Aliphatic region of the 2D-COSY experiment of compound **3i-minor** (600 MHz in CDCl₃), showing correlation between **H-3** and **H-2** (red), **H-2** and **H-1** (blue), **H-1** and **H-6** (orange) and **H-6** and **H-5** (green).

Relative configuration

As well as for **3i-major**, a first NOE-NMR experiment was performed by saturating **H-3** signal (**Figure 22**).

Control signals from the aldehydic proton **H-7** (9.55 ppm) and from aromatic protons of the 3-aryl-group (7.48 ppm) were observed. Furthermore, a NOE effect was present on the **H-2** signal at 4.82 ppm.

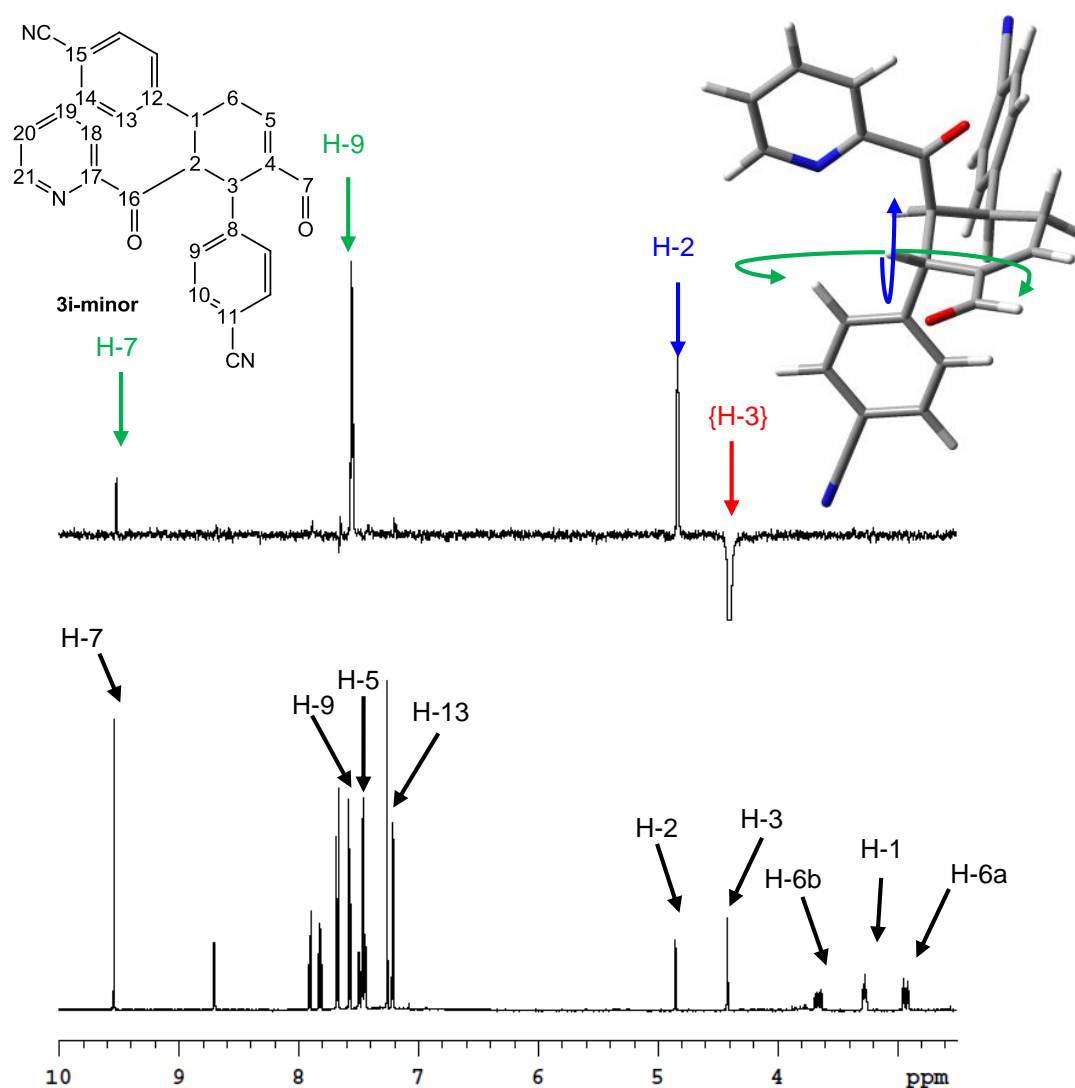


Figure 22. Top: Aliphatic area of NOE-NMR spectrum obtained from the irradiation of **H-3** (600 MHz in CDCl_3). Red: irradiated signal, green: control signals, blue: signals of interest. Bottom: $^1\text{H-NMR}$ spectrum.

A second experiment saturating **H-2** signal (4.83 ppm) was then performed as shown in **Figure 23**. Proton **H-2** gave NOE effect on **H-3** (control signal), as expected. Differently from the major product, a large NOE effect was observed on the aromatic protons **H-9** (7.40 ppm). This suggested that **H-2** and **H-9** were close in the space. Furthermore, the

spectrum showed intense NOE effect with the aliphatic signal at 3.28 ppm of **H-1**, and a weak enhancement on the aromatic protons of 1-aryl-group at 7.20 ppm (**H-13**, *para* system). This spectrum suggested the relative stereochemistry of **C-1**, **C-2** and **C-3**; in fact, **H-2** and **H-1** must be positioned on the same side of the molecule (*syn* position), due to the large NOE effect. Differently, **H-3** and **H-2** were in the *anti* position, since **H-2** showed a large NOE effect on **H-9**.

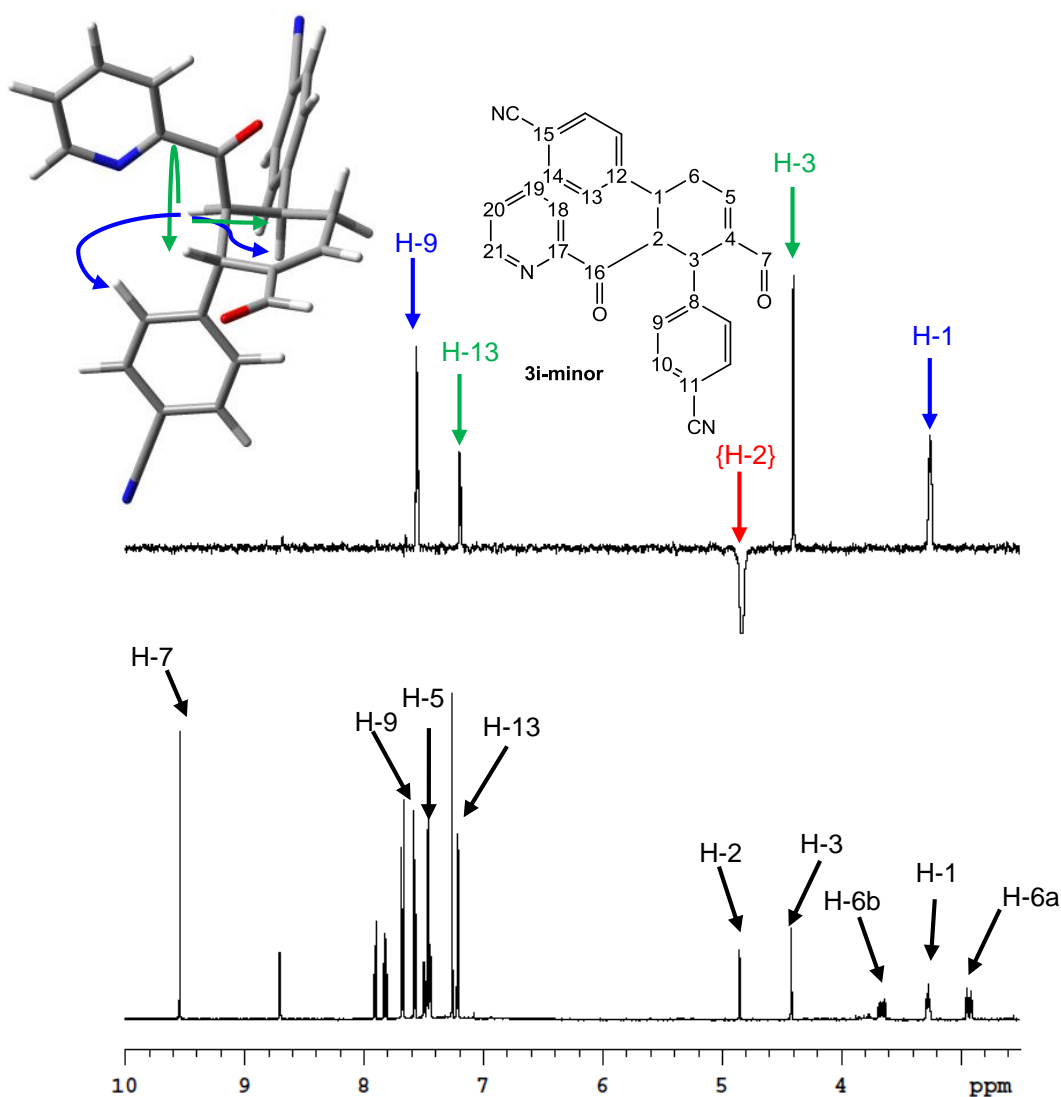


Figure 23. Top: NOE-NMR spectrum obtained from the irradiation of **H-2** (600 MHz in CDCl_3). Red: irradiated signal, green: control signals, blue: signals of interest. Bottom: ^1H -NMR spectrum.

In order to have redundant information about the relative configuration a “control” NOE-NMR experiment was acquired by saturation of **H-1** (**Figure 24**). NOE effect on **H-2**, **H-13**, and **H-6a** (2.98 ppm) was obtained, as expected. In addition, correlation between **H-1** and **H-9** reinforced the hypothesis made before that **H-3** and **H-1** are in the *anti* position.

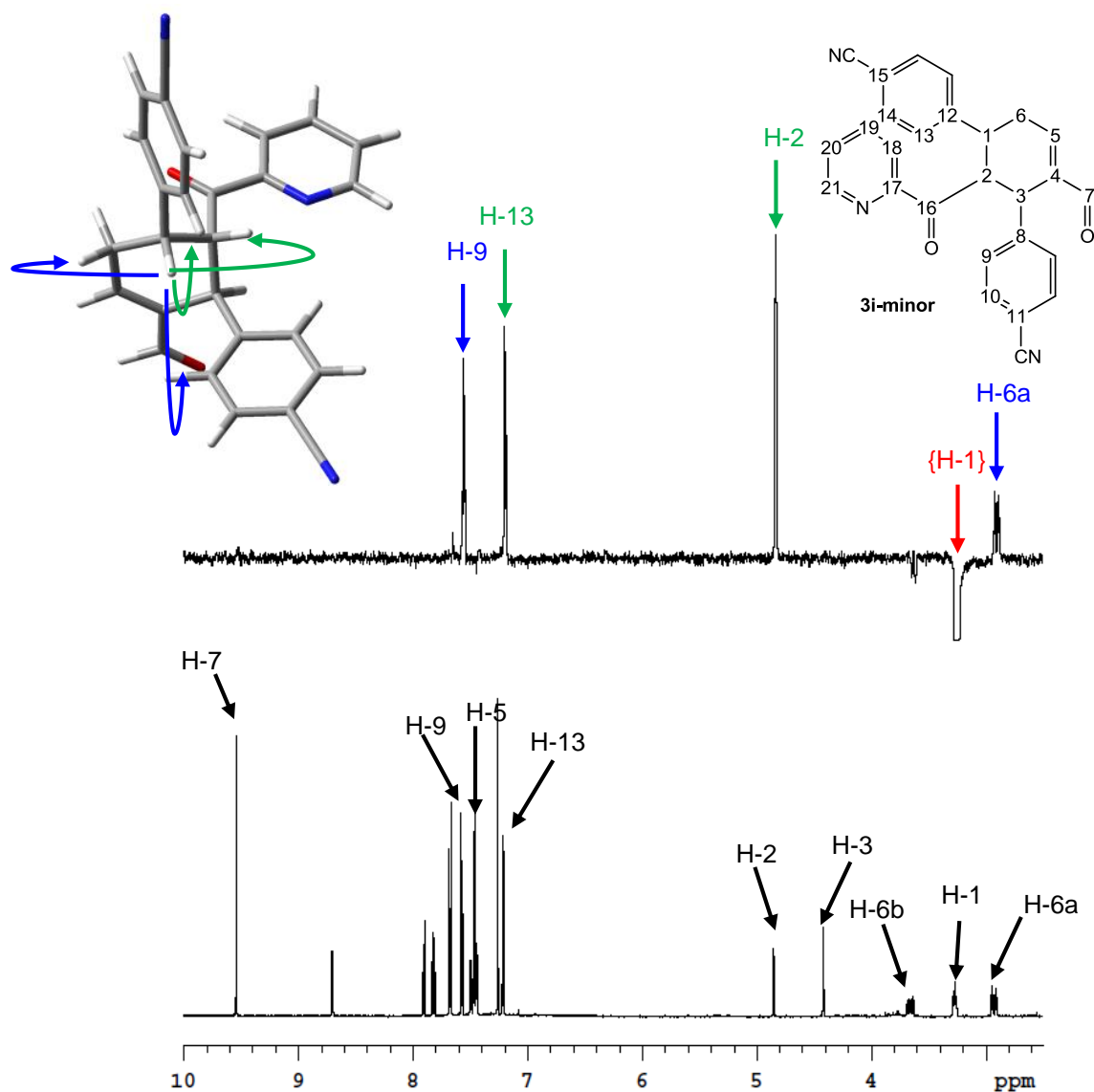


Figure 24. Top: Aliphatic area of NOE-NMR spectrum obtained from the irradiation of **H-1** (600 MHz in CDCl_3). Red: irradiated signals, green: control signals, blue: signals of interest. Bottom: ^1H -NMR spectrum.

Finally, in order to obtain information about the preferred conformation of the aldehydic group, a third experiment saturating aldehydic proton **H-7** at 9.55 ppm was carried out (**Figure 25**). The experiment showed large NOE effect on **H-5** (7.43 ppm), while a weak NOE effect on **H-3** was observed, which led to the conclusion that the proton **H-7** of the aldehydic group is localized mainly towards **H-5**.

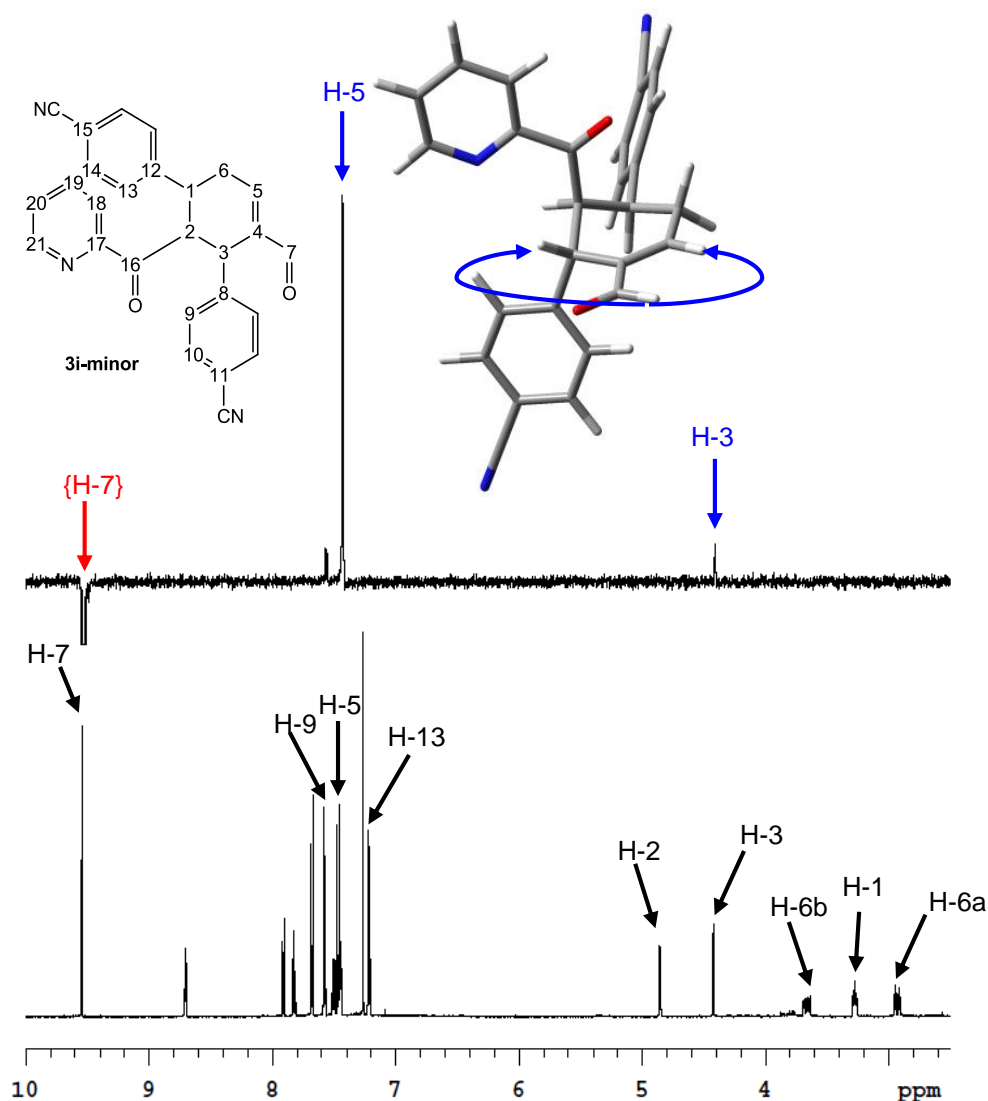


Figure 25. Top: NOE-NMR spectrum obtained from the irradiation of **H-7** (600 MHz in CDCl_3). Red: irradiated signals, blue: signals of interest. Bottom: ^1H -NMR spectrum.

With the information collected from the above-mentioned spectra, it was possible to assign the $1S^*, 2S^*, 3S^*$ relative configuration to the compound **3i-minor** (**Figure 26**). As conclusion, the relative configuration of minor product differed from the major product in the disposition of **H-2**, which in one case was positioned on the same side of **H-3** (major), and in the other case was in the *syn* position with **H-1** (minor).

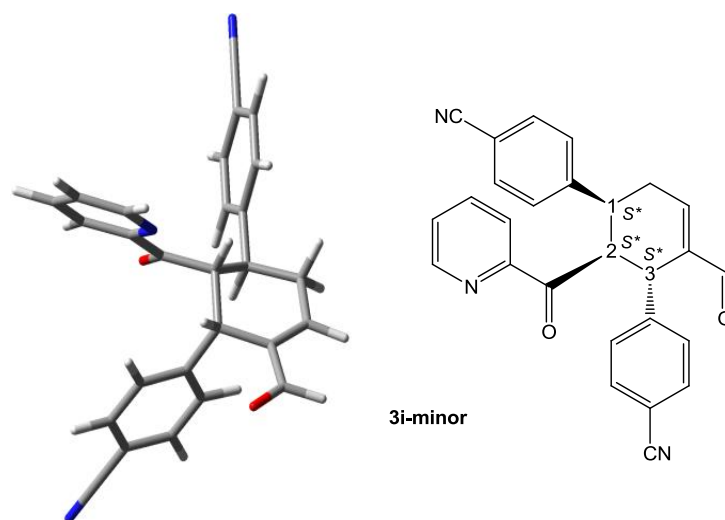


Figure 26. 3D structure (left) and relative configuration (right) of compound **3i-minor**.

Conformational analysis

Using the same procedure adopted for **3i-major** a conformational search was performed for **3i-minor**. The conformers with lowest energy were then optimized by DFT computations at the B3LYP/6-31G(d) level of theory. The 1*S*,2*S*,3*S* absolute configuration was assumed and six structures were minimized (**Figure 27**).

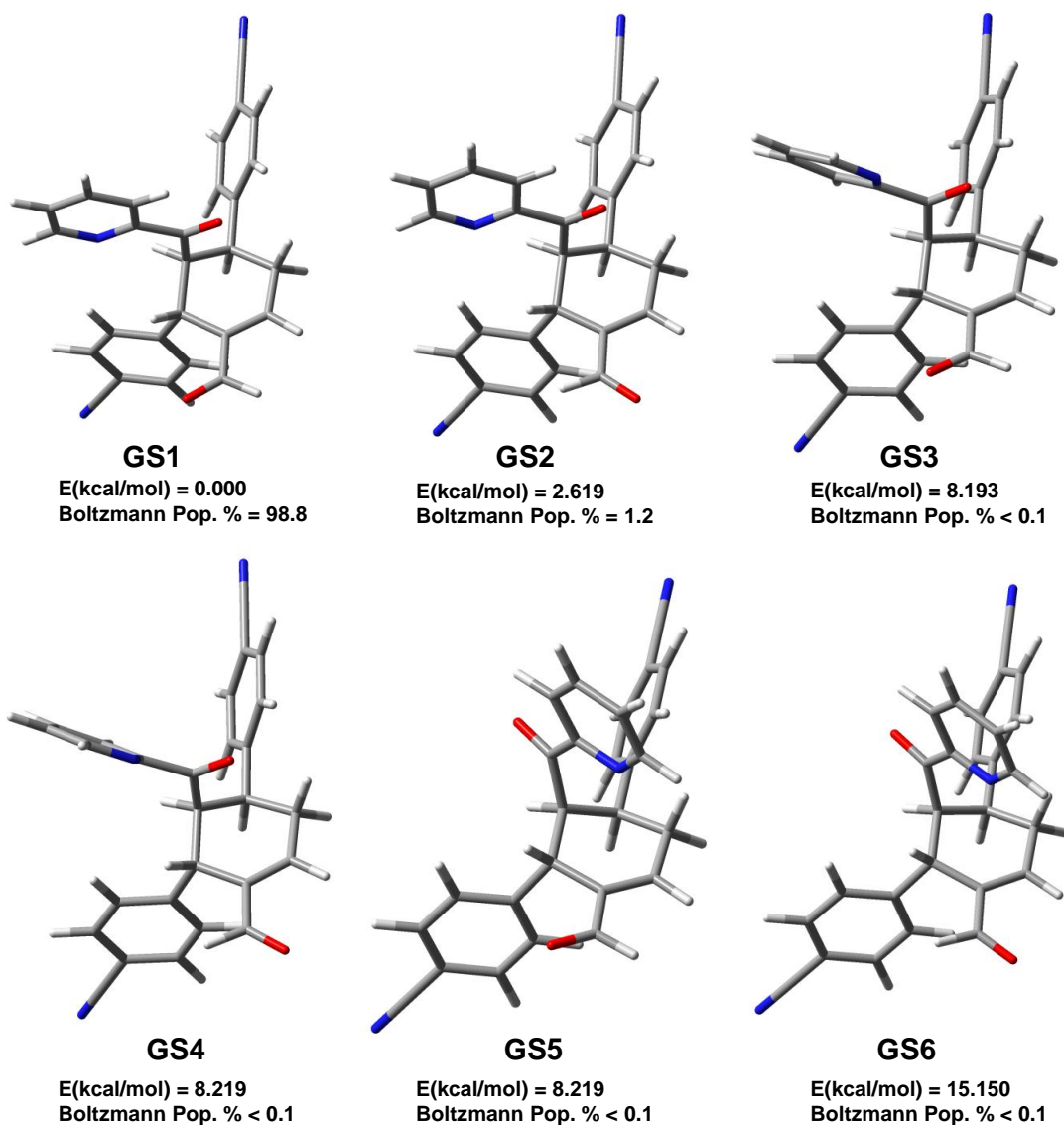


Figure 27. Conformations found by DFT calculations, optimized at the B3LYP/6-31G(d) level and relative energies of compound **3i-minor**.

Results from **Figure 27** showed that only conformation **GS1** and **GS2** were populated (Boltzmann population is higher than 0.5%). The two conformations derive from a 180° rotation of the aldehydic group, as for **3i-major** and the experimental NOE-NMR results well agreed with the lowest energy conformation **GS1**.

Absolute configuration

Once the relative configuration and DFT conformation of compound **3i-minor** were found, the absolute configuration was assigned by means of ECD technique. The spectrum acquired in the region between 180 nm and 400 nm was investigated and compared with the one of **3i-major** (**Figure 28**).

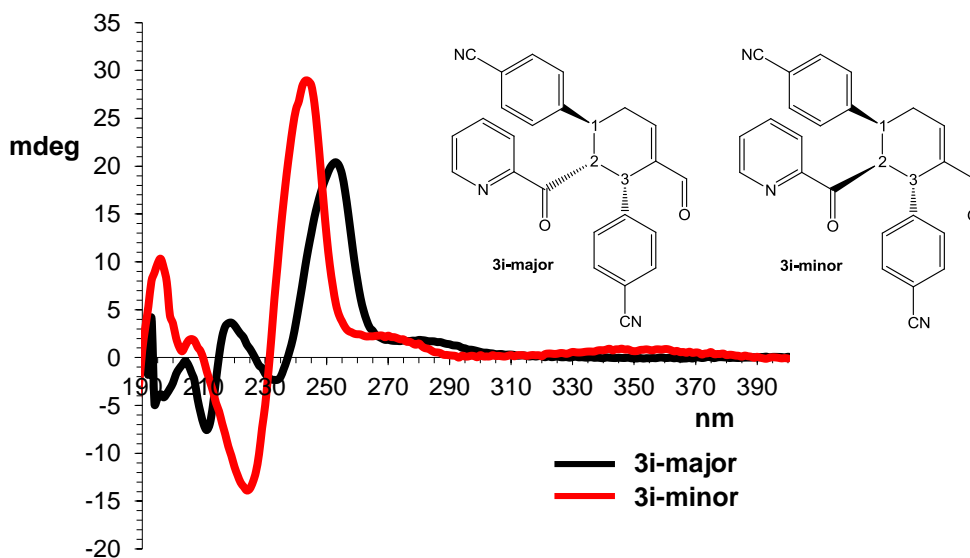


Figure 28. Comparison between the ECD experimental spectra of **3i-minor** (red) and **3i-major** (black). See details of ECD analysis in the **Section 6**.

The experimental spectrum of **3i-minor** showed a very broad band at 350 nm. The most intense region of the spectrum exhibited a positive signal at 240 nm and a negative one at 220 nm. As evidence from **Figure 28** the experimental spectrum confirmed that **3i-minor** was diastereoisomer with **3i-major**. Differently from **3i-major**, **3i-minor** did not show a negative branch at 215 nm.

Once the experimental spectrum was obtained, ECD simulations were performed using the functionals described in the **Paragraph 3.3.2** for **3i-major**. The TD-DFT simulations of the ECD spectra were carried out using the most stable geometries **GS1** and **GS2** and assuming the 1*S*,2*S*,3*S* absolute configuration (**Figure 29**).

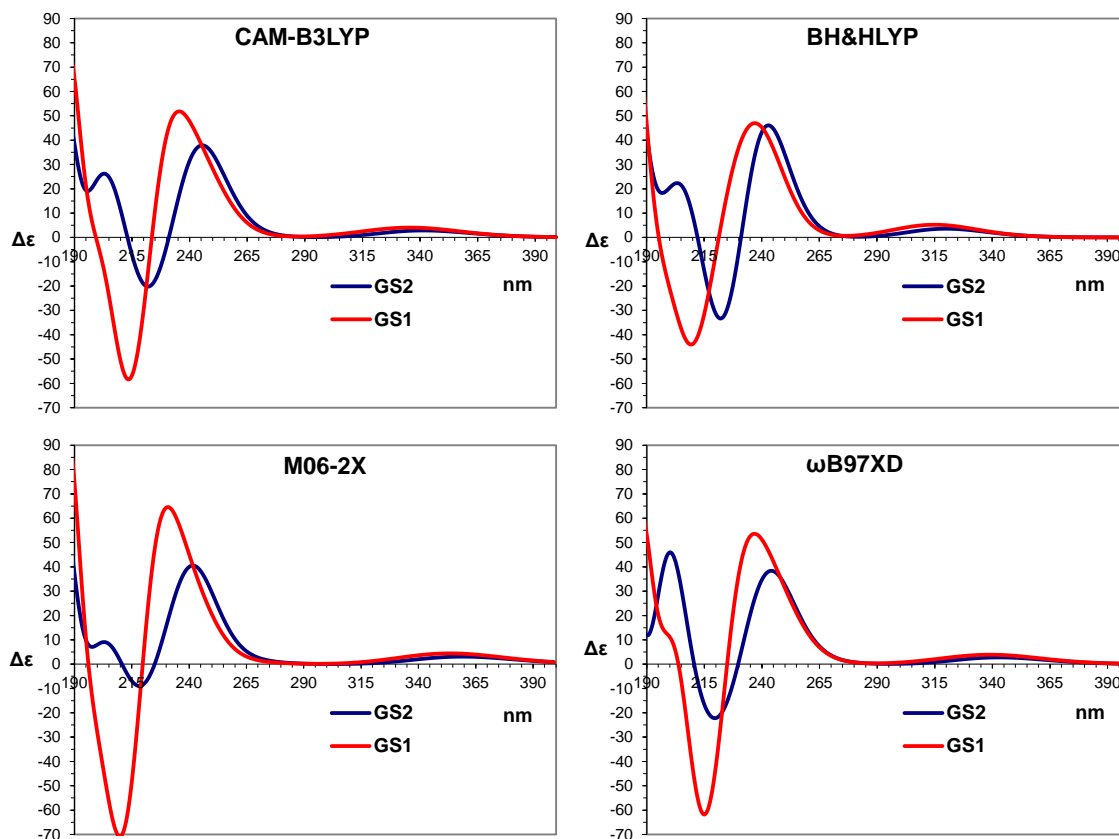


Figure 29. TD-DFT simulated spectra of the two conformations **GS1** and **GS2** of **3i-minor** performed using functionals CAM-B3LYP, BH&HLYP, M06-2X, ω B97XD and the 6-311++G(2d,p) basis set. The spectra were obtained using a 0.25 eV line width at half height.

All the simulated spectra showed a positive band around 240 nm and a negative signal at 215 nm, according with experimental results. Conformation **GS2** exhibited an extra “shoulder” band at 200 nm, while **GS1** presented a smooth spectrum in that area. Furthermore, **GS1** seemed to be shifted to the left compared with **GS2**. In conclusion, **GS1** showed more similarity with the experimental spectrum, leading to verify that it was the most populated conformation.

In order to obtain the averaged simulated spectrum to be compared with the experimental ECD, the spectra were weighted according with the populations determined by Boltzmann distribution based on the DFT calculations. The comparison between the experimental spectrum (black line) and the average simulated spectra obtained for each functional (coloured lines) is shown in **Figure 30**.

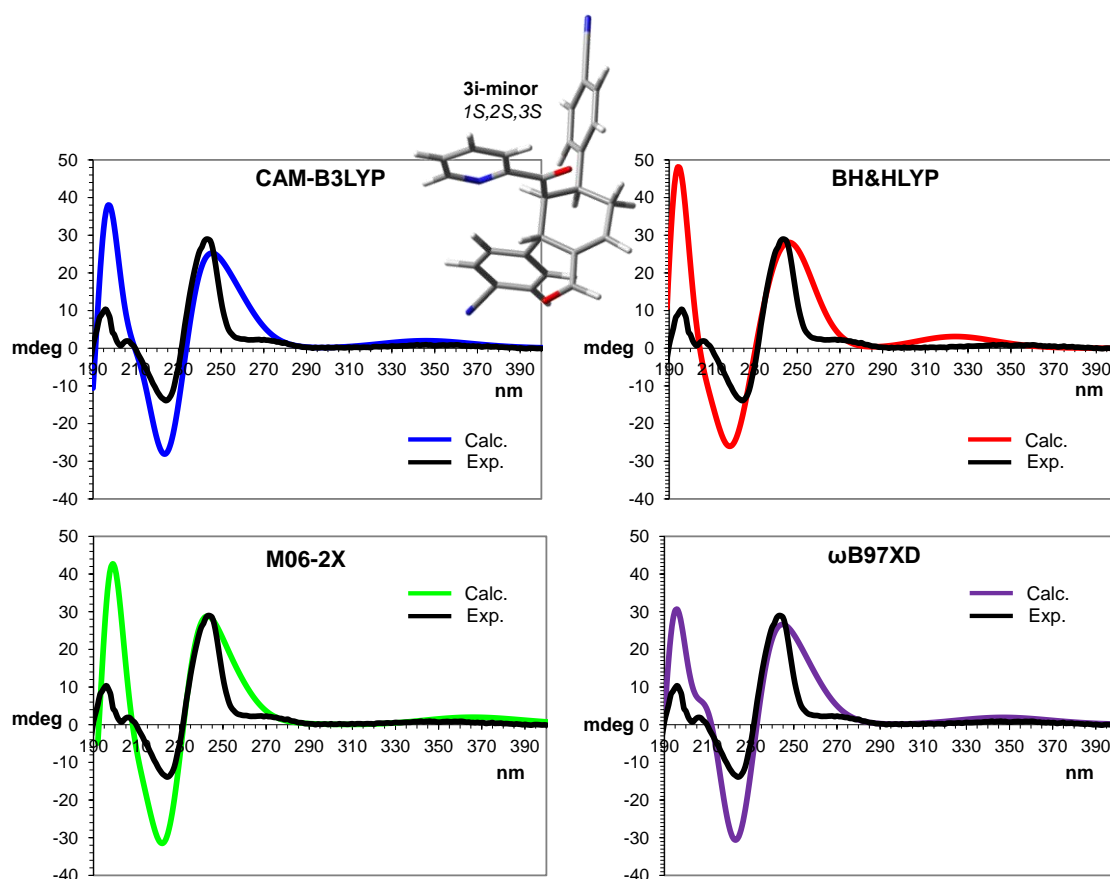


Figure 30. TD-DFT simulations compared with the experimental ECD spectrum of **3i-minor**. Black line: experimental spectrum. Coloured lines: simulated spectra. All the simulations were performed for 1S,2S,3S absolute configuration.

The simulated spectra were scaled and shifted in order to obtain the best overlap with experimental one (y axes scaling factors: 0.5, 0.6, 0.5, 0.45; x axes shift factors: 10, 9, 10, 12 nm for CAM-B3LYP, BH&HLYP, ω B97XD, M06-2X, respectively).

Comparing all the weighted simulated spectra with experimental one (**Figure 31**) the 1S,2S,3S absolute configuration was reliably assigned to **3i-minor**.

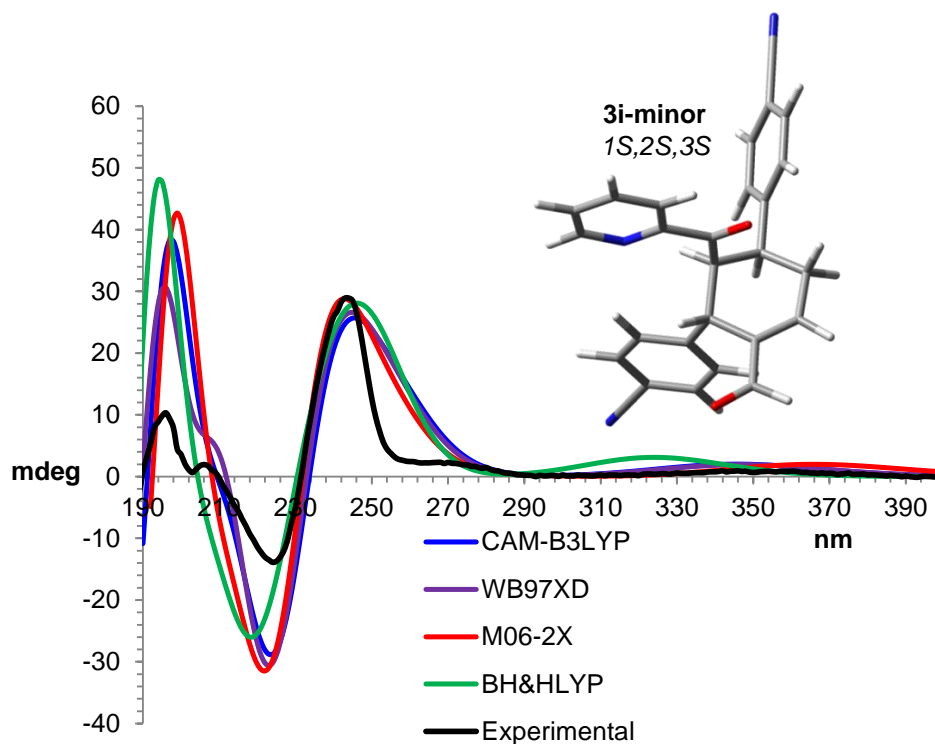


Figure 31. Comparison between the sum of all weighted simulated spectra and experimental spectrum for compound **3i-minor**.

3.3.4 Characterization of compound **3f-major**

Another approach for the determination of absolute configuration was employed in the case of compound **3f**. In fact, the absolute configuration of **3f-major** was determined by means of VCD techniques.

The IR and VCD region between 1350 cm^{-1} and 1850 cm^{-1} was investigated (**Figure 32**). The most intense region of IR spectrum showed a broad band centred at 1674 cm^{-1} , due to the stretching of the two C=O groups. In parallel, VCD spectrum presented a negative signal at 1792 cm^{-1} , which was attributed to the C=O stretching of the aldehydic group, and a positive signal at 1780 cm^{-1} , due to stretching C=O of the ketone moiety. The attribution was made on the base of the results of the DFT calculations.

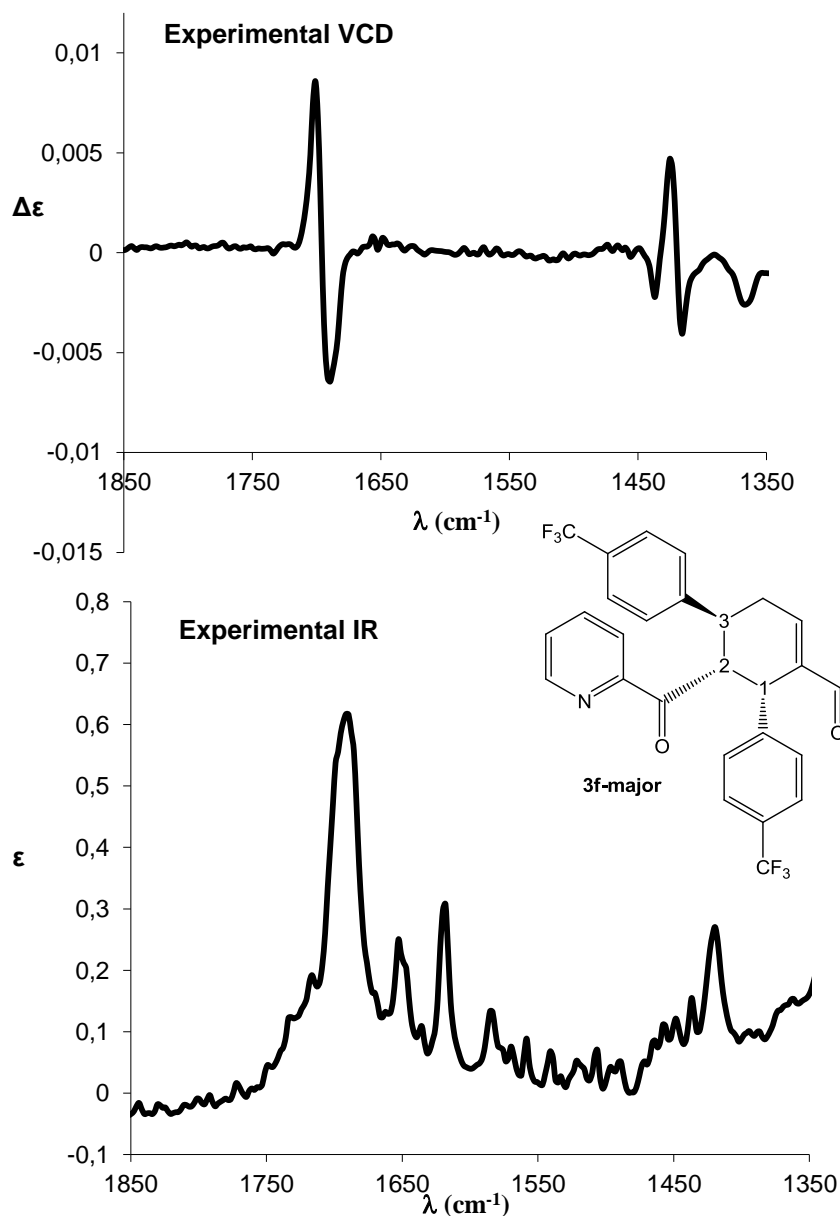


Figure 32. IR and VCD results for compound **3f-major**. Top: VCD experimental spectrum. Bottom: IR experimental spectrum. See details in **Section 6**.

Once the experimental spectrum was recorded, IR and VCD simulations were performed using DFT computations. In this case the same preliminary considerations about relative configuration and DFT conformations made for **3i-major** were used. Thus, it was possible to perform VCD calculations starting from the same absolute configuration (1*S*,2*R*,3*S*) and conformations (**GS3** and **GS4**) found for **3i-major**, substituting the cyano functional group with the CF₃ group as shown in **Figure 33**.

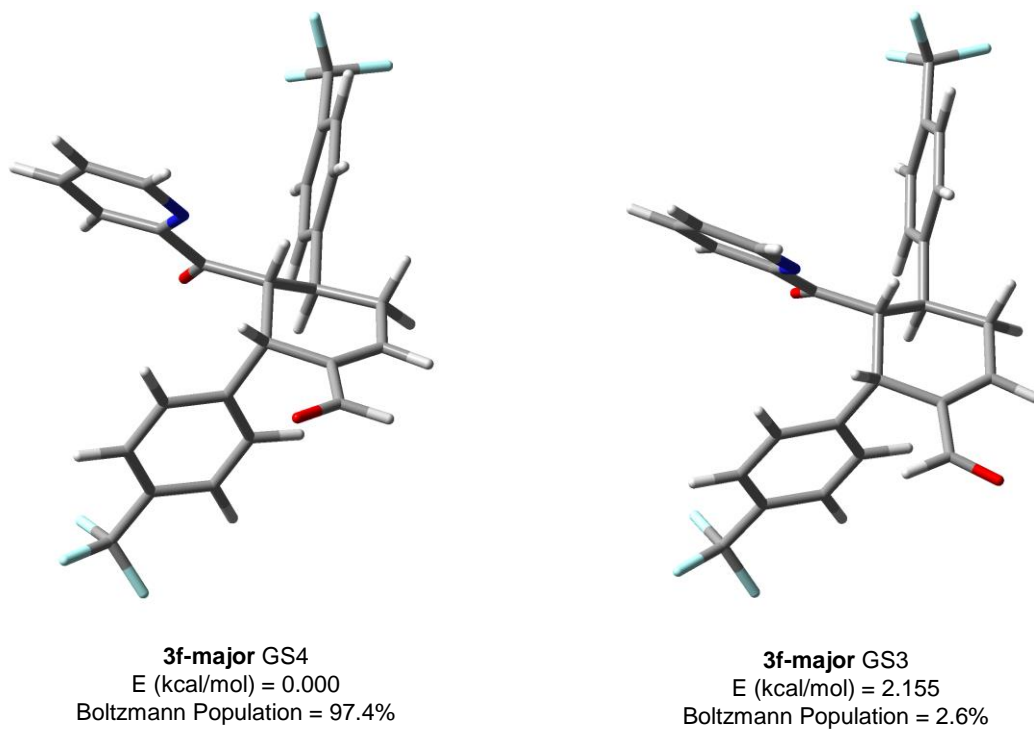


Figure 33. Most populated conformations of **3f-major**, using the absolute configuration 1*S*,2*R*,3*S*.

These structures were optimized by means of DFT calculations (B3LYP functional, 6-31G(d) basis set) and the simulated spectra were compared with experimental spectra as shown in **Figure 34**.

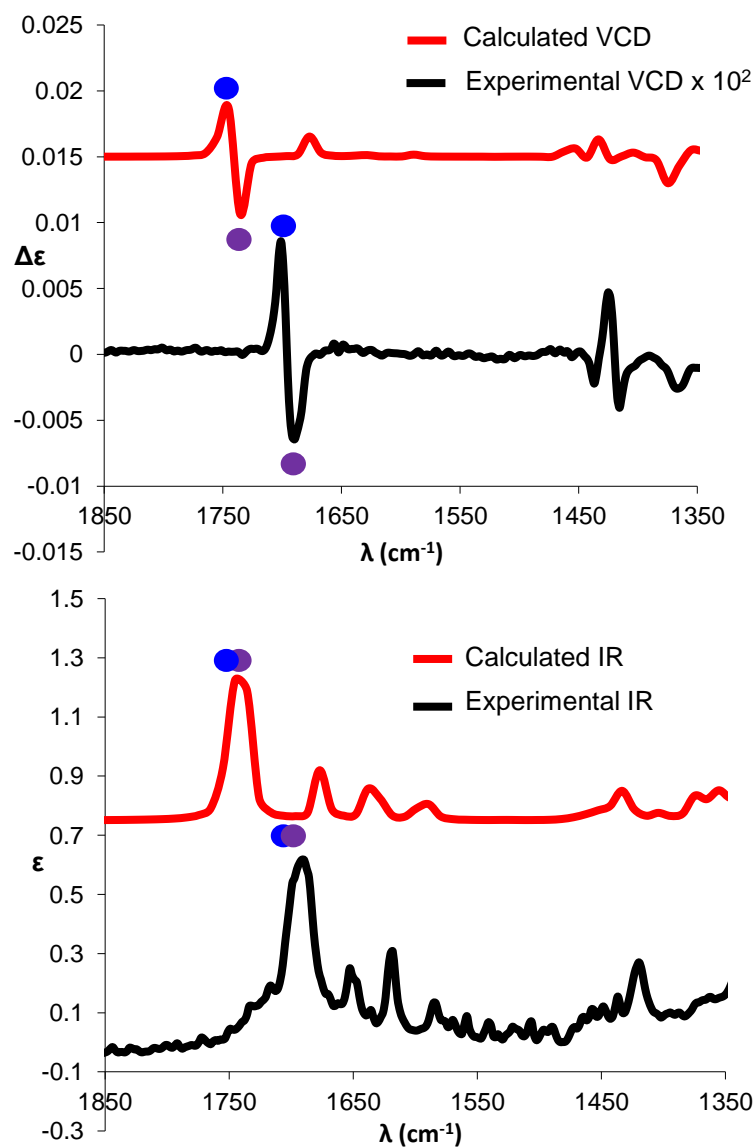


Figure 34. Comparison between simulated and experimental VCD spectra (top) and between simulated and experimental IR spectra (bottom).

The simulated spectra were scaled and shifted in order to obtain the best overlap with experimental one (for VCD spectrum: x axis scaling factor: 0.975, y axis shift factor: 0.015 $\Delta\epsilon$, y axis scaling factor: 0.00001; for IR spectrum: x axis scaling factor: 0.975, y axis shift factor: 0.75 $\Delta\epsilon$, y axis scaling factor: 0.00001). VCD simulations finally assigned the 1*S*,2*R*,3*S* absolute configuration to **3f-major**, according with results obtained by ECD spectroscopy.

3.3.5 Characterization of compound **3f-minor**

As well as for **3f-major** the IR and VCD region between 1550 cm^{-1} and 1850 cm^{-1} was observed for **3f-minor** (Figure 35).

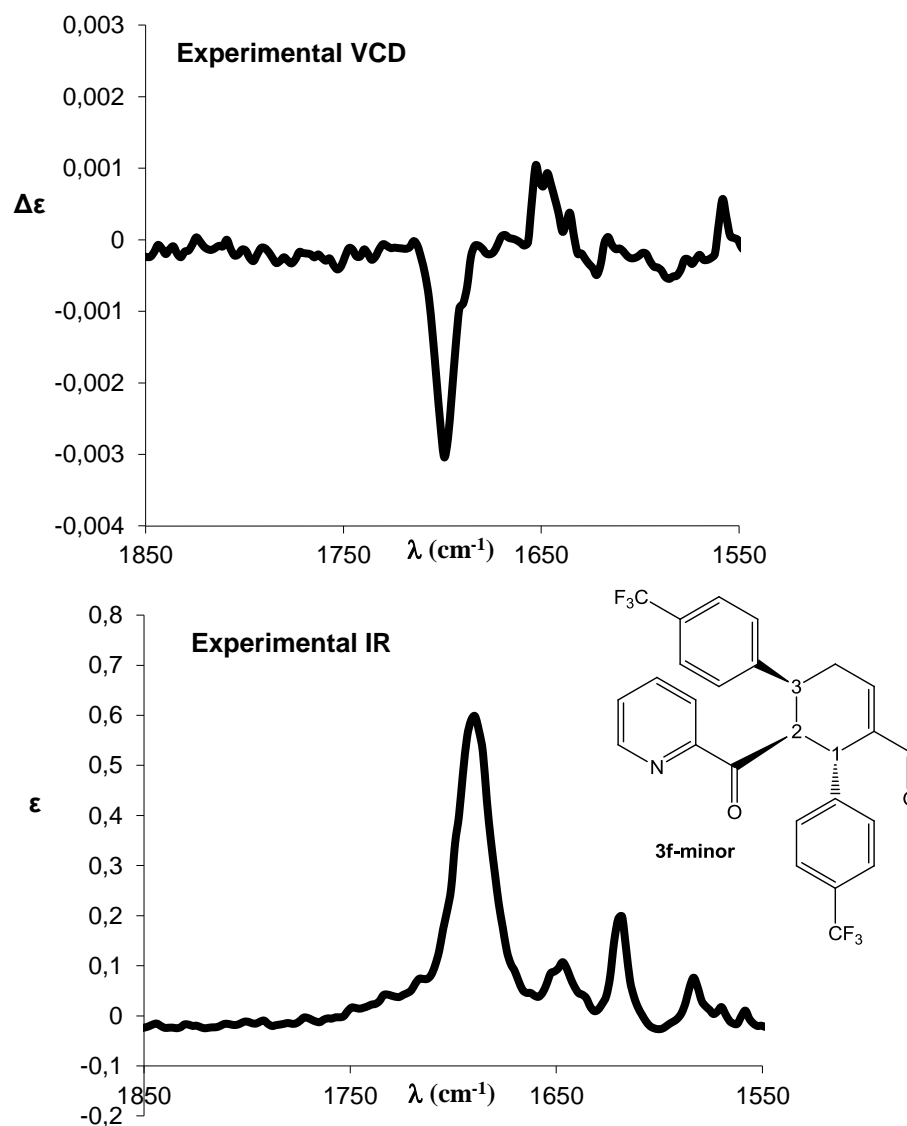


Figure 35. IR and VCD of compound **3f-minor**. Top: VCD experimental spectrum. Bottom: IR experimental spectrum.

The most intense IR signal was analysed, such as the band at about 1700 cm^{-1} . In parallel, VCD spectrum presented a signal at about the same wavelength (1700 cm^{-1}), corresponding to the stretching of the carbonyl group bonded to the pyridine group.

It was possible to perform VCD calculations starting from the same absolute configuration ($1S,2S,3S$) and conformations (**GS1** and **GS2**) found for **3i-minor**, substituting the cyano functional group with the CF_3 group, as shown in **Figure 36**.

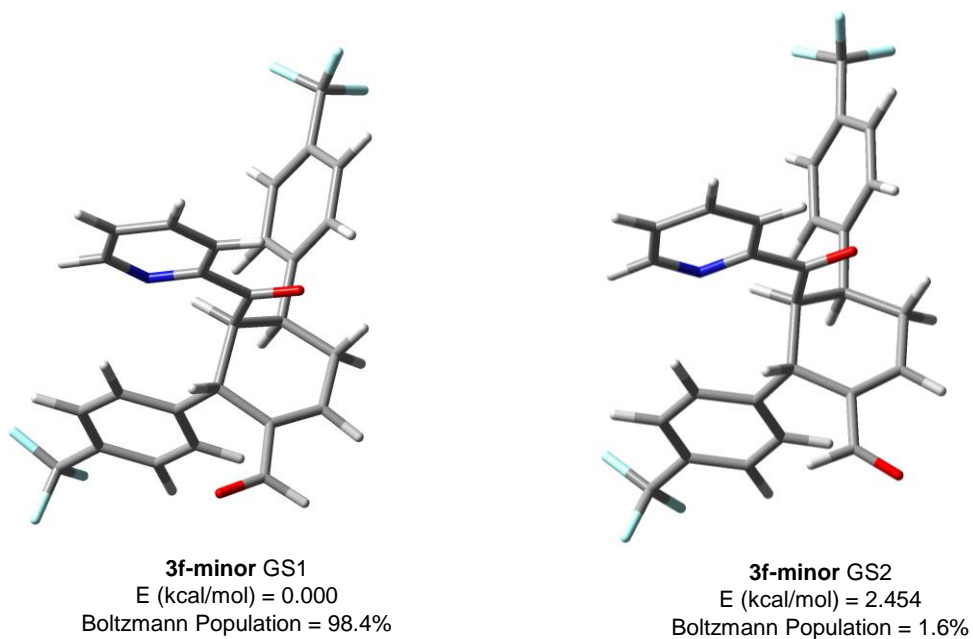


Figure 36. Most populated conformations of **3f-minor**, using the absolute configuration 1*S*,2*S*,3*S*.

These structures were optimized by means of DFT calculations (B3LYP functional, 6-31G(d) basis set) and the results were compared with experimental spectra as shown in **Figure 37**.

The simulated spectra were scaled and shifted in order to obtain the best overlap with experimental one (for IR spectrum: x axis scaling factor: 0.96, y axis shift factor: 0.75 $\Delta\epsilon$, y axis scaling factor: 0.001; for VCD spectrum: x axis scaling factor: 0.96, y axis shift factors: 0.008 $\Delta\epsilon$, y axis scaling factor: 0.00001).

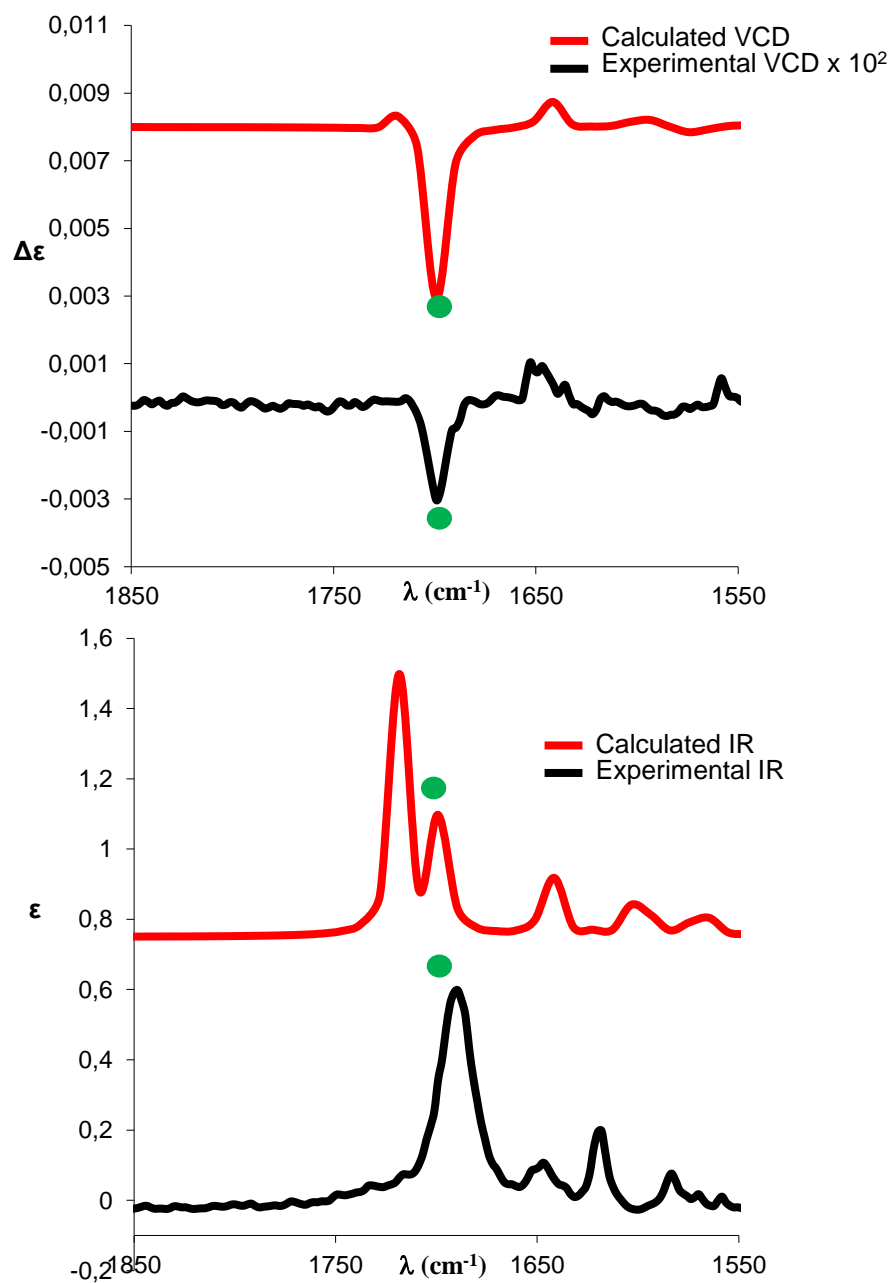


Figure 37. Comparison between simulated and experimental VCD spectra (top) and between simulated and experimental IR spectra (bottom).

As result, VCD simulations assigned the 1*S*,2*S*,3*S* absolute configuration to **3f-minor**. Thus, VCD configurations well agreed with ECD results and reinforced the hypothesis made for the absolute configuration of each diastereoisomer.

4 Conclusions

A enantioselective strategy for the synthesis of pyridine derivatives by means of synergistic catalysis was investigated. The obtainment of enantiopure compounds bearing three stereogenic centres (**3**) was achieved via highly enantioselective Michael-Michael-Aldol cascade reaction between 2-acetyl-pyridine (**1**) and α,β -unsaturated compounds (**2**). The mechanism involved a multicatalytic strategy, combining iminium catalysis and transition metal catalysis in a synergistic fashion. A reaction scope using different cinnamaldehydes (**2**) was performed in order to clarify the applicability and reproducibility of the reaction. As conclusion, the desired products were obtained with excellent enantioselectivities, good diastereoselectivities and moderate yields. The relative configurations of the products were determined by means of 2D-COSY and NOE-NMR experiments, while the absolute configurations were attributed by ECD and VCD spectroscopies supported by quantum mechanical calculations, which allowed verifying the stereochemistry of the reaction.

5 Experimental Part

5.1 General

Purifications: For the chromatography stationary phase Silica gel 60 F254 (Merck) for the TLC and silica gel 60 Å (230-400 mesh, Sigma Aldrich) were employed. To purify the products for the assignment of relative and absolute configuration HPLC Waters™ 600 instrument was used, with detection fixed at 254 nm. *Phenomenex Luna C18* (5 µm, 100 Å, 250 × 10 mm) was employed to purify **3i-major** fraction. The mobile phase consisted of an azeotropic mixture CH₃CN/H₂O (90:10), obtained by distillation (b.p. = 76-77 °C), and H₂O. *Lux Cellulose2* (5 µm, 250 × 10 mm) was used for **3i-minor** fraction, employing a mixture of *n*-hexane:*i*-PrOH as eluent.

NMR spectra: NMR spectra were recorded using a spectrometer operating at a field of 9.4 T (400 MHz for ¹H, 100.6 MHz for ¹³C) and a field of 14.4 T (600 MHz for ¹H, 150.8 MHz for ¹³C). Chemical shifts are given in ppm relative to the chloroform peak (7.26 ppm, 77.16 ppm) or relative to the internal standard tetramethylsilane (¹H and ¹³C). The assignment of the ¹³C signals was obtained by means of DEPT and J-MOD experiments. The protons assignments were possible by means of NOE-NMR and 2D-COSY experiments, the spectra of **3i-major** were obtained at 600 MHz in CD₃CN, while the ones of **3i-minor** were recorded at 600 MHz in CDCl₃.

ECD spectra: were recorded with a JASCO J-810 spectropolarimeter at +25 °C. Compounds were dissolved in acetonitrile using a concentration of about 10⁻⁴ M, in order to obtain a maximum absorbance of about 1 in the UV spectrum, and a 0.2 cm path length. Spectra were recorded in the 180-400 nm interval, and 16 scans were summed to register the final spectrum.

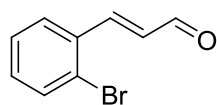
VCD spectra: were recorded with a ChiralIR-2X FT-VCD spectrometer (Biotools, Inc.) equipped with single PEM at 36kHz and 4 cm⁻¹ resolution, at +25 °C. Compounds were dissolved in CDCl₃ using a concentration of about 10⁻² M, in order to obtain a maximum absorbance of about 0.6 in the IR spectrum, and a 0.1 cm path length. Spectra were recorded in the 1000-2000 cm⁻¹ interval, and 12 blocks of 3120 scans, were summed to get the final spectrum.

5.2 Procedures and spectroscopic data of synthesized compounds.

Some of the cinnamaldehydes used for the reaction were bought commercially (**2a**, **2c**, **2d**, **2e**, **2m**, **2n**, **2o**), while few other were synthesized on site by Wittig reaction (**2b**, **2f**, **2g**, **2h**, **2i**, **2l**).⁽²⁸⁾

Synthesis of cinnamaldehydes (2b, 2g, 2l): A suspension of 20 mmol (1 eq) triphenylphosphoranylidene-acetaldehyde (**11**) and 40 mmol (2 eq) of benzaldehyde (**12**) in 5 mL of toluene was stirred at +40 °C up to 3 days. The reaction was monitored by TLC and ¹H-NMR. The mixture was separated by chromatography column using a *EtOAc:n-hexane* mixture in 1:15 ratio. The product (**2**) was obtained as a yellow solid and then characterized by ¹H-NMR spectroscopy.

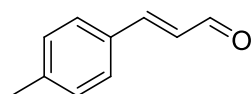
COMPOUND 2b: (E)-3-(2-bromophenyl)acrylaldehyde



¹H NMR (400 MHz, CDCl₃, TMS, +25 °C): δ 9.63 (d, *J* = 7.5 Hz, 1H), 7.73 (d, *J* = 15.5 Hz, 1H), 7.50 (d, *J* = 7.5 Hz, 1H), 7.27 (m, , 2H), 7.14 (td, *J* = 7.8, 1.5 Hz, 1H), 6.53 (dd, *J* = 15.5, 7.5 Hz, 1H).

Yield = 30%

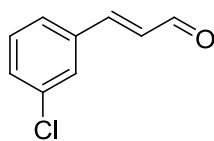
COMPOUND 2g: (E)-3-(p-tolyl)acrylaldehyde



¹H-NMR (400 MHz, CDCl₃, TMS, +25 °C): δ 9.52 (d, *J* = 7.7 Hz, 1H), 7.33 – 7.27 (m, 3H), 7.06 (d, *J* = 8.3 Hz, 2H), 6.52 (dd, *J* = 15.9, 7.7 Hz, 1H), 2.23 (s, 3H).

Yield = 34%

COMPOUND 2l: (E)-3-(3-chlorophenyl)acrylaldehyde

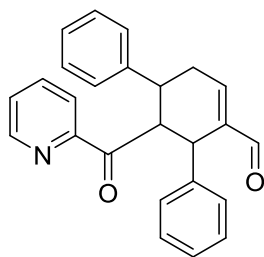


¹H NMR (400 MHz, CDCl₃, TMS, +25 °C): δ 9.57 (d, *J* = 7.6 Hz, 1H), 7.36 (m, 1H), 7.30 (ddd, *J* = 5.4, 3.6, 1.8 Hz, 1H) 7.28-7.20 (m, 3H), 6.52 (dd, *J* = 16.0, 7.6 Hz, 1H).

Yield = 63%

General procedure for the synthesis of compounds 3a-o: In a vial, the (*R*)-Jørgensen catalyst (**XXIX**) (13 mg, 20 mol%), the Zn(acac)₂ (2.5 mg, 5 mol%), 2-acetyl-pyridine (**1**) (24.2 mg, 0.2 mmol), cinnamaldehyde (**2**) (0.6 mmol) and the benzoic acid (12.2 mg, 20 mol%) were added. Then the mixture was dissolved in 3mL of CH₂Cl₂ and left to react under stirring up to 4 days. The reaction was monitored by TLC and ¹H-NMR. Crude was purified by chromatography column using different ratios of *n*-hexane:EtOAc between 2:1 and 6:1. The product (**3**) was obtained as a brown or red oil. Product was then characterized by ¹H-NMR and ¹³C-NMR, IR spectroscopies and HRMS.⁽²⁹⁾

COMPOUND 3-a: 2-2''-picolinoyl-1',2',3',6'-tetrahydro-[1,1':3',1''-terphenyl]-4'-carbaldehyde



Eluent mixture: *n*-hexane:EtOAc = 2:1

d.r. (major:minor) = 6:1

Major diastereoisomer

¹H-NMR (400 MHz, CDCl₃, 7.26 ppm, +25 °C): δ 9.49 (s, 1H), 8.75 (ddd, *J* = 4.8, 1.6, 0.9 Hz, 1H), 7.77 (ddd, *J* = 7.7, 7.7, 1.6 Hz, 1H), 7.63 (d, *J* = 7.5 Hz, 1H), 7.42 (d, *J* = 7.5 Hz, 2H), 7.24 – 7.05 (m, 8H), 6.80 – 6.72 (m, 2H), 5.08 (dd, *J* = 12.5, 5.4 Hz, 1H), 4.61 (dd, *J* = 5.4, 1.9 Hz, 1H), 3.61 (ddd, *J* = 12.5, 11.2, 6.1 Hz, 1H), 3.10 (ddd, *J* = 20.8, 6.1, 4.9 Hz, 1H), 2.63 (dddd, *J* = 20.8 Hz, 11.2 Hz, 2.4 Hz, 1.9 Hz, 1H).

¹³C-NMR (100.6 MHz, CDCl₃, 77.16 ppm, +25 °C): δ 199.77 (C=O), 192.33 (C=O), 153.45 (Cq), 150.16 (CH), 149.24 (CH), 144.73 (Cq), 142.38 (Cq), 138.87 (Cq), 137.22 (CH), 128.88 (CH), 128.61 (CH), 128.16 (CH), 127.53 (CH), 127.31 (CH), 127.28 (CH), 126.44 (CH), 122.47 (CH), 49.09 (CH), 41.13 (CH), 36.51 (CH₂), 36.34 (CH).

HRMS (ESI): m/z calc. for C₂₅H₂₂NO₂[M + H]⁺ = 368.1645 found: 368.1639.

HPLC (OZ-H column, Hexane:*i*PrOH = 90:10, flow rate = 1.0 mL/min, λ = 230 nm): t_R = 21.7 min (*S*), 27.8 min (*R*); 99% e.e. (*R*).

[α]_D²² = +3.0° (c = 1.0, CHCl₃)[(*R*) catalyst].

IR ν_{max} (KBr, cm⁻¹): 3025 (aromatic CH), 1685 (C=O), 2337 (C=N-C)

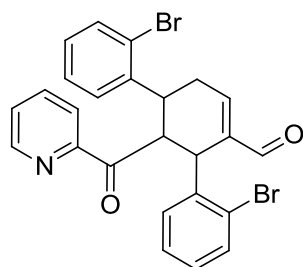
Yield = 40%

Minor diastereoisomer

¹H-NMR (400 MHz, CDCl₃, 7.26 ppm, +25 °C): δ 9.54 (s, 1H), 8.69 (ddd, *J* = 4.7, 1.7, 0.9 Hz, 1H), 7.92 – 7.87 (ddd, *J* = 8.1, 8.1, 1.3 Hz, 1H), 7.77 (td, *J* = 7.7, 1.7 Hz, 1H), 7.47 – 7.39 (m, 4H), 7.39 – 7.33 (m, 4H), 7.17 – 7.07 (m, 4H), 4.95 (dd, *J* = 3.6, 1.8 Hz, 1H), 4.36 (broad s, 1H), 3.65 (dddd, *J* = 20.3, 11.1, 2.9, 1.8 Hz, 1H), 3.35 (ddd, *J* = 11.1, 6.1, 3.6 Hz, 1H), 2.90 (ddd, *J* = 20.3, 6.1, 4.5 Hz, 1H).

¹³C-NMR (100.6 MHz, CDCl₃, 77.16 ppm, +25 °C): δ 200.01, 192.43, 153.65, 150.14, 149.22, 142.51, 141.77, 137.15, 136.75, 135.86, 129.32, 128.98, 128.17, 128.00, 127.84, 127.67, 122.30, 50.30, 40.13, 35.83, 30.10.

COMPOUND 3-b: 2,2''-dibromo-2'-picolinoyl-1',2',3',6'-tetrahydro-[1,1':3',1''-terphenyl]-4'-carbaldehyde



Eluent mixture (*n*-hexane:*EtOAc*) = 3:1

d.r. (major:minor) > 99%

Major diastereoisomer

¹H-NMR (400 MHz, CDCl₃, 7.26 ppm, +25 °C): δ 9.47 (s, 1H), 8.73 (ddd, *J* = 4.7, 1.4 Hz, 1.4 Hz, 1H), 7.73 – 7.69 (m, 2H), 7.45 (m, 2H), 7.40 (dd, *J* = 8.0, 1.1 Hz, 1H), 7.30 – 7.27 (m, 1H), 7.23 (dd, *J* = 7.8, 1.8 Hz, 1H), 7.17 (m, 2H), 7.06 (ddd, *J* = 9.8, 7.14, 2.3

Hz, 1H) 7.00 (ddd, $J = 7.6, 7.6, 1.2$ Hz, 1H), 6.91 (ddd, $J = 7.7, 7.7, 1.7$ Hz, 1H), 5.42 (dd, $J = 12.5, 5.1$ Hz, 1H), 5.09 (dd, $J = 5.1, 2.0$ Hz, 1H), 4.26 (ddd, $J = 12.5, 10.8, 6.0$ Hz, 1H), 3.18 (ddd, $J = 20.1, 6.0, 4.8$ Hz, 1H), 2.45 (dddd, $J = 20.1, 10.8, 2.7, 2.0$ Hz, 1H).

$^{13}\text{C-NMR}$ (100.6 MHz, CDCl_3 , 77.16 ppm, +25 °C): δ 199.78 (C=O), 191.79 (C=O), 153.53 (CH), 149.60 (Cq), 148.84 (CH), 143.06 (CH), 138.08 (CH), 136.98 (Cq), 133.16 (CH), 133.14 (CH), 130.26 (CH), 128.80 (Cq), 127.98 (Cq), 127.32 (CH), 126.98 (CH), 126.48 (CH), 122.52 (CH), 46.22 (CH), 39.79 (CH), 36.20 (CH_2), 34.54 (CH).

HRMS (ESI): m/z calc. for $\text{C}_{25}\text{H}_{19}\text{Br}_2\text{NO}_2[\text{M} + \text{H}]^+$: 523.9855, found = 523.9862.

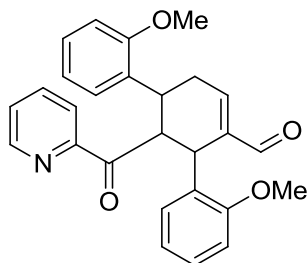
HPLC (Chiralpak OD-H column, *hexane/iPrOH* = 80:20, flow rate = 1.0 mL min $^{-1}$, λ = 230 nm): t_R = 37.0 min (*S*), 27.2 min (*R*); 99% e.e. (*R*).

$[\alpha]_D^{22} = +2.3^\circ$ ($c = 1.0$, CHCl_3)[*R*] catalyst].

IR ν_{max} (KBr, cm^{-1}): 2900 (aromatic CH), 1699 (C=O).

Yield = 28%

COMPOUND 3-c: 2,2''-dimethoxy-2'-picolinoyl-1',2',3',6'-tetrahydro-[1,1':3',1''-terphenyl]-4'-carbaldehyde



Eluent mixture (*n*-hexane:EtOAc) = 2:1

d.r. (major:minor) > 99%

Major diastereoisomer

$^1\text{H-NMR}$ (400 MHz, CDCl_3 , 7.26 ppm, +25 °C): δ 9.50 (s, 1H), 8.76 (ddd, 1H), 7.78 – 7.69 (m, 2H), 7.43 (ddd, $J = 16.1, 8.2, 5.7$ Hz, 1H), 7.22 – 7.13 (m, 2H), 7.06 – 6.97 (m, 3H), 6.89 (dt, $J = 6.6, 3.3$ Hz, 1H), 6.59 (m, 3H), 5.36 (dd, $J = 11.3, 4.6$ Hz, 1H), 5.02 (dd, $J = 4.6, 2.0$ Hz, 1H), 4.26 (ddd, $J = 11.3, 11.0, 6.0$ Hz, 1H), 3.90 (ddd, $J = 20.1, 6.0, 4.8$ Hz, 1H), 3.73 (dddd, $J = 20.1, 11.5, 2.7, 2.0$ Hz, 1H), 3.65 (s, 3H), 3.02 (s, 3H).

$^{13}\text{C-NMR}$ (100.6 MHz, CDCl_3 , 77.16 ppm, +25 °C): δ 199.24, 192.43, 157.39, 156.92, 154.14, 151.65, 148.92, 143.00, 136.43, 129.30, 128.29, 127.19, 127.03, 126.43, 121.19, 120.79, 119.95, 111.07, 109.91, 55.55, 55.50, 54.03, 46.37, 34.05, 29.83.

HRMS (ESI): m/z calc. for $C_{27}H_{25}NNaO_4 [M + Na]^+ = 450.1676$, found = 450.1676.

HPLC (OD-H column, *n*-hexane/*i*PrOH = 90:10, flow rate = 1.0 mL min⁻¹, $\lambda = 230$ nm):

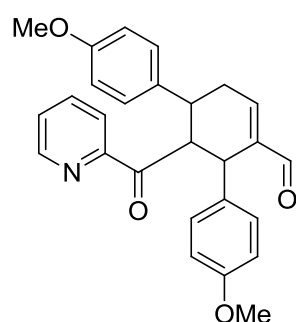
$t_R = 36.3$ min (*S*), 71.1 min (*R*); 99% e.e. (*R*).

$[\alpha]_D^{22} = +1.7^\circ$ ($c = 1.0$, CHCl₃)[(*R*) catalyst].

IR ν_{max} (KBr, cm⁻¹): 3008 (aromatic CH), 2841 (C-H methyl stretch), 1684 (C=O), 1490 (C-H methyl bend), 1246 (C-O).

Yield = 37%

COMPOUND 3-d: 4,4''-dimethoxy-2'-picolinoyl-1',2',3',6'-tetrahydro-[1,1':3',1''-terphenyl]-4'-carbaldehyde



Eluent mixture (*n*-hexane:EtOAc) = 2:1

d.r. (major:minor) = 4:1

Major diastereoisomer

¹H-NMR (400 MHz, CDCl₃, 7.26 ppm, +25 °C): δ 9.46 (s, 1H), 8.72 (ddd, $J = 4.8, 1.6, 0.9$ Hz, 1H), 7.76 (ddd, $J = 7.7, 7.7, 1.7$ Hz, 1H), 7.68 (dd, $J = 10.8, 2.9$ Hz, 1H), 7.48 (ddd, $J = 7.5, 4.7, 1.1$ Hz, 1H), 7.15 – 7.00 (m, 3H), 6.73 – 6.68 (m, 2H), 6.67 (s, 4H), 4.98 (dd, $J = 12.5, 5.2$ Hz, 1H), 4.59 (dd, $J = 5.2, 1.8$ Hz, 1H), 3.71 (s, 3H), 3.68 (s, 3H), 3.49 (ddd, $J = 12.5, 10.8, 6.1$ Hz, 1H), 2.98 (ddd, $J = 20.8, 6.1, 4.7$ Hz, 1H), 2.55 (dddd, $J = 20.8, 10.8, 2.9, 1.8$ Hz, 1H).

¹³C-NMR (100.6 MHz, CDCl₃, 77.16 ppm, +25 °C): δ 200.02 (C=O), 192.42 (C=O), 158.65 (Cq), 158.05 (Cq), 153.48 (Cq), 150.00 (CH), 149.23 (CH), 142.60 (Cq), 137.20 (CH), 136.81 (Cq), 130.95 (Cq), 129.84 (CH), 128.48 (CH), 127.24 (CH), 122.48 (CH), 113.99 (CH), 113.61 (CH), 55.23 (CH₃), 55.16 (CH₃), 49.44 (CH), 40.39 (CH₂), 36.60 (CH), 35.49 (CH).

HRMS (ESI): m/z calc. for $C_{27}H_{25}NNaO_4 [M + Na]^+ = 450.1676$, found = 450.1685.

HPLC (OD-H column, hexane/*i*PrOH = 90:10, flow rate = 1.0 mL min⁻¹, $\lambda = 230$ nm):

$t_R = 36.3$ min (*S*), 71.1 min (*R*); 99% e.e. (*R*).

$[\alpha]_D^{22} = +4.4^\circ$ ($c = 1.0$, CHCl₃)[(*R*) catalyst].

IR ν_{\max} (KBr, cm^{-1}): 2970 (aromatic CH), 2900 (C-H methyl stretch), 1689 (C=O), 1394 (C-H methyl bend), 1249 (C-O).

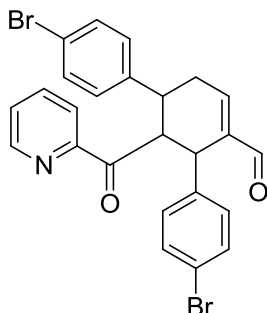
Yield = 30%

Minor diastereoisomer

$^1\text{H-NMR}$ (400 MHz, CDCl_3 , 7.26 ppm, +25 °C): δ 9.52 (s, 1H), 8.69 (d, $J = 4.6$ Hz, 1H), 7.89 (d, $J = 7.8$ Hz, 1H), 7.75 (ddd, $J = 7.8, 7.8, 1.1$ Hz, 1H), 7.39 (ddd, $J = 7.4, 4.6, 1.1$ Hz, 1H), 7.36 (m, 3H), 7.04 (d, $J = 8.7$ Hz, 2H), 6.89 (d, $J = 8.7$ Hz, 2H), 6.67 (d, $J = 9.4$ Hz, 2H), 4.86 (dd, $J = 3.5, 1.8$ Hz, 1H), 4.29 (broad s, 1H), 3.81 (s, 3H), 3.69 (s, 3H), 3.58 (dddd, $J = 20.3, 11.2, 2.9, 1.6$ Hz, 1H), 3.28 (ddd, $J = 11.2, 5.9, 3.6$ Hz, 1H), 2.85 (ddd, $J = 20.3, 5.9, 4.7$ Hz, 1H).

$^{13}\text{C-NMR}$ (100.6 MHz, CDCl_3 , 77.16 ppm, +25 °C): δ 202.04, 193.25, 158.49, 158.15, 153.68, 152.00, 149.05, 139.68, 137.05, 134.96, 134.42, 129.18, 128.88, 127.20, 122.47, 114.13, 113.73, 55.40, 55.26, 50.95, 39.60, 35.31, 29.85.

COMPOUND 3-e : 4,4''-dibromo-2'-picolinoyl-1',2',3',6'-tetrahydro-[1,1':3',1''-terphenyl]-4'-carbaldehyde



Eluent mixture (*n*-hexane:EtOAc) = 3:1

d.r. (major:minor) = 5:1

Major diastereoisomer

$^1\text{H-NMR}$ (400 MHz, CDCl_3 , 7.26 ppm, +25 °C): δ 9.48 (s, 1H), 8.74 (d, $J = 4.7$ Hz, 1H), 7.80 (ddd, $J = 7.7, 7.7, 1.7$ Hz, 1H), 7.68 (dt, $J = 7.7$ Hz, 1H), 7.51 (ddd, $J = 7.5, 4.8, 1.2$ Hz, 1H), 7.30 (m, 4H), 7.15 (m, 1H), 7.1 (d, $J = 8.4$ Hz, 2H), 6.63 (d, $J = 8.4$ Hz, 2H), 5.02 (dd, $J = 12.5, 5.4$ Hz, 1H), 4.63 (dd, $J = 5.4, 1.7$ Hz, 1H), 3.42 (ddd, $J = 12.5, 11.1, 5.9$ Hz, 1H), 3.01 (ddd, $J = 20.9, 5.9, 4.3$ Hz, 1H), 2.58 (dddd, $J = 20.9, 11.1, 2.8, 1.7$ Hz, 1H).

$^{13}\text{C-NMR}$ (100.6 MHz, CDCl_3 , 77.16 ppm, +25 °C): δ 199.64 (C=O), 192.05 (C=O), 153.08 (Cq), 149.94 (Cq), 149.37 (Cq), 143.44 (CH), 142.06 (CH), 137.91 (Cq), 137.43

(Cq), 131.79 (CH), 131.41 (CH), 130.47 (Cq), 129.27 (CH), 126.46 (CH), 122.51 (CH), 121.49 (CH), 120.33 (CH), 48.95 (CH), 40.59 (CH), 36.11 (CH), 35.94 (CH₂).

HRMS (ESI): m/z calc. for C₂₅H₂₀Br₂NO₂[M + H]⁺ = 523.9855, found = 523.9853.

HPLC (OD-H column, *hexane/iPrOH* = 90:10, flow rate = 1.0 mL min⁻¹, λ = 230 nm):
 t_R = 23.0 min (*S*), 35.4 min (*R*); 99% e.e. (*R*).

$[\alpha]_D^{22} = +2.4^\circ$ ($c = 1.0$, CHCl₃)[(*R*) catalyst].

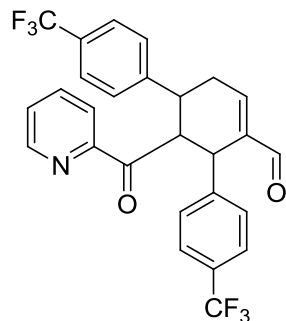
IR ν_{max} (KBr, cm⁻¹): 2971 (aromatic CH) 2880 (C-H stretch off C=O), 1684 (C=O).

Yield = 43%

Minor diastereoisomer

¹H NMR (400 MHz, CDCl₃, 7.26 ppm, +25 °C): δ 9.46 (s, 1H), 8.62 (ddd, $J = 4.8, 1.7, 1.0$ Hz, 1H), 7.83 (ddd, $J = 7.9, 1.0, 1.0$ Hz, 1H), 7.73 (ddd, $J = 7.7, 7.7, 1.7$ Hz, 1H), 7.44 – 7.37 (m, 4H), 7.36 – 7.30 (m, 1H), 7.29 – 7.20 (m, 3H), 6.96 – 6.87 (m, 2H), 4.75 (dd, $J = 3.9, 2.0$ Hz, 1H), 4.23 (broad s, 1H), 3.54 (dddd, $J = 20.7, 11.0, 2.8, 1.9$ Hz, 1H), 3.15 (ddd, $J = 11.0, 5.8, 3.9$ Hz, 1H), 2.82 (ddd, $J = 20.7, 5.8, 4.6$, 1H).

COMPOUND 3-f: 2'-picolinoyl-4,4''-bis(trifluoromethyl)-1',2',3',6'-tetrahydro-[1,1':3',1''-terphenyl]-4'-carbaldehyde



Eluent mixture (*n*-hexane:EtOAc) = 5:1

d.r. (major:minor) = 5:1

Major diastereoisomer

¹H-NMR (400 MHz, CDCl₃, 7.26 ppm, +25 °C): δ 9.50 (s, 1H), 8.77 (ddd, $J = 4.7, 1.6, 0.9$ Hz, 1H), 7.81 (ddd, $J = 7.7, 6.1, 1.7$ Hz, 1H), 7.67 (d, $J = 8.1$ Hz, 1H), 7.55 (ddd, $J = 7.7, 4.7, 1.3$ Hz, 1H), 7.45 (d, $J = 8.2$ Hz, 2H), 7.43 (d, $J = 8.2$ Hz, 2H), 7.35 (d, $J = 8.1$ Hz, 2H), 7.20 (m, 1H), 6.89 (d, $J = 8.1$ Hz, 2H), 5.14 (dd, $J = 12.5, 5.5$ Hz, 1H), 4.76 (dd, $J = 5.5, 1.8$ Hz, 1H), 3.60 (ddd, $J = 12.5, 11.1, 6.0$ Hz, 1H), 3.05 (ddd, $J = 20.8, 6.0, 4.9$ Hz, 1H), 2.60 (dddd, $J = 20.8, 11.1, 2.8, 1.8$ Hz, 1H).

¹³C-NMR (100.6 MHz, CDCl₃, 77.16 ppm, +25 °C): δ 199.51 (C=O), 191.93 (C=O), 152.96 (Cq), 149.99 (CH), 149.46 (CH), 148.41 (CH), 148.40 (CH), 142.90 (CH), 142.89 (CH), 141.90 (CH), 137.52 (CH), 129.17 (CH), 127.82 (CH), 127.79 (CH), 125.75 (Cq), 125.72 (Cq), 125.29 (Cq), 125.26 (Cq), 122.52 (Cq), 49.30 (CH), 41.29 (CH), 36.42 (CH₂), 30.25 (CH).

HRMS (ESI): m/z calc. for C₂₇H₂₀F₆NO₂[M + H]⁺ = 504.1393, found = 504.1398.

HPLC (OD-H column, *hexane/iPrOH* = 80:20, flow rate = 1.0 mL min⁻¹, λ = 230 nm):
t_R = 9.1 min (*S*), 16.5 min (*R*); 99% e.e. (*R*).

[α]_D²² = +3.2° (c = 1.0, CHCl₃)[(*R*) catalyst].

IR ν_{max} (KBr, cm⁻¹): 2980 (aromatic CH), 2888 (HC=O), 1699 (C=O).

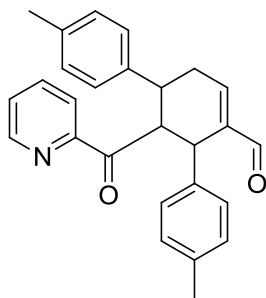
Yield = 55%

Minor diastereoisomer

¹H-NMR (400 MHz, CDCl₃, 7.26 ppm, +25 °C): δ 9.56 (s, 1H), 8.69 (ddd, *J* = 4.7, 1.6, 0.9 Hz, 1H), 7.91 (dt, *J* = 7.6 Hz, 1H), 7.81 (ddd, *J* = 7.7, 7.7, 1.7 Hz, 1H), 7.64 (d, *J* = 8.3 Hz, 2H), 7.58 (d, *J* = 8.5 Hz, 2H), 7.50 – 7.38 (m, 2H), 7.23 (d, *J* = 8.4 Hz, 2H), 7.15 (d, *J* = 8.0 Hz, 2H), 4.91 (dd, *J* = 3.6, 1.9 Hz, 1H), 4.42 (s, 1H), 3.60 (dddd, *J* = 20.3, 11.0, 2.8, 1.7 Hz, 1H), 3.25 (ddd, *J* = 11.0, 6.1, 3.6 Hz, 1H) 2.86 (ddd, *J* = 20.3, 6.1, 4.7 Hz 1H).

¹³C-NMR (100.6 MHz, CDCl₃, 77.16 ppm, +25 °C): δ 200.82, 192.73, 153.48, 152.47, 149.14, 146.71, 145.85, 138.98, 137.34, 129.56, 129.24, 128.52, 128.29, 127.67, 125.82, 125.80, 125.41, 125.20, 122.70, 50.26, 40.08, 36.12, 29.87.

COMPOUND 3-g: 4,4''-dimethyl-2'-picolinoyl-1',2',3',6'-tetrahydro-[1,1':3,1''-terphenyl]-4'-carbaldehyde



Eluent mixture (*n*-hexane:EtOAc) = 5:1

d.r. (major:minor) = 7:1

Major diastereoisomer

¹H-NMR (400 MHz, CDCl₃, 7.26 ppm, +25 °C): δ 9.47 (s, 1H), 8.74 (ddd, *J* = 4.7, 1.6, 0.9 Hz, 1H), 7.77 (ddd, *J* = 7.7, 7.7, 1.7 Hz, 1H), 7.68 (dt, *J* = 7.8, 1.1 Hz, 1H), 7.48 (ddd, *J* = 7.5, 4.7, 1.8 Hz, 1H), 7.12 (m, 3H), 6.96 (d, *J* = 7.9 Hz, 2H), 6.95 (d, *J* = 7.9 Hz, 2H), 6.64 (d, *J* = 8.0 Hz, 2H), 5.03 (dd, *J* = 12.5, 5.4 Hz, 1H), 4.61 (dd, *J* = 5.4, 1.8 Hz, 1H), 3.50 (ddd, *J* = 12.5, 11.1, 5.9 Hz, 1H), 3.00 (ddd, *J* = 20.8, 5.9, 4.7 Hz, 1H), 2.59 (dddd, *J* = 20.8, 11.1, 2.9, 1.8 Hz, 1H), 2.25 (s, 3H), 2.20 (s, 3H).

¹³C-NMR (100.6 MHz, CDCl₃, 77.16 ppm, +25 °C): δ 199.99 (C=O), 192.43 (C=O), 157.49 (Cq), 154.17 (Cq), 153.55 (Cq), 150.14 (CH), 149.22 (CH), 141.77 (Cq), 137.17 (CH), 136.71 (Cq), 135.86 (Cq), 129.32 (CH), 128.98 (CH), 128.73 (CH), 127.40 (CH), 127.23 (CH), 122.53 (CH), 49.21 (CH), 40.77 (CH), 36.64 (CH), 35.90 (CH₂), 21.24 (CH₃), 21.11 (CH₃).

HRMS (ESI): *m/z* calc. for C₂₇H₂₅NNaO₂[M + Na]⁺ = 418.1778, found = 418.1786.

HPLC (OD-H column, *hexane/iPrOH* = 90:10, flow rate = 1.0 mL min⁻¹, λ = 230 nm):
t_R = 13.0 min (*S*), 27.0 min (*R*); 99% e.e. (*R*).

[α]_D²² = +2.8° (*c* = 1.0, CHCl₃)[(*R*) catalyst].

IR ν_{max} (KBr, cm⁻¹): 3000 (aromatic CH), 2941 (C-H methyl stretch), 1684 (C=O), 1394 (C-H methyl bend), 1250 (C-O).

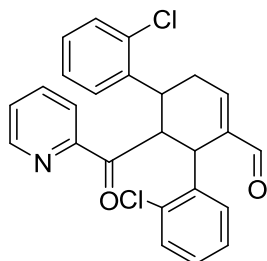
Yield = 10%

Minor diastereoisomer

¹H-NMR (400 MHz, CDCl₃, 7.2 ppm, +25 °C): δ 9.46 (s, 1H), 8.63 (ddd, *J* = 4.9, 1.4, 0.8 Hz, 1H), 7.83 (ddd, *J* = 7.8, 1.0, 1.0 Hz, 1H), 7.70 (ddd, *J* = 7.7, 7.7, 1.8 Hz, 1H), 7.61 – 7.54 (m, 1H), 7.51 – 7.45 (m, 1H), 7.40 – 7.33 (m, 1H), 7.33 – 7.28 (m, 1H), 7.16 – 7.12 (m, 2H), 6.99 – 6.83 (m, 4H), 4.84 (dd, *J* = 3.6, 1.8 Hz, 1H), 4.24 (broad s, 1H),

3.54 (dddd, $J = 20.1, 10.5, 3.1, 1.6$ Hz, 1H), 3.30 (ddd, $J = 10.5, 5.9, 3.6$ Hz, 1H), 2.81 (ddd, $J = 20.1, 5.9, 4.8$ Hz, 1H), 2.27 (s, 3H), 2.14 (s, 3H).

COMPOUND 3-h: 3,3''-dichloro-2'-picolinoyl-1',2',3',6'-tetrahydro-[1,1':3',1''-terphenyl]-4'-carbaldehyde



Eluent mixture (*n*-hexane:EtOAc) = 5:1

d.r. (major:minor) = 8:1

Major diastereoisomer

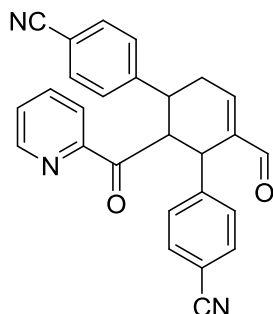
¹H-NMR (400 MHz, CDCl₃, 7.26 ppm, +25 °C): δ 9.47 (s, 1H), 8.75 (ddd, $J = 4.7, 1.4, 1.0$ Hz, 1H), 7.75 – 7.69 (m, 2H), 7.44 (ddd, $J = 5.3, 5.3, 3.4$ Hz, 1H), 7.27 (d, $J = 1.9$ Hz, 2H), 7.23 – 7.08 (m, 6H), 6.98 (dd, $J = 7.3, 1.8$ Hz, 1H), 5.42 (dd, $J = 12.6, 5.1$ Hz, 1H), 5.12 (dd, $J = 5.1, 2.0$ Hz, 1H), 4.25 (ddd, $J = 12.6, 11.3, 5.8$ Hz, 1H), 3.16 (ddd, $J = 20.8, 5.8, 4.8$ Hz, 1H), 2.49 (dddd, $J = 20.8, 11.3, 3.0, 2.0$ Hz, 1H).

¹³C NMR (100.6 MHz, CDCl₃, 77.16 ppm, +25 °C): δ 199.78 (C=O), 191.78 (C=O), 153.40 (CH), 149.93 (CH), 148.85 (CH), 142.85 (CH), 141.44 (Cq), 136.94 (Cq), 136.33 (CH), 135.26 (CH), 134.39 (CH), 130.06 (CH), 129.81 (Cq), 129.72 (Cq), 128.50 (Cq), 127.60 (Cq), 127.30 (CH), 127.26 (CH), 126.94 (CH), 126.38 (CH), 122.30 (CH), 46.18 (CH), 37.00 (CH), 33.36 (CH), 29.82 (CH₂).

$[\alpha]_D^{22} = +2.312^\circ$ ($c = 1.0$, CHCl₃)[*R*] catalyst].

Yield = 57%

COMPOUND 3-i: 6'-formyl-2'-picolinoyl-1',2',3',4'-tetrahydro-[1,1':3,1''-terphenyl]-4,4''-dicyanitrile



Eluent mixture (*n*-hexane:EtOAc) = 3:1 --> 1:1

d.r. (major:minor) = 4:1

Major diastereoisomer

¹H-NMR (400 MHz, CDCl₃, 7.26 ppm, +25 °C): δ 9.50 (s, 1H), 8.76 (ddd, *J* = 4.7, 1.7, 0.9 Hz, 1H), 7.82 (ddd, *J* = 7.7, 7.7, 1.7 Hz, 1H), 7.65 (dt, *J* = 7.8, 1.1 Hz, 1H), 7.55 (ddd, *J* = 7.7, 4.8, 1.6 Hz, 1H), 7.49 (d, *J* = 8.3 Hz, 2H), 7.45 (d, *J* = 8.3 Hz, 2H), 7.31 (d, *J* = 8.3 Hz, 2H), 7.22 (dd, *J* = 4.8, 1.9 Hz, 1H), 6.87 (d, *J* = 8.3 Hz, 2H), 5.12 (dd, *J* = 12.5, 5.6 Hz, 1H), 4.75 (dd, *J* = 5.6, 1.9 Hz, 1H), 3.53 (ddd, *J* = 12.5, 11.2, 6.0 Hz, 1H), 3.05 (ddd, *J* = 20.7, 6.0, 4.8 Hz, 1H), 2.60 (dddd, *J* = 20.7, 11.2, 2.9, 1.9 Hz, 1H).

¹³C-NMR (100.6 MHz, CDCl₃, 77.16 ppm, +25 °C): δ 199.44 (C=O), 191.72 (C=O), 152.69 (Cq), 149.87 (CH), 149.54 (CH), 144.32 (Cq), 141.49 (Cq), 137.65 (CH), 132.65 (CH), 132.11 (CH), 129.54 (CH), 128.84 (CH), 128.94 (CH), 128.03 (CH), 122.47 (CH), 118.77 (CH), 118.03 (Cq), 111.49 (Cq), 110.76 (Cq), 48.86 (CH), 41.13 (CH), 36.76 (CH₂), 35.61 (CH).

HRMS (ESI): *m/z* calc. for C₂₇H₂₀N₃O₂[M + H]⁺ = 418.1550, found = 418.1556

HPLC (OD-H column, hexane/*i*PrOH = 80:20, flow rate = 1.0 mL min⁻¹, λ = 230 nm):
t_R = 45.0 min (*S*), 61.6 min (*R*); 99% e.e. (*R*).

[α]_D²² = +3.2° (c = 1.0, CHCl₃)[(*R*) catalyst].

IR ν_{max} (KBr, cm⁻¹): 2980 (aromatic CH), 2882 (HC=O), 2288 (C≡N-C), 1699 (C=O).

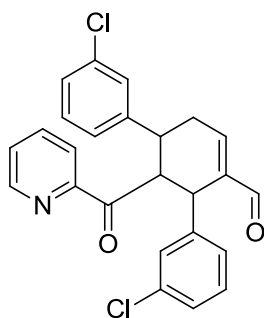
Yield = 40%

Minor diastereoisomer

¹H-NMR (600 MHz, CDCl₃, TMS, +25 °C): δ 9.55 (s, 1H), 8.71 (ddd, *J* = 4.7, 1.7, 0.9 Hz, 1H), 7.9 (dt, *J* = 7.6, 1.2 Hz, 1H), 7.82 (ddd, *J* = 7.6, 7.6, 1.8 Hz, 1H), 7.68 (d, *J* = 8.3 Hz, 2H), 7.58 (d, *J* = 8.3 Hz, 2H), 7.50 (ddd, *J* = 7.6, 4.7, 1.2 Hz, 1H), 7.47 (d, *J* = 8.3 Hz, 2H), 7.44 (ddd, *J* = 3.6, 1.2 Hz, 1H), 7.22 (d, *J* = 8.3 Hz, 2H), 4.85 (dd, *J* = 3.6, 2.3 Hz, 1H), 4.42 (broad s, 1H), 3.65 (dddd, *J* = 20.0, 10.5, 2.8, 1.2 Hz, 1H), 3.28 (ddd, *J* = 10.5, 6.1, 3.6 Hz, 1H), 2.93 (ddd, *J* = 20.0, 6.1, 4.0, 1H).

¹³C-NMR (150.8 MHz, CDCl₃, 77 ppm, +25 °C): δ 200.13, 192.36, 153.18, 149.54, 147.90, 146.93, 138.51, 137.36, 132.18, 128.84, 128.62, 127.79, 127.76, 122.67, 118.76, 118.60, 116.34, 111.06, 110.75, 50.08, 40.07, 36.33, 29.45.

COMPOUND 3-1: 3,3''-dichloro-2'-picolinoyl-1',2',3',6'-tetrahydro-[1,1':3',1''-terphenyl]-4'-carbaldehyde



Eluent mixture (*n*-hexane:EtOAc) = 3:1

d.r. (major:minor) = 5:1

Major diastereoisomer

¹H-NMR (400 MHz, CDCl₃, 7.26 ppm, +25 °C): δ 9.49 (s, 1H), 8.75 (ddd, *J* = 4.8, 1.6, 0.9 Hz, 1H), 7.81 (ddd, *J* = 7.7, 7.7, 1.7 Hz, 1H), 7.69 (dt, *J* = 7.9, 1.0 Hz, 1H), 7.52 (ddd, *J* = 7.5, 4.8, 1.3 Hz, 1H), 7.19 – 7.05 (m, 7H), 6.71 (t, *J* = 1.8 Hz, 1H), 6.61 (dt, *J* = 7.6 Hz, 1H), 5.04 (dd, *J* = 12.5, 5.4 Hz, 1H), 4.64 (dd, *J* = 5.4, 1.9 Hz, 1H), 3.47 (ddd, *J* = 12.5, 11.0, 6.1 Hz, 1H), 3.01 (ddd, *J* = 20.7, 6.1, 5.1 Hz, 1H), 2.59 (dd, *J* = 20.7, 11.0, 2.9, 1.9 Hz, 1H).

¹³C-NMR (100.6 MHz, CDCl₃, 77.16 ppm, +25 °C): δ 199.56 (C=O), 192.01 (C=O), 153.15 (CH), 150.10 (CH), 149.38 (CH), 146.50 (CH), 141.76 (Cq), 140.86 (Cq), 137.43 (CH), 134.15 (Cq), 134.42 (Cq), 129.95 (CH), 129.43 (CH), 128.83 (Cq), 127.89 (Cq), 127.65 (CH), 127.63 (CH), 127.11 (CH), 126.84 (CH), 125.57 (CH), 122.51 (CH), 48.87 (CH), 40.70 (CH), 36.20 (CH₂), 36.12 (CH).

HRMS (ESI): *m/z* calc. for C₂₅H₁₉Cl₂NNaO₄[M + Na]⁺ = 458.0685, found = 458.0686.

$[\alpha]_D^{22} = +2.8^\circ$ ($c = 1.0$, CHCl_3)[(R) catalyst].

IR ν_{max} (KBr, cm^{-1}): 2980 (aromatic CH), 2900 (HC=O), 1684 (C=O).

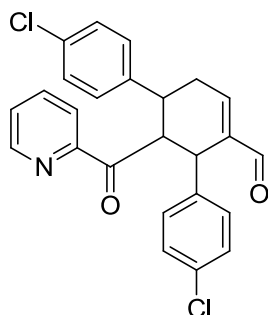
Yield = 42%

Minor diastereoisomer

$^1\text{H-NMR}$ (400 MHz, CDCl_3 , 7.26 ppm, +25 °C): δ 9.54 (s, 1H), 8.71 (ddd, $J = 4.7, 1.6, 0.9$ Hz, 1H), 7.91 (d, $J = 7.8$ Hz, 1H), 7.80 (ddd, $J = 7.7, 7.7, 1.7$ Hz, 1H), 7.46 (m, 2H), 7.43 – 7.39 (m, 2H), 7.36 (d, $J = 7.3$ Hz, 2H), 7.31 (d, $J = 6.6$ Hz, 2H), 7.01 (d, $J = 6.6$ Hz, 2H), 4.87 (dd, $J = 3.6, 1.6$ Hz, 1H), 4.35 (broad s, 1H), 3.61 (dddd, $J = 20.2, 11.6, 2.9, 1.6$ Hz, 1H), 3.24 (ddd, $J = 11.6, 6.2, 3.6$ Hz, 1H), 2.87 (ddd, $J = 20.2, 6.2, 5.8$ Hz, 1H).

$^{13}\text{C-NMR}$ (100.6 MHz, CDCl_3 , 77.16 ppm, +25 °C): δ 201.06, 192.82, 153.63, 152.62, 149.13, 144.75, 144.02, 138.74, 137.09, 134.44, 134.13, 130.15, 129.88, 129.53, 128.17, 128.07, 127.58, 127.38, 126.78, 126.31, 122.46, 50.17, 39.84, 35.70, 29.76.

COMPOUND 3-m: 4,4''-dichloro-2'-picolinoyl-1',2',3',6'-tetrahydro-[1,1':3',1''-terphenyl]-4'-carbaldehyde



Eluent mixture (n -hexane:EtOAc) = 3:1

d.r. (major:minor) = 5:1

Major diastereoisomer

$^1\text{H-NMR}$ (400 MHz, CDCl_3 , 7.26 ppm, +25 °C): δ 9.48 (s, 1H), 8.74 (ddd, $J = 4.8, 1.6, 0.9$ Hz, 1H), 7.80 (ddd, $J = 9.4, 6.7, 2.9$ Hz, 1H), 7.68 (dt, $J = 6.8$ Hz, 1H), 7.50 (ddd, $J = 10.1, 5.0, 3.8$ Hz, 1H), 7.17 (m, 5H), 7.13 (d, $J = 7.6$ Hz, 2H), 6.69 (d, $J = 7.6$ Hz, 2H), 5.02 (dd, $J = 12.5, 5.4$ Hz, 1H), 4.64 (dd, $J = 5.4, 1.8$ Hz, 1H), 3.49 (ddd, $J = 12.5, 11.0, 6.1$ Hz, 1H), 3.01 (ddd, $J = 20.9, 6.1, 5.0$ Hz, 1H), 2.58 (dddd, $J = 20.9, 11.0, 2.5, 1.8$ Hz, 1H).

$^{13}\text{C-NMR}$ (100.6 MHz, CDCl_3 , 77.16 ppm, +25 °C): δ 199.67 (C=O), 192.07 (C=O), 153.11 (Cq), 149.95 (CH), 149.36 (CH), 142.91 (CH), 142.12 (Cq), 137.41 (Cq), 137.39

(Cq), 133.25 (Cq), 132.23 (Cq), 130.10 (CH), 129.07 (CH), 128.88 (CH), 128.48 (CH), 127.60 (CH), 122.48 (CH), 49.06 (CH), 40.53 (CH), 36.17 (CH₂), 35.86 (CH).

HRMS (ESI): m/z calc. for C₂₅H₂₁NO₂ [M+H]⁺: 436.0871, found = 436.0886.

HPLC (OZ-H column, *hexane/iPrOH* = 90:10, flow rate = 1.0 mL min⁻¹, λ = 230 nm): t_R = 18.6 min (*S*), 27.7 min (*R*); 99% e.e. (*R*).

[α]_D²² = +2.5° (c = 1.0, CHCl₃)[(*R*) catalyst].

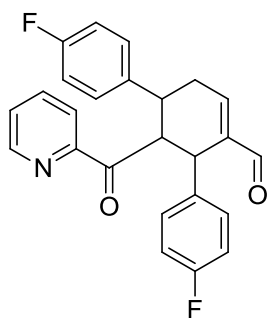
Yield = 56%

Minor diastereoisomer

¹H-NMR (400 MHz, CDCl₃, 7.26 ppm, +25 °C): δ 9.53 (s, 1H), 8.69 (ddd, *J* = 4.7, 1.6, 0.9 Hz, 1H), 7.84 (ddd, *J* = 7.9, 7.9, 1.0 Hz, 1H), 7.73 (ddd, *J* = 7.7, 7.7, 1.6 Hz, 1H), 7.40 (ddd, *J* = 7.7, 4.8, 1.4 Hz, 1H), 7.34 – 7.27 (m, 5H), 7.08 – 7.04 (m, 2H), 7.01 – 6.96 (m, 2H), 4.83 (dd, *J* = 3.6, 1.9 Hz, 1H), 4.32 (broad s, 1H), 3.60 (dddd, *J* = 20.4, 11.1, 2.8, 1.4 Hz, 1H), 3.24 (ddd, *J* = 11.1, 6.1, 3.6 Hz, 1H), 2.86 (ddd, *J* = 20.4, 6.1, 4.8 Hz, 1H).

¹³C-NMR (100.6 MHz, CDCl₃, 77.16 ppm, +25 °C): δ 201.06, 192.74, 153.42, 152.48, 148.97, 141.11, 140.30, 139.06, 137.10, 132.72, 132.31, 129.39, 129.17, 128.77, 128.40, 127.37, 122.45, 50.47, 39.54, 35.48, 29.94.

COMPOUND 3-n: 4,4''-difluoro-2'-picolinoyl-1',2',3',6'-tetrahydro-[1,1':3',1''-terphenyl]-4'-carbaldehyde



Eluent mixture (*n-hexane:EtOAc*) = 3:1

d.r. (major:minor) = 5:1

Major diastereoisomer

¹H-NMR (400 MHz, CDCl₃, 7.26 ppm, +25 °C): δ 9.48 (s, 1H), 8.74 (ddd, *J* = 4.7, 1.0, 0.7 Hz, 1H), 7.79 (ddd, *J* = 7.7, 7.7, 1.7 Hz, 1H), 7.67 (d, *J* = 7.8 Hz, 1H), 7.54 – 7.45 (ddd, *J* = 7.6, 4.7, 1.3 Hz, 1H), 7.21 – 7.12 (m, 3H), 6.88 (d, *J* = 6.8 Hz, 2H), 6.83 (d, *J* = 6.8 Hz, 2H), 6.75 – 6.70 (m, 2H), 4.95 (dd, *J* = 12.5, 5.7 Hz, 1H), 4.65 (dd, *J* = 5.7, 1.9

Hz, 1H), 3.45 (ddd, $J = 12.5, 10.9, 6.2$ Hz, 1H), 2.94 (ddd, $J = 20.9, 6.2, 4.7$ Hz, 1H), 2.52 (dddd, $J = 20.9, 10.9, 2.8, 1.3$ Hz, 1H).

^{13}C -NMR (100.6 MHz, CDCl_3 , 77 ppm, +25 °C): δ 199.7 (C=O), 192.49 (C=O), 153.0 (Cq), 150.26 (CH), 149.66 (CH), 142.1 (Cq), 142.1 (Cq), 137.69 (Cq), 130.64 (Cq), 130.56 (Cq), 129.28 (CH), 129.21 (CH), 128.7 (CH) 127.84 (CH), 122.75 (CH), 115.91 (CH), 115.70 (CH), 115.60 (CH), 115.39 (CH), 49.59 (CH), 40.74 (CH), 36.68 (CH_2), 35.99 (CH).

HRMS (ESI): m/z calc. for $\text{C}_{25}\text{H}_{21}\text{NO}_2$ $[\text{M}+\text{H}]^+$: 404.1462, found = 405.1409.

HPLC (OZ-H column, *hexane/iPrOH* = 90:10, flow rate = 1.0 mL min⁻¹, $\lambda = 230$ nm): $t_R = 14.31$ min (*S*), 25.17 min (*R*); 99% e.e. (*R*).

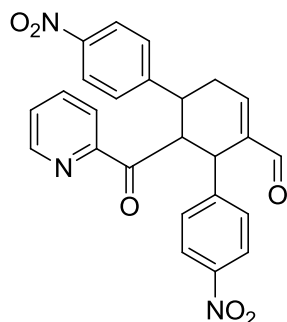
$[\alpha]_D^{22} = +3.4^\circ$ ($c = 1.0$, CHCl_3)[(*R*) catalyst].

Yield = 53%

Minor diastereoisomer

^1H -NMR (400 MHz, CDCl_3 , 7.2 ppm, +25 °C): δ 9.51 (s, 1H), 8.66 (ddd, $J = 4.7, 1.5, 0.8$ Hz, 1H), 7.29 (d, $J = 8.7$ Hz, 1H), 7.80 (ddd, $J = 8.9, 8.9, 1.7$ Hz, 1H), 7.55 – 7.32 (m, 4H), 7.10 - 6.90 (m, 4H), 6.83 (m, 2H), 4.83 (dd, $J = 3.6, 2.0$ Hz, 1H), 4.33 (broad s, 1H), 3.66 (dddd, $J = 20.6, 11.0, 3.3, 2.1$ Hz, 1H), 3.59 (ddd, $J = 11.0, 5.9, 3.6$ Hz, 1H), 2.93 (ddd, $J = 20.6, 5.9, 5.0$ Hz, 1H).

COMPOUND 3-o: 4,4''-dinitro-2'-picolinoyl-1',2',3',6'-tetrahydro-[1,1':3,1''-terphenyl]-4'-carbaldehyde



Eluent mixture (*n*-hexane:EtOAc) = 3:1

d.r. (major:minor) = 6:1

Major diastereoisomer

¹H-NMR (400 MHz, CDCl₃, 7.26 ppm, +25 °C): δ 9.48 (s, 1H), 8.74 (ddd, *J* = 4.7, 1.6, 0.9 Hz, 1H), 7.79 (ddd, *J* = 7.8, 7.8, 1.5 Hz, 1H), 7.67 (dd, *J* = 7.6, 6.3 Hz, 1H), 7.50 (dd, *J* = 15.8, 7.9 Hz, 1H), 7.17 (m, 3H), 6.88 (d, *J* = 5.2 Hz, 2H), 6.83 (d, *J* = 5.2 Hz, 2H), 6.72 (m, 2H), 5.02 (dd, *J* = 12.5, 5.4 Hz, 1H), 4.65 (dd, *J* = 5.4, 1.8 Hz, 1H), 3.51 (ddd, *J* = 12.5, 10.8, 6.1 Hz, 1H), 3.02 (ddd, *J* = 20.7, 6.1, 4.6 Hz, 1H), 2.52 (dddd, *J* = 20.7, 10.8, 2.9, 1.8 Hz, 1H).

¹³C-NMR (100.6 MHz, CDCl₃, 77 ppm, +25 °C): δ 199.30 (C=O), 191.60 (C=O), 152.40 (Cq), 151.40 (Cq), 149.70 (CH), 149.50 (CH), 147.10 (Cq), 146.70 (Cq), 146.20 (CH), 141.40 (Cq), 137.60 (CH), 130.10 (CH), 129.50 (CH), 128.40 (CH), 128.20 (CH), 128.00 (CH), 124.00 (CH), 123.40 (CH), 122.40 (CH), 48.90 (CH), 40.80 (CH), 36.40 (CH₂), 35.40 (CH).

HRMS (ESI): *m/z* calc. for C₂₅H₁₉Cl₂NNaO₄[M + Na]⁺ = 458.1352, found = 458.1374.

HPLC (OD-H column, *hexane/iPrOH* = 90:10, flow rate = 1.0 mL min⁻¹, λ = 230 nm):
t_R = 8.98 min (*S*), 11.15 min (*R*); 99% e.e. (*R*).

[α]_D²² = +4.2° (c = 1.0, CHCl₃)[(*R*) catalyst].

Yield = 85%

Minor diastereoisomer

¹H-NMR (400 MHz, CDCl₃, 7.2 ppm, +25 °C): δ 9.55 (s, 1H), 8.71 (ddd, *J* = 4.7, 1.6, 0.9 Hz, 1H), 7.92 (ddd, *J* = 7.9, 1.1, 1.1 Hz, 1H), 7.81 (ddd, *J* = 7.7, 7.7, 1.7 Hz, 1H), 7.49 – 7.46 (m, 2H), 7.37 – 7.33 (m, 2H), 7.11 – 7.05 (m, 5H), 6.82 – 6.77 (m, 1H), 4.85 (dd, *J* = 3.7, 1.9 Hz, 1H), 4.34 (broad s, 1H), 3.56 (dddd, *J* = 20.0, 10.8, 3.1, 1.6 Hz, 1H), 3.28 (ddd, *J* = 10.8, 5.6, 3.6 Hz, 1H), 2.89 (ddd, *J* = 20.0, 5.6, 5.0 Hz, 1H).

6 Appendix

6.1 Density Functional Theory (DFT)

Density Functional Theory (DFT) is a computational methodology used to predict the conformation of big molecules and bulk materials. Particularly, it is based on the determination of electron density and wave function in a many-electron system. This technique employs functionals (i.e. function of other function), which represent the spatial dependence of electron density.

Since 1990s, conformational analysis was mostly performed using molecular mechanics methods, such as MM3,⁽³⁰⁾ MMX,⁽³¹⁾ MMFF⁽³²⁾ etc. and with semi-empirical methods (AMI,⁽³³⁾ PM3⁽³⁴⁾ and MINDO⁽³⁵⁾). Generally, results obtained through these methodologies were quite accurate, at least for ground states calculations. The introduction of ab initio techniques, such as HF, introduced some advantages, even if the neglecting of electron correlation remained a serious limitation. However, such limitation could be partially overcome by using higher-level methods, such as MP2.⁽³⁶⁾

The Density Functional Theory (DFT) was introduced in the 60's by Hohenberg and Kohn, who based DFT calculations on the two Hohenberg-Kohn theorems.⁽³⁷⁾ The theorems asserted that the ground state properties of a many-electron system depend only on the electronic density, which on its turn depends on the three spatial coordinates (x,y,z). Thus, DFT calculations were based on the fact that the electron properties and wave function were determined by the electron density function $\rho(x,y,z)$. In fact, the ground state energy was described as $E_0=f(\rho)$ ⁽³⁸⁾ and by calculating electron density function the total energy of the system was determined. The Density Functional Theory (DFT) introduced great advantages considering the electron correlation compared with previously used methodologies also in terms of cost to performance ratios.⁽³⁹⁾ The technique was improved one year later by Kohn and Sham, introducing the Kohn-Sham-DFT method.

Another method that was less popular than Kohn-Sham-DFT, was known as Orbital Free Density Functional Theory (OFDFT), which is an interactive method, as well as HF methods, but differently from the first one it included the electron-correlation.

Recently, high-level calculations performed in a short amount of time have been allowed also for molecule containing 50-60 atoms thanks to the introduction of high power computers and high-efficiency software like Gaussian 09⁽⁴⁰⁾ and Spartan. DFT

calculations are very interesting because they can be applied both to conformational analysis of ground states and to the research of the correct geometries and energies of transition states. For this reason, it is the most popular method used for conformational analysis.

Since DFT calculations provide some uncertainty in calculating the relative energies of ground states, the development of the performance of some DFT functionals have been reported in many papers.⁽⁴¹⁾ The accuracy of the results is strictly connected to the association between functional and basis set used. One of the most popular functional is the hybrid B3LYP, in which the exchange energy is combined with the exact energy from Hartree-Fock theory.

This functional had often provided satisfying results in terms of conformational analysis, mostly in the prediction of the ground state energies. Regarding transition states energies, recent studies have proved⁽⁴²⁾ that taking in account of dispersion forces, as in using B3LYP, could become a big problem when the transition state is particularly crowded and the rotational barrier is higher than 30 kcal/mol. In this case, ω B97X-D functional is a valid candidate for the calculation of correct rotational barriers.

The most employed basis set for ground states calculations is 6-31G(d), where a contraction of 6 gaussian primitives describes each core orbital, while each valence shell is described by two contractions, one with 3 primitives and the other one with 1 primitive. A number of d primitives are added for every atom different than hydrogen. However, the basis set produce only a small increase in accuracy, since the functional presents limited accuracy compared with the basis set.

Geometry results collected with B3LYP could be well compared with X-ray analysis, while relative energies determined can be checked with kinetics studies results. Generally, DFT geometries and relative energies calculated well agree with experimental results.

Time-Dependent Density Functional Theory (TD-DFT)⁽⁴³⁾ is an extension of DFT used to predict the physical and chemical properties of many-body systems. Through TD-DFT calculations system properties can be studied, in the presence of a time-dependent potential. The effect of such potential allows extracting important information about the molecule, such as excitation energies and absorption spectra, as in ECD simulations.

6.2 Electronic Circular Dichroism (ECD)

Determination of the absolute configuration is an important request, mostly for pharmaceutical production, since chirality of compounds could largely determine their biological activity. In addition, also enantiomeric purity must be verified for every new drug. Although the most reliable method remains X-ray crystallography, in recent years new methods for the study of chirality have been explored based on chiro-optical properties of the system. The most largely used is circular dichroism (CD), which overcome the problem of crystallization, since X-ray methods cannot manage with compound that cannot be crystallized.⁽⁴⁴⁾ In biology, for example, Electronic Circular Dichroism (ECD) is employed to determine the secondary structure of proteins.⁽⁴⁵⁾ In particular, the Electronic Circular Dichroism (ECD) is a CD experiment conducted with UV-VIS radiations.

Circular dichroism occurs when a chiral molecule, that contains one or more chromophoric groups, adsorbs differently a left-handed circularly polarized light (L-CPL) and a right-handed circularly polarized light (R-CPL). The measurements performed in the visible and ultra-violet region register electronic transitions (ECD). The difference in such absorption creates the ECD signals, which can be either positive or negative depending on whether L-CPL is adsorbed to a greater extent than R-CPL (positive CD signal) or to a lesser extent (negative CD signal).

Circularly polarized light is obtained by the interaction between two lights that are out of phase, when the resultant is no more linearly polarized. For example, if the two lights are a quarter-wave out of phase, the resultant is a circularly polarized light (CPL) (**Figure 38**).

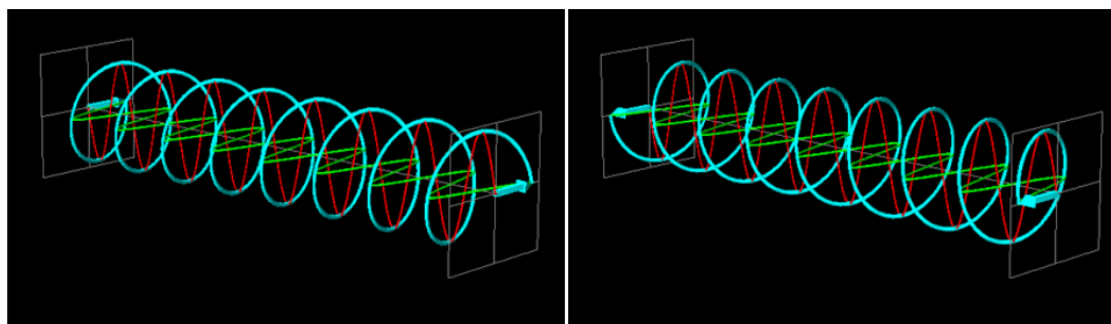


Figure 38. Left Circularly Polarised (L-CPL) Light Right Circularly Polarised (R-CPL) Light.

A molecule that absorbs differently left-handed and right-handed circularly polarized light is defined *optically active* or *chiral*. When a dextrorotatory (E_R) and levorotatory (E_L) component of a vector is different by an active compound, an elliptical polarization occurs. Therefore, it is necessary to introduce ϵ_R and ϵ_L , which are defined as absorptivity of each vector component.⁽⁴⁶⁾ The result of the analysis is the wavelength-dependent difference of absorption that is defined as the difference between the absorption of the left and the right circularly polarized light.

$$\Delta\epsilon = \epsilon_L - \epsilon_R$$

Electronic circular dichroism represents one of the most powerful methods for determination of stereochemistry, due to its sensitivity to absolute configuration and to conformational features, which is impossible to be verified by the conventional absorption spectra.⁽⁴⁷⁾

Unfortunately, there is no relationship between absolute configuration of an enantiomer and its ECD signal sign, because it depends on details on the electronic and geometric molecular structure.⁽⁴⁸⁾ However, two enantiomers could be distinguished by opposite sign of signal that maintains the same magnitude. Furthermore, spectrum signals are determined by the chromophoric groups contained in the molecule and their environment, thus ECD spectrum, intensity and position of signals reflect the environment and position of each chromophore, giving important information about chirality. Additionally, ECD is also sensitive to solvent interaction, and chiro-optical response to solute-solvent interactions is sometimes drastic and non-intuitive.⁽⁴⁹⁾ Although, a possibility to understand interactions between molecule and solvent is through force-field MD simulations.⁽⁵⁰⁾

The determination of absolute configuration should be performed comparing experimental data with more or less sophisticated calculated theoretical curves. In this case, it is very important to choose the correct reference data. Hence, time-dependent density functional theory (TD-DFT) is widely used for ECD simulations with the basic idea of extending ground state density functional theory (DFT) to time dependent-phenomena. The ECD simulated spectra strongly depends on the conformation of the molecule, thus, it is very important to carry out calculations for all structures found thanks to conformational analysis. Then the weighted spectrum is obtained taking into account of Boltzmann distributions, allowing the comparison with the experimental

results.⁽⁵¹⁾ Spectra calculated with this method are usually in very good agreement with experimental results, even if Kohn-Sham potential approximation is considered.⁽⁵¹⁾ An example of experimental and calculated comparison was reported in **Figure 39**.

4-Arylpyrazolo[3,4-b]pyridine

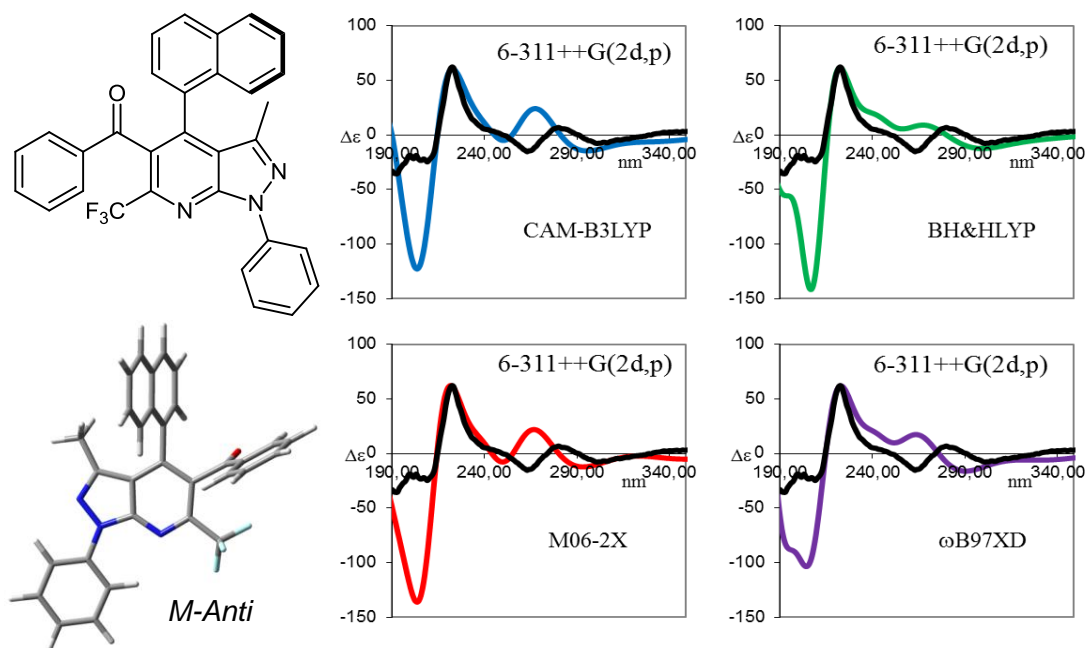


Figure 39. Comparison between experimental and calculated ECD spectra with different functionals. Coloured lines; calculated spectra, black lines: experimental spectra.⁽⁵²⁾

6.3 Vibrational Circular Dichroism (VCD)

Vibrational circular dichroism (VCD) spectroscopy is basically circular dichroism spectroscopy in the infrared and near infrared ranges.⁽⁵³⁾ This technique is very similar to the above-mentioned ECD, since it allows predicting the optical properties (such as chirality) of a substance by the circularly polarized infrared radiations. In particular, VCD is the differential absorption of left and right circularly polarized infrared light (L-CPL and R-CPL), which occurs in an *optically active* molecule. Hence, differently from ECD, VCD study the absorption of infrared radiations, instead of UV-visible radiations. This technique has been shown to be particularly useful for the study of the conformational characteristics and absolute configuration of large biological samples such as nucleic acids and smaller molecules like chiral pharmaceutical drugs. Extensive VCD studies were performed for several proteins in solution and other complex scaffolds.⁽⁵⁴⁾ The published reports have proved VCD as a powerful technique, which provides complementary and improved results compared with those previously obtained by visible/UV circular dichroism (ECD). However, one of the problems associated with VCD and generally with vibrational activity is the weakness of signals. In fact, strength of vibrational signals is much smaller than those of electronic bands, involving low signal-to-noise ratios. Thus, VCD experiments generally require a higher sample concentration compared with ECD and for this reason, ECD technique is often preferred. As well as for ECD, VCD can be usefully employed in conjunction with DFT calculations to determine the absolute configuration of newly synthesized molecules and can be used to determine enantiomeric purity in molecules whose absolute configuration is already known.⁽⁵⁵⁾

Generally, DFT calculations are commonly employed for VCD simulations and compared with the experimental results. As well as for ECD, it is very important to perform VCD calculations for all structures found thanks to conformational analysis, since VCD results strongly depend on the environment of a molecule. Then the weighted VCD simulated spectrum is obtained taking in count of Boltzmann distributions. An example of comparison between simulated and experimental VCD spectra obtained for (*M*)-BINOL, was reported below (**Figure 40**).

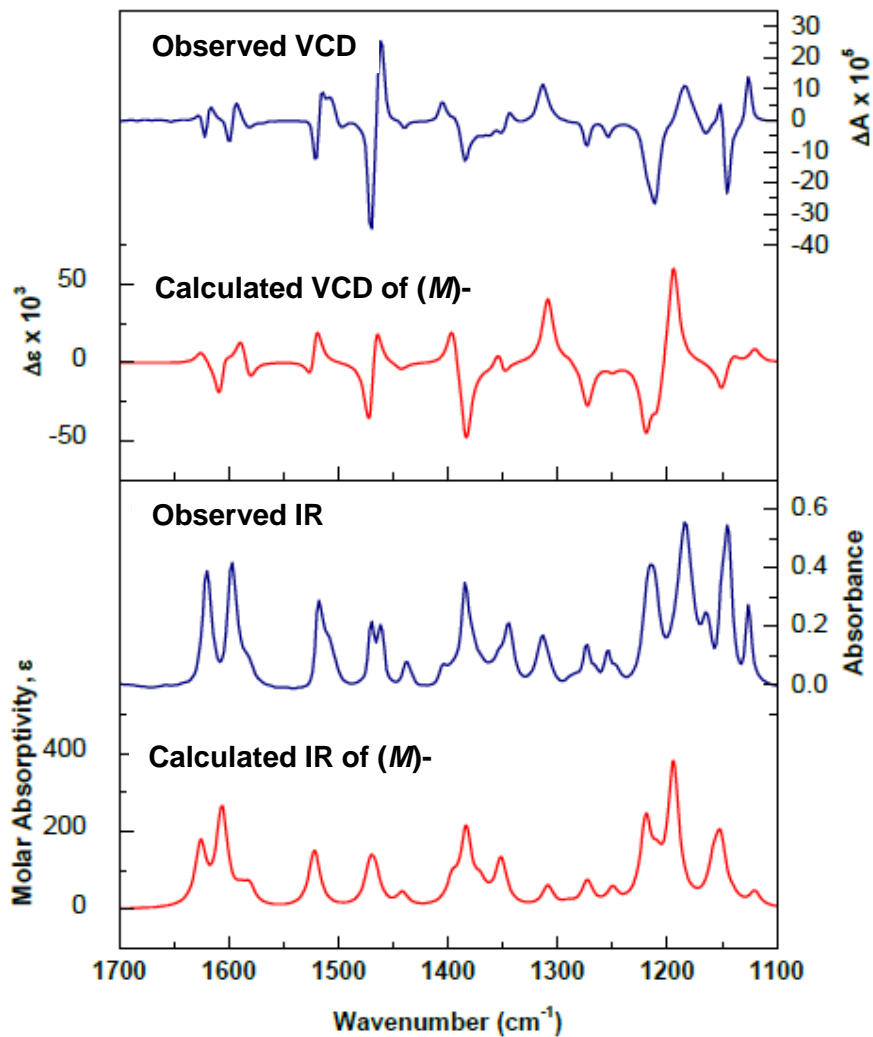
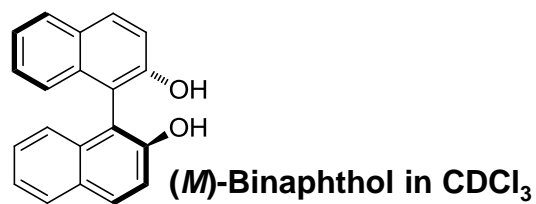


Figure 40. Comparison between experimental and calculated ECD spectra.⁽⁵⁶⁾

7 Bibliography

- ⁽¹⁾ L. A. Nguyen, H. He, C. Pham-Huy, *International journal of Biomedical Science*, **2006**, 2, 85-100.
- ⁽²⁾ W. Len *s.l.*: *Tetratology*, **1988**, 38, 203-215.
- ⁽³⁾ K.B. Sharpless, *Angew. Chem. Int. Ed. Engl*, **2001**, 41, 2024–2032.
- ⁽⁴⁾ C. S. Foote, *Acc. Chem. Res.*, **2000**, 33, 323–440.
- ⁽⁵⁾ a) P. I. Dalko and L. Moisan, *Angew. Chem. Int. Ed. Engl*, **2004**, 43, 5138–5175. b) P. I. Dalko and L. Moisan, *Angew. Chem. Int. Ed. Engl.*, **2001**, 41, 3726–3748. c) B. List, *Synth. and Cat.*, **2004**, 346-1021. d) B. List, *Chem. Commun*, **2004**, 719–722.
- ⁽⁶⁾ a) Z. G. Hajos, D. R. Parrish, *J. Org. Chem.*, **1974**, 39 (12), 1615–1621, b) U. Eder, G. Sauer, R. Wiechert, *Angew. Chem. Int. Ed.*, **1971**, 20, 496–497.
- ⁽⁷⁾ A. B. Northrup and D. W. C. MacMillan, *J. Am. Chem. Soc.*, **2002**, 124, 2458–2460.
- ⁽⁸⁾ M. Bella, S. Kobbelgaard, K. A. Jørgensen, *J. Am. Chem. Soc.*, **2005**, 127, 3670–3671.
- ⁽⁹⁾ P. McDaid, Y. Chen, A. Deng, *Angew. Chem. Int. Ed. Engl.*, **2002**, 41, 338–340.
- ⁽¹⁰⁾ Y. Huang, A. K. Unni, A. N. Thadani, Rawal, V. H., *Nature*, **2003**, 424, 146–1146.
- ⁽¹¹⁾ M. Meazza, *Thesis for the degree of Doctor of Philosophy*, Southampton University, **2016**.
- ⁽¹²⁾ H. Gotoh, T. Hayashi, M. Shoji, *Angew. Chem. Int. Ed.*, **2005**, 44, 4212–4215.
- ⁽¹³⁾ K. A. Ahrendt, C. J. Borths and D. W. C. MacMillan, *J. Am. Chem. Soc.*, **2000**, 122 (17), 4243–4244.
- ⁽¹⁴⁾ B. List, *Tetrahedron*, **2002**, 58, 5573-5590.
- ⁽¹⁵⁾ a) M. Meazza, R. Rios, *Synthesis*, **2016**, 48, 960-973. b) I. Ibrahim, A. Cordova, *Angew. Chem. Int. Ed.*, **2006**, 45, 1952-1956. c) M. Meazza, V. Ceban, M. B. Pitak, S. J. Coles, R. Rios, *Chem. Eur. Journal*, **2014**, 20, 16853-16857.
- ⁽¹⁶⁾ a) A. E. Allen, D. W. C. MacMillan, *Chem. Sci.*, **2012**, 2, 633-658. b) D. A. Evans, J. Bartroli, T. L. Shih, *J. Am. Chem. Soc.* **1981**, 103, 2127-2129.
- ⁽¹⁷⁾ a) I. Ibrahim, S. Santoro, F. Himoto, A. Cordova, *Adv. Synth. Catal.*, **2011**, 353, 245-252. b) M. A. Kacprzyński, S. A. Kazane, T. L. May, A. H. Hoveyda, *Org. Lett.*, **2007**, 9, 3187-3190.
- ⁽¹⁸⁾ S. Afewerki; P. Breistein, K. Pirttila, L. Deiana, P. Dziejcz, I. Ibrahim, A. Cordova, *Chem. Eur. J.*, **2011**, 17, 8784-8788.

- ⁽¹⁹⁾ M. Meazza, F. Tur, N. Hammer, K. A. Jørgensen, *Angew. Chem. Int. Ed.*, **2017**, *56*, 1–6.
- ⁽²⁰⁾ For authoritative reviews on the concept of organocatalytic cascade reactions: a) A. N. Alba, X. Companyo, M. Viciano and R. Rios, *Curr. Org. Chem.*, **2009**, *13*, 1432–1474. b) D. Enders, C. Grondal and M. R. Huttl, *Angew. Chem Int. Ed.*, **2007**, *46*, 1570–1581. c) C. Grondal, M. Jeanty and D. Enders, *Nat. Chem.*, **2010**, *2*, 167–178.
- ⁽²¹⁾ For an excellent review: T. Newhouse, P. S. Baran and R. W. Hoffmann, *Chem. Soc. Rev.*, **2009**, *38*, 3010–3021.
- ⁽²²⁾ a) L. F. Tietze, U. Beifuss, *Angew. Chem.*, **1993**, *105*, 137–170. b) L. F. Tietze, U. Beifuss *Angew. Chem. Int. Ed. Engl.*, **1993**, *32*, 131–163; c) L. F. Tietze, *Chem. Rev.*, **1996**, *96*, 115–136; d) L. F. Tietze, G. Brasche, K. Gericke, *Weinheim*, **2006**.
- ⁽²³⁾ a) L. F. Tietze, A. Modi, *Med. Res. Rev.*, **2000**, *20*, 304–322. b) *Multicomponent Reactions*, (Eds.: J. Zhu, H. Bienaym), Wiley-VCH, **2005**. c) *Synthesis of Heterocycles via Multicomponent Reactions*, (Eds.: R. V. A. Orru, E. Ruijter), Springer, **2010**.
- ⁽²⁴⁾ a) B. List, *Chem. Commun.*, **2006**, 819–824. b) A. Erk-kilä, I. Majander, P. M. Pihko, *Chem. Rev.*, **2007**, *107*, 5416–5470; c) S. Mukherjee, J. W. Yang, S. Hoffmann, B. List, *Chem. Rev.*, **2007**, *107*, 5471–5569; d) X. Yu, W. Wang, *Org. Biomol. Chem.*, **2008**, *6*, 2037–2046; e) C. Palomo, A. Mielgo, *Angew. Chem.*, **2006**, *118*, 8042–8046; f) C. Palomo, A. Mielgo, *Angew. Chem. Int. Ed.*, **2006**, *45*, 7876–7880.
- ⁽²⁵⁾ A. Carlone, S. Cabrera, M. Marigo and K. A. Jørgensen, *Angew. Chem., Int. Ed.*, **2007**, *46*, 1101–1104.
- ⁽²⁶⁾ T. Bui, C. F. Barbas, *Tetrahedron Lett.*, **2000**, *41*, 6951–6954.
- ⁽²⁷⁾ X. Companyo, A. Zea, A. R. Alba, A. Mazzanti, A. Moyano and R. Rios, *Chem. Commun.*, **2010**, *46*, 6953–6955.
- ⁽²⁸⁾ Starting materials **2i-2h-2f** were synthesized by Gabriela Sitinova.
- ⁽²⁹⁾ Compounds obtained with (*S*)-Jørgensen catalyst were synthesized by Gabriela Sitinova.
- ⁽³⁰⁾ N. L. Allinger, Y. H. Yuh, J.-H. Lii, *J. Am. Chem. Soc.*, **1989**, *111*, 8551–8566.
- ⁽³¹⁾ *PCMODEL*, v9, Serena Software, Bloomington, IN (USA).
- ⁽³²⁾ T. A. J. Halgren, *Comput. Chem.*, **1996**, *17*, 520–552.
- ⁽³³⁾ M. J. S. Dewar, E. G. Zoebisch, E. F. Healy, J. J. P. Stewart, *J. Am. Chem. Soc.*, **1985**, *107*, 3902–3909.
- ⁽³⁴⁾ a) J. J. P. Stewart, *J. Comput. Chem.*, **1989**, *10*, 209–220; b) J. J. P. Stewart, *J. Comput. Chem.* **1989**, *10*, 221–264.

- ⁽³⁵⁾ R. C. Bingham, M. J. S. Dewar, D. H. Lo, *J. Am. Chem. Soc.*, **1975**, *97*, 1285–1293.
- ⁽³⁶⁾ M. J. Frisch, M. Head-Gordon, J. A. Pople, *Chem. Phys. Lett.*, **1990**, *166*, 281–289.
- ⁽³⁷⁾ P. Hohenberg, W. Kohn, *Phys. Rev.*, **1964**, *136*, 864–871.
- ⁽³⁸⁾ P. C. H. Mitchell, *Appl. Organometal. Chem.*, **2000**, *14*, 744–747. in the preface to: *A Chemist's Guide to Density Functional Theory*, (Eds.: W. Koch, M. C. Holthausen), Wiley-VCH, 2nd ed., **2002**.
- ⁽³⁹⁾ a) *A Chemist's Guide to Density Functional Theory* (Eds.: W. Koch,; M.C. Holthausen), Wiley-VCH, 2nd ed., **2002**; b) *A Primer in Density Functional Theory* (Eds.: C. Fiolhais,; F. Nogueira,; M. Marques), Springer-Verlag, **2003**.
- ⁽⁴⁰⁾ a) C. E. Check, T. M. Gilbert, *Org. Chem.*, **2005**, *70*, 9828–9834; b) M. D. Wodrich, C. Corminbouef, P. Schleyer, *Org. Lett.*, **2006**, *8*, 3631–3634; c) P. R. Shreiner, A. Fokin, R. A. Pascal, A. De Mejere, *Org. Lett.*, **2006**, *8*, 3635–3638; d) S. Grimme, *Angew. Chem. Int. Ed.*, **2006**, *45*, 4460–4464; e) Y. Zhao, D. G. Truhlar, *Org. Lett.*, **2006**, *8*, 5753–5755; f) T. A. Rokob, A. Hamza, I. Pápai, *Org. Lett.*, **2007**, *9*, 4279–4282; g) P. R. Shreiner, *Angew. Chem. Int. Ed.*, **2007**, *46*, 4217–4219; h) M. D. Wodrich, C. S. Wannere, Y. Mo, P. D. Jarowski, K. N. Houk, P. Schleyer, *Chem. Eur. J.*, **2007**, *13*, 7731–7744; i) Y. Zhao, D. G. Truhlar, *Acc. Chem. Res.*, **2008**, *41*, 157–167; j) T. Schwabe, S. Grimme, *Acc. Chem. Res.*, **2008**, *41*, 569–579; k) M. D. Wodrich, D. F. Jana, P. Schleyer, C. Corminbouef, *J. Phys. Chem.*, **2008**, *112*, 11495–11500.
- ⁽⁴¹⁾ D. Young, *Computational Chemistry*, **2001**, *17*, 147–158.
- ⁽⁴²⁾ E. Masson, *Org. Biomol. Chem.*, **2013**, *11*, 2859–2871 .
- ⁽⁴³⁾ E. Runge, E. K. U. Gross, *Phys. Rev. Lett.*, **1984**, *52*, 997–1000.
- ⁽⁴⁴⁾ a) *Circular Dichroism and the Conformational Analysis of Biomolecules* (Ed.: G. D. Fasman) New York: Plenum Press; **1996**. b) P. Manavalan, W. C. Johnson, *Biosci.*, **1985**, *8*, 141–149. c) N. Sreerama, S. Y. Venyaminov, R. W. Woody, *Anal. Biochem.*, **2000**, *287*, 243–251.
- ⁽⁴⁵⁾ *Circular dichroism, Principles and applications* (Eds.: N. Berova, K. Nakanishi, R. W. Woody), Plenum Press, **2000**.
- ⁽⁴⁶⁾ a) *Introduction to stereochemistry* (Eds.: K. Mislow), W. A. Benjamin Inc., **1965**. b), N. Berova, L. Di Bari, G. Pescitelli, *Chem. Soc. Rev.*, **2007**, *36*, 914–931.
- ⁽⁴⁷⁾ *WIREs Comput Mol Sci*, **2012**, *2*, 150–166.
- ⁽⁴⁸⁾ L. Caruana, M. Mondatori, V. Corti, S. Morales, A. Mazzanti, M. Fochi, L. Bernardi, *Chem. Eur. J.*, **2015**, *21*, 6037–6041.
- ⁽⁴⁹⁾ a) J. Kongsted, T. B. Pedersen, A. Osted, A. E. Hansen, K. V. Mikkelsen, O. J.

Christiansen, *J. Chem. Phys. A*, **2004**, *108*, 3632–3641. b) T. Müller, K. B. Wiberg, P. H. Vaccaro, *J. Chem. Phys. A*, **2000**, *104*, 5959–5968. c) Y. Kumata, J. Furukawa, T. Fueno, *Bull. Chem. Soc. Jpn.*, **1970**, *43*, 3920–3921. d) P. Mukhopadhyay, G. Zuber, M. Goldsmith, P. Wipf, D. N. Beratan, *Chem. Phys. Chem.*, **2006**, *7*, 2483–2486.

⁽⁵⁰⁾ a) M. D. Kundrat, J. Autschbach, *J. Chem. Theory Comput.*, **2009**, *5*, 1051–1060. b) P. Mukhopadhyay, G. Zuber, M. Goldsmith, P. Wipf, D. N. Beratan, *Chem. Phys. Chem.*

⁽⁵¹⁾ M. A. L. Marques, E. K. U. Gross, *Annu. Rev. Phys. Chem.*, **2004**, *55*, 427–455.

⁽⁵²⁾ P. Gunasekaran, S. Perumal, J. C. Menéndez, M. Mancinelli, S. Ranieri, A. Mazzanti, *J. Org. Chem.*, **2014**, *79*, 11039 – 11050.

⁽⁵³⁾ <http://planetphysics.org/?op=getobj;from=objects;id=410> Principles of IR and NIR Spectroscopy.

⁽⁵⁴⁾ a) P. Malon, R. Kobrinskaya, T. A. Keiderling, *Biopolymers*, **1988**, *27*, 733-746. b) T. A. Keiderling, S. C. Yasui, U. Narayanan, A. Annamalai, P. Malon, R. Kobrinskaya, L. Yang, *Spectroscopy of Biological Molecules New Advances* (Eds.: E. D. Schmid, F. W. Schneider, F. Siebert), **1988**. c) S. C. Yasui, T. A. Keiderling, *Mikrochimica Acta*, **1988**, *II*, 325-327.

⁽⁵⁵⁾ I. Chabay and G. Holzwarth, *Appl. Opt.*, **1945**, *14*, 254-260.

⁽⁵⁶⁾ http://www.chemtech.ugent.be/upload/files/VCD_White_Paper_Jan2017.pdf.

Aknowlegments

I would like to begin by thanking Prof. Andrea Mazzanti, supervisor of this thesis, for the indispensable help provided for the realization of this project and for the availability always shown during this work. I would like to thank Dr. Ramon Rios Torres, co-supervisor, for the immense support and for giving me the opportunity to perform part of this work in his research team. I would also like to reserve a part of my awards to the research teams I had the pleasure to work with: in particular Gabriela Sotinova, who was my partner in this project and whose support was fundamental; Dr. Michele Mancinelli, for the indispensable contribution in this project and in the elaboration of the thesis; and finally Dr. Luke Shirley and Dr. Luca Prati, for the many tips and the help they gave to me whenever I needed it. Lastly, I would like to give special thanks to the Universities of Bologna and Southampton for giving me the opportunity and the indispensable materials to accomplish this path.